DOCTOR OF PHILOSOPHY

Optical and acoustic beam shaping for imaging and manipulation

Yang, Zhengyi

Award date:
2014

Awarding institution:
University of Dundee

Optical and acoustic beam shaping for imaging and manipulation

Zhengyi Yang

A thesis submitted for the degree of

Doctor of Philosophy (PhD)

University of Dundee

September 2014

Contents

List of Figures

List of Tables

Acknowledgement

There are numerous people I would like to acknowledge throughout my graduate study. It has been a great pleasure and honour to work with all of them.

First, I would like to thank my supervisor, Mike MacDonald. From my first visit to Institute of Medical Science and Technology (IMSaT) in September 2010, I knew this would be where I want to perform research. Mike has been incredibly supportive as an advisor and mentor. It has been an amazing graduate experience for me.

I would also like to acknowledge Christine Démoré. When I started working on ultrasound, Christine was the one who patiently helped me advancing my knowledge and skills, not only on ultrasound, but also my programming skills in Matlab and experimental protocols, all of which have been very crucial to this thesis.

I acknowledge Prof. Sandy Cochran and Paul Prentice's contribution in my graduate study and this thesis. Great thanks to Prof. Gabe Spalding for his help and guidance. Even though he was only in Dundee for a fairly short time, he has always inspired me and gave me a lot of courage. I also acknowledge Zhihong Huang for all the support during the graduate study.

I would like to say thanks to Patrick Dahl for the great help to improve my English through a lot of discussion.

Additionally, the experiments with ExAblate system would not be possible without the help of Alexander Volovick and Osnat Dogadkin. They have been

very helpful for sharing the knowledge and experience on the ultrasound transducer system.

I would like to thank all the help from people in James Hutton Institute, including Lionel Dupuy, Helen Downie, Kleber Mariano, Caroline Upton and others. They have given me a lot of advice and demonstration in the lab on sample preparing procedures. I am particularly grateful for the assistance and advices provided by Lionel.

Thanks to Graham Brodie, Bjoern Gerold, Paul O'Mahoney and all the other colleagues in the office for their help in the lab and the discussions. Great thanks to Yongqiang Qiu, Zhen Qiu, Joyce Joy, Han Wang, Xu Xiao, Doudou Xu, Xiaochun Liao, Yang Kuang, Chunhui Li, Srikanta Sharma and many other colleagues for all the support. Whenever I had problems, they were always willing to help. I also would like to acknowledge Peter Glynne-Jones for the acoustic simulations.

I also acknowledge Chinese Scholarship Council (CSC) for providing scholarship to make my graduate study possible, as well as Engineering and Physical Sciences Research Council (EPSRC) and Scottish Funding Council (SFC) for providing the research funds.

And finally last, but not least, I would like to say great thanks to my Wife Xiaojing Lv, for all the support and understanding. She is always interested in what I am doing, support me when I am down and be happy with me when I achieve. Without her support and love I could not have made this. Thank you.

Declaration

I hereby declare that this dissertation entitled `Optical and acoustic beam shaping for imaging and manipulation' has been prepared by me under the direct guidance of Dr Michael P. MacDonald as part of my study for the award of PhD Degree at the University of Dundee, Dundee, Scotland. I have not submitted this dissertation previously for the award of any degree or diploma at any other institution.

Signature. Date.

This is to certify that the candidate has fulfilled the conditions of the Regulations appropriate of the degree of Doctor of Philosophy in the University of Dundee and that the candidate is qualified to submit this thesis in application for that degree.

Signature. Date.

List of Publications

- C. Démoré, P. Dahl, Z. Yang, P. Glynne-Jones, A. Melzer, S. Cochran, M. MacDonald, and G. Spalding, "Acoustic tractor beam," *Phys. Rev. Lett.*, vol. 112, no. 17, p. 174302, Apr. 2014.
- Z. Yang, H. Downie, E. Rozbicki, L. Dupuy and M. MacDonald, "Light Sheet Tomography (LST) for *in situ* imaging of plant roots," *Opt. Express*, vol. 21, no. 14, pp. 16239–16247, 2013.
- C. Démoré, Z. Yang, A. Volovick, S. Cochran, M. MacDonald, and G. Spalding, "Mechanical Evidence of the Orbital Angular Momentum to Energy Ratio of Vortex Beams," *Phys. Rev. Lett.*, vol. 108, no. 19, p. 194301, May 2012.
- C. Démoré, Z. Yang, A. Volovick, H. Wang, S. Cochran, M. MacDonald, and G. Spalding, "A sonic screwdriver: Acoustic angular momentum transfer for ultrasonic manipulation," *in Ultrasonics Symposium (IUS), 2011 IEEE International*, pp. 180–183, 2011.
- G. Spalding, A. Volovick, Z. Yang, C. Démoré, M. MacDonald, and S. Cochran, "The sonic screwdriver: a model system for study of wave angular momentum," *SPIE NanoScience+ Engineering (p. 80971N–80971N–10). International Society for Optics and Photonics*, 2011.

Abstract

Sound and light show many similarities because they both propagate as waves. This means they share the same wave properties such as reflection, refraction, scattering, diffraction, and so on. The similarities between them bring a lot of opportunities for translating knowledge of one onto the other. When compared to ultrasound, and particularly in microscopy and micromanipulation, optics is a more-developed and better-understood area, partly due to the difficulty of producing complex ultrasonic beams. Hence it makes perfect sense to explore sound based on the research of optics. Differences between light and sound are mainly due to the nature variety of their mechanisms and different scale of their wavelength. Those difference makes either light or sound suitable for certain applications.

This thesis will focus on the currently technology for beam shaping for acoustic and optical waves, making use of their similarities, especially for imaging and manipulation purposes.

When light scattering and absorption is low, optical scattering is able to provide high resolution and suitable for imaging. A low-cost Light-Sheet Tomography imaging system is built for monitoring the growth of plant roots based on optical scattering from the roots. When optical scattering and absorption is severe it dramatically decreases spatial resolution, optical absorption can be employed to generate less-scattered acoustic signals to form high contrast images of the optical absorbing structure in a sample. A photoacoustic imaging system featuring light sheet illumination is built, along

with an automatic data acquisition system. 2D images acquired with this system are reconstructed with inverse Radon transformation.

The short wavelength of optical waves makes them suitable for interaction with micron-scale objects, but less suitable for macro objects because the force does not easily scale up with the size of the targets. On the other hand, ultrasonic waves have the suitable wavelength and power level for interaction with mm- or even cm- size objects.

Various ultrasonic beams with vortex wavefront were generated with a 1000-element phase-control transducer array to levitate and rotate a macro acoustic absorber by transferring linear and angular momentum from the acoustic beam to the absorber. The ratio between linear and angular momentum in the beam was measured simultaneously. With the same ultrasound transducer array, the delivery of a controllable negative radiation force onto prism-shape target is demonstrated to pull the prism towards the sound source. This is the first demonstration of macroscopic and ultrasonic tractor beam.

The study of ultrasound and optical beam shaping has proven that the similarities between sound and light waves can be utilized to extend our existing knowledge on them, and further provides more opportunities on wave-matter interaction applications.

Abbreviations

2P-SPIM	two-photon scanned light-sheet microscopy
AOD	acousto-optic deflector
AOTF	acousto-optical tuneable filter
AOM	acousto-optic modulator
AR-PAM	acoustic-resolution PAM
BBI	Bessel beam illumination
CW	continuous wave
DOE	diffractive optical element
DSLM	digital scanned laser light-sheet fluorescence microscopy
DSLM-SI	DSLM-structured illumination
EM	Electromagnetic
EMBL	European Molecular Biology Laboratory
FL	focal length
FLIM	fluorescence lifetime imaging microscopy
FOV	field of view
FUS	focused ultrasound surgery
GFP	green fluorescence protein
HG	Hermite-Gaussian
HIFU	high intensity focused ultrasound
HiLo	highly inclined and laminated optical sheet microscopy
HROPFOS	high-resolution OPFOS

LC	liquid crystal
LG	Laguerre-Gaussian
LSFM	light sheet fluorescence microscopy
LST	light-sheet tomography
MRI	magnetic resonance image
MuVi-SPIM	Multiview SPIM
NA	numerical aperture
ND	neutral density
NDT	non-destructive testing
NRF	negative radiation force
NUE	plant nutrient use efficiency
OAM	orbital angular momentum
OCPI	objective-coupled planar illumination
OCT	optical coherence tomography
OPFOS	orthogonal-plane fluorescence optical sectioning microscope
OPM	oblique plane microscopy
OR-PAM	optical-resolution PAM
PALM	photo activated localization microscopy
PAM	Photoacoustic microscope
PML	perfectly matched layer
PSF	point spread function
Re	Reynolds number
SAM	spin angular momentum
SDCLM	spinning disk confocal laser microscopy
SIM	structured illumination microscopy
SiMView	simultaneous multiview
SLM	spatial light modulator
SPIM	selective/single plane illumination microscopy

SPIM-SI	SPIM with structured illumination
SSIM	saturated structured illumination microscopy
SSP	spiral phase plate
STED	stimulated emission depletion microscopy
TCSPC	time-correlated single-photon counting
TLSM	thin laser light-Sheet microscope
USW	ultrasonic standing wave

Chapter 1
Introduction

The nature of sound and light is fascinating, not only do they help us observe the world, but also they can interact with matter and even exert force onto objects through momentum transfer. Both light and sound propagates as waves, which makes them very similar to each other. They share many wave properties and often interact with matters in an analogous manner.

Thanks to the laser technology and development in optical beam shaping tools, optics is a well-established subject, applied in many areas such as imaging and micro-manipulation. On the contrary, research in ultrasound is not as widespread. It is often limited by the difficulty on complex sound beam generation and the high amplitude attenuation during propagation. The similarities between sound and light make perfect sense for us to extend our knowledge and understanding in optics into acoustics, and *vice versa*.

The differences between light and sound can also be of benefit. They are mainly on two aspects. 1) Light propagates as electromagnetic wave while sound propagates as mechanical waves. This difference in nature determines that their interaction with materials varies. 2) Their wavelength scale differs. Generally speaking, the wavelength of sound waves is several magnitudes larger than that of visible light waves, which means short-wavelength light wave is suitable for precise interaction with micro-objects, while long-wavelength sound wave

experiences less scattering and is more likely to provide larger force for manipulation. Those differences bring higher chance of finding the right type for practical application.

Similarities and differences between sound and light lead to cross-fertilisation of ideas between them, bringing new possibilities both in a hybrid system, and even when only one modality is used.

In this thesis, properties of the waves, especially the similarities, along with the beam shaping techniques in both areas, will be investigated and applied to the imaging and manipulation objects.

1.1 Waves

Because the similar and analogous behaviours of light and sound come from their wave nature it is useful to discuss here the properties of waves. A wave is defined as a disturbance or oscillation that travels through space and matter, accompanied by a transfer of energy.

There are two main types of waves. Mechanical waves propagate through a medium and the substance of this medium is deformed. The deformation reverses itself owing to restoring force resulting from its deformation. In air, sound waves propagate via air molecules colliding with their neighbour as a kind of mechanical wave. Sometimes sound waves are also referred to as pressure waves because it consists of a repeating pattern of high-pressure and low-pressure regions moving through a medium. The second type of waves, electromagnetic (EM) waves, consist of periodic oscillations of electrical and magnetic field generated by charged particles, hence do not require a medium and can travel through a vacuum. Types of EM waves vary in wavelength and among which, visible light with wavelength ranges from 400 nm to 700 nm is one typical kind.

A wave can be transverse or longitudinal depending on the direction of its oscillation. Transverse waves occur when the oscillation is perpendicular to the propagation, while longitudinal waves occur when the oscillations are parallel to the propagation. EM waves are transverse while sound waves in gas, or fluids are longitudinal. Even though sound waves in a solid medium can be transverse, as well as longitudinal, we usually say sound waves are longitudinal because applications of sound waves are usually carried out in gas or fluids.

Among all the forms of waves, sound and light waves are the most widely used, such as enhancing our ability to observe or manipulate microscopic objects. There are many notable similarities between acoustic beams and optical beams; at the same time, they are different. For instance, long wavelength of sound makes it a useful tool to interact with macroscopic target while submicron-scale wavelength of light makes it suitable for microscopic target. Moreover, as different forms of waves, they interact different materials differently, which brings more choices for various purposes such as gaining contrast in imaging applications. Those all make it interesting to investigate the similarities and analogue between light and sound, which is the purpose of this thesis.

1.2 Physical Properties of Waves

1) Absorption

The energy of a wave is proportional to the square of its amplitude. When the wave passes through a substance, its energy is absorbed by the substance, resulting in a decrease of the amplitude, termed absorption. Substances are usually selectively absorbing, i.e. they absorb specific radiation, at specific wavelengths. For instance, water is transparent to EM waves around visible light wavelength but is strong absorber below 100 nm or above 1um, as shown in Figure 1-1.

Normally the energy is transformed to internal energy of the absorber as heat. When light is absorbed by the sample and cause a temperature rise, it can

lead to thermal expansion and further to generation of sound as a pressure transient, which is termed photoacoustic effect and is utilized in photoacoustic imaging (PAM). More details of PAM will be studied in Chapter 5.

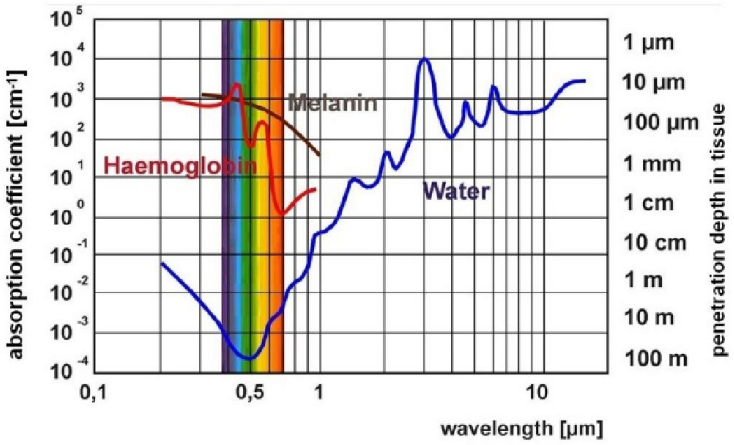

Figure 1-1 Absorption spectra of EM waves for water, haemoglobin and melanin, clearly shown that the absorption coefficient depends on wavelength and material [1]

2) Scattering

Scattering happens when the wave is forced to deviate from its original trajectory due to the localized non-uniformities in the medium through which they pass. Depending on the size of the scatterers and the wavelength of the EM wave, optical scattering behaves differently.

When particles are much smaller than the wavelength of the light, Rayleigh scattering dominates, in which the scattering strongly dependent to the wavelength of the light [2]:

$$I_s = k\frac{1}{\lambda^4} \qquad \text{Eq. (1-1)}$$

Where I_s scattered intensity of light, λ is the wavelength. As shown in Eq. (1-1) that in Rayleigh scattering, the intensity of scattering is inverse proportional to quartic of light wavelength. An everyday example of this is seen when sun light passes through our atmosphere, short-wavelength light is strongly scattered by air molecules and some reaches our eyes, while the long-wavelength light penetrates the atmosphere. Hence the sky appears blue to us.

For particle sizes equivalent to or larger than the light wavelength, Mie scattering predominates, in which the scattering produces a pattern like an antenna lobe, with a sharper and more intense forward lobe for larger particles. Comparing to Rayleigh scattering, Mie scattering is less sensitive to the wavelength. The size of water drops in the cloud is close to the wavelength of visible light, hence sun light experience Mie scattering in cloud and appears white.

Usually scattering and absorption happens at the same time, which leads to attenuation, defined as the reduction in the intensity of a wave propagating through the medium. Attenuation efficiency highly varies by wave types or wavelength. For instance, in optically-transparent media like air or water, acoustic waves experience much higher attenuation than EM waves because of the energy consumption caused by the viscosity of those transmitting media. Acoustic attenuation results from the combined losses due to both absorption and scattering, while in soft tissues scatter component accounts for about 10% - 15% of the total attenuation [3]. In soft tissues, acoustic attenuation coefficient is nearly linear frequency dependent [4], to be more specific, around 0.6 – 0.9 dB/cm for 1 MHz ultrasound [5], which is much lower than optical absorption coefficient and gives ultrasound better penetration depth comparing to light.

Scattering has been used in many aspects. For instance, scattering of sound or light can be employed for imaging; microscopy based on scattering will be investigated in Chapter 3 for imaging plant roots *in vivo*. In addition, scattering of light results in a tiny force on the scatterers, which is utilized in optical trapping devices.

3) Reflection

When a wave strikes an interface between two different media, it changes direction and returns into the medium from which it originated, called reflection. Reflection coefficient, describes as the amplitude of reflected wave related to that

of the incident wave, depends on the impedances of the two media. For instance, at the interface of two medium with impedance z_1 and z_2, the reflection coefficient is

$$\mathrm{r} = \left|\frac{z_2 - z_1}{z_2 + z_1}\right| \qquad \text{Eq. (1-2)}$$

At the interface of media with mismatched impedance, a bigger portion of the energy would be reflected rather than going through the boundary. This is similar for both optical beam and acoustic beam, even though the definition of impedance is different in each concept. A material's characteristic optical impedance is inversely proportional to the refractive index of this material while its characterized acoustic impedance depends on both the density of transmitting medium and sound speed in it.

When reflection is not wanted, anti-reflection coating can be added between the media for impedance matching to reduce the reflection coefficient, hence increase the energy going through the interface. On the other hand, reflection of waves causes echoes and can be used in imaging, for example, in sonography with ultrasound and in optical coherence tomography (OCT) with light. In Chapter 6, special targets were customized with hollow design to enhance the reflection of ultrasound.

4) Refraction

Refraction happens when a wave changes its speed and results in changing of its direction. Refraction is the most commonly observed phenomenon with light, but any types of waves can refract when it interacts with different media. The direction of incidence and refraction are related to the refractive indices of the two material by Snell's law:

$$\frac{sin\,\theta_1}{sin\,\theta_2} = \frac{n_2}{n_1} = \frac{v_1}{v_2} \qquad \text{Eq. (1-3)}$$

With each θ as the angle measured from the normal of the boundary, v as the velocity of light in the respective medium, and n as the refractive index of the respective medium.

In optics, refractive index of a substance is a dimensionless number that describes how light propagates through that medium. It is defined as $n = c/v$, where c is the speed of light in vacuum and v is the speed of light in the substance. This concept is widely used within the full EM spectrum. It can also be used with other waves such as acoustic waves. In this case, the speed of sound is used instead of that of light and a reference medium other than vacuum must be chosen [6].

Refraction is the principle behind optical lenses for shaping light path. Analogously, acoustical lenses are also built to bend or curve sound beams, usually for underwater applications.

5) Diffraction

A wave exhibits diffraction when it encounters an obstacle. The wave bends around small obstacles and spreads out after passing small openings. Diffraction occurs with all waves, including sound waves and EM waves.

It is very confusing to distinguish diffraction from another property of waves which is interference. Richard Feynman suggested that '… there is no specific, important physical difference between them' [7]. When there are only a few sources, say two, we call it interference, as in Young's slits, but with a large number of sources, the process is called diffraction.

Diffraction is more than just wave bends around small obstacles. It can be described by the Huygens-Fresnel principle and the principle of wave's superposition, as shown in Figure 1-2. The propagation of a wave can be visualized by considering every point on a wave-front serves as a source of spherical secondary wavelets which spread out in the forward direction at the speed of light, such that the wavefront at some later time is the envelope of these

wavelets. When wavelets are added together, their sum is determined by the related phases as well as the amplitude of the wavelets, so that diffraction patterns usually have a series of maxima and minima.

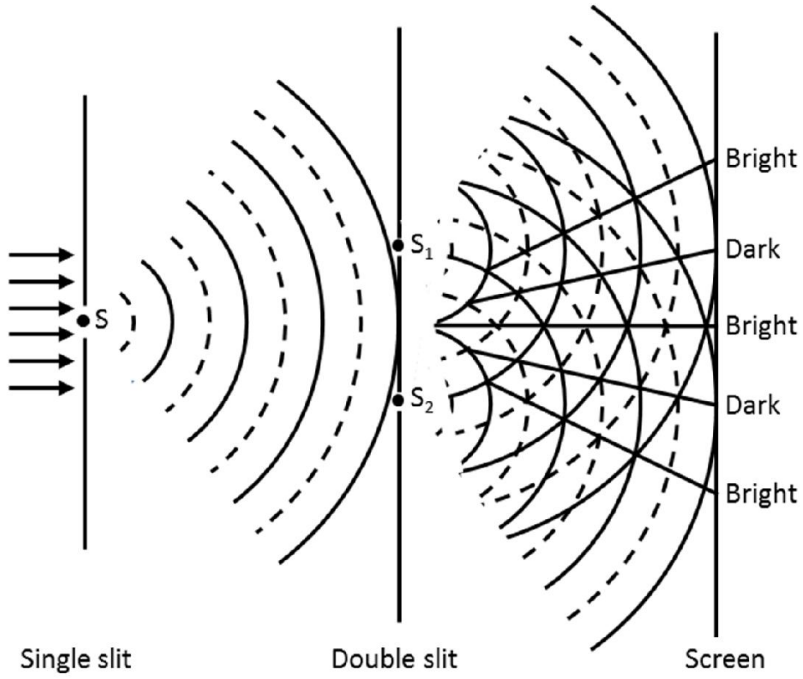

Figure 1-2 The famous double-slit experiment. Sub-waves from the two slits interference and form the intensity maxima and minima pattern.

Thanks to the developed technology, diffractive pattern of complex wavefront now can be simulated and computed to design diffractive elements for generating arbitrary distribution of wave energy, in both optics and sound. Applications examples will be given in Chapter 2.1.2 and Chapter 2.2.

6) Polarization

A wave is polarized if it oscillates in one direction or plane. The polarization of a transverse wave describes the direction of oscillation of the plane perpendicular to the direction of travel.

EM waves are transverse waves, can exhibit polarization; while sound waves are longitudinal waves, and cannot exhibit polarization, because the medium vibrates only along the propagation direction. The polarization state of

EM waves determines if spin angular momentum is present in the beam. More about spin angular momentum will be introduced in Chapter 2.7.

7) Dispersion

A wave undergoes dispersion when the phase velocity depends on the wave frequency. Dispersion is sometimes called chromatic dispersion to emphasize its wavelength-dependent nature and it leads to the chromatic aberration in optics. It is most easily observed by letting white light pass through a prism and results to a spectrum of rainbow colours. Even through dispersion is mostly described for light, it may occur for any kind of wave, such as sound waves.

8) Wavefront

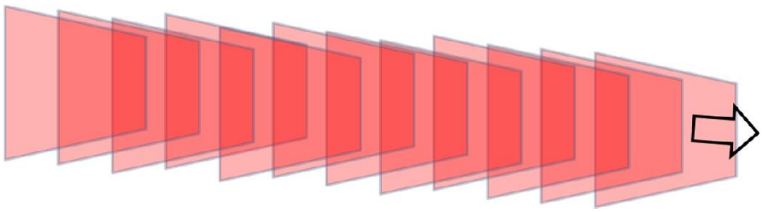

Figure 1-3 The wavefronts of a plane wave traveling in 3D-space.

A wavefront is the locus of points having the same phase: a line or curve in 2D, or surface for a wave propagation in 3D. The simplest form of a wavefront is the plane wave, where the wavefronts are infinite parallel planes of constant peak-to-peak amplitude normal to the propagation direction, as shown in Figure 1-3. Similarly, wavefront is not particular in optics but also in acoustics.

1.3 Structure of This Thesis

This thesis will contain seven chapters, in each of which wave modulation methods were used on optical or/and acoustic beams to fulfil certain applications. Most importantly, similarities between light and sound are employed, applied and investigated for those applications.

Chapter 2 of this thesis will give a background on the research been carried out on beam shaping and wavefront control for imaging and manipulation, in both optics and sounds.

Chapter 3 to 6 are four individual chapters, each of which will focus on a particular challenge, either with optics or ultrasound or both.

Chapter 3 describes the development of a Light-Sheet Tomography (LST) imaging system based on light sheet illumination, as well as continuous 3D imaging and tracking of plant roots.

A light-sheet illumination photoacoustic imaging system is described in Chapter 4. Three different optics for forming light sheet was compared and investigated for generating uniform beam profile along the sheet. High frequency PVDF transducer was fabricated for acquiring ultrasound signal for image reconstruction.

Chapter 5 describes the investigation of ratio between angular momentum and topological charge by creating and studying of helical acoustic beam with multi-element acoustic transducer array. This ratio was predicted in theoretical optics and acoustics, but has never been demonstrated in a single experiment. Because it needs accurate measurement of linear momentum and orbital angular momentum simultaneously, which is prohibitively hard with light because the ratio of the two momenta is not in the same magnitude.

Generation of non-conservative negative radiation pressure force (tractor beam) is a great interest but at the moment, most of the research is still theoretical. With the same transducer array, 'pulling' macro prism objects with plane Bessel-beam-like ultrasound beam is presented in Chapter 6.

Summary and future work are presented in Chapter 7.

Chapter 2

Background: Beam Shaping and Wavefront Control for Imaging and Manipulation

Even though optical and acoustic waves are not entirely the same, they share a lot properties in common. Hence it stands to reason that the principles or even techniques for optical and acoustic beam shaping can also be shared.

In this chapter, present techniques of beam shaping and wavefront control will be introduced, especially the similarities of these on both optical and acoustic waves will be highlighted.

2.1 Light Beam Shaping

2.1.1 Lasers and Gaussian Beam

The laser is perhaps the most important optical device developed in the last 60 year. Since its invention, it provided possibility of making optics one of the most rapidly growing fields in science and technology today. The word *laser* is an acronym of **l**ight **a**mplification by the **s**timulated **e**mission of **r**adiation. Based on amplification and stimulated emission, laser is capable of generating

electromagnetic wave with intense, highly directional, coherence, and nearly monochromatic energy.

The mode of a laser depends on the design of its optical resonator. Many lasers emit beams that approximate a Gaussian profile, called Gaussian beam which has the simplest and most popular optical resonator. Moreover, a Gaussian mode is the fundamental mode formed with spherical mirrors in an optical resonator. Its transverse electric field and intensity distribution (irradiation) are well approximated by Gaussian function. The mathematical function that describes Gaussian beam is a solution to the paraxial form of the Helmholtz equation, yielding the electrical field variation:

$$E(r,z) = E_0 \frac{\omega_0}{\omega(z)} exp\left(\frac{-r^2}{\omega(z)^2} - ikz - ik\frac{r^2}{2R(z)} + i\zeta(z)\right) \qquad \text{Eq. (2-1)}$$

Where r is the radial distance from the centre axis of the beam,

z is the axial distance from the beam's narrowest point (called the 'beam waist'),

$E_0 = |E(0,0)|$,

$\omega_0 = \omega(0)$ is the waist size,

$\omega(z)$ is the radius at which the field amplitude drops to 1/e of its axial value,

i is the imaginary unit (for which $i^2 = -1$),

$k = 2\pi/\lambda$ is the wave number,

$R(z)$ is the radius of curvature of the beam's wavefront and

$\zeta(z)$ is the Gouy phase shift, an extra contribution to the phase that is seen in Gaussian beam.

The corresponding time-averaged intensity distribution of Gaussian beam:

$$I(r,z) = \frac{|E(r,z)|^2}{2\eta} = I_0\left(\frac{\omega_0}{\omega(z)}\right)^2 exp\left(\frac{-2r^2}{\omega(z)^2}\right) \qquad \text{Eq. (2-2)}$$

Where $I_0 = I(0,0)$ is the intensity at the centre of the beam at its waist.

The constant η is the characteristic impedance of the medium is which the beam is propagating, for free space, $\eta = \eta_0 \approx 376.7\Omega$.

Since the Fourier transform of Gaussian distribution is still a Gaussian distribution, propagation of Gaussian beams through optical system can be treated almost as simple as geometric optics: the transverse distribution intensity remains Gaussian at every point in the system; only the radius of the Gaussian and radius of curvature of the wavefront change.

The geometry and behaviour of a Gaussian beam are governed by a set of beam parameters. The beam waist, which has the minimum beam diameter, is shown in Figure 2-1. Gaussian beam either diverges from or converges to this beam waist. Under the laws of geometrical optics a bundle of rays (a beam) converging at an angle of θ should collapse to a point. Because of diffraction, this does not occur. However at the intersection of the asymptotes that define θ, the beam diameter reaches a minimum value $d_0 = 2\omega_0$, the beam waist diameter.

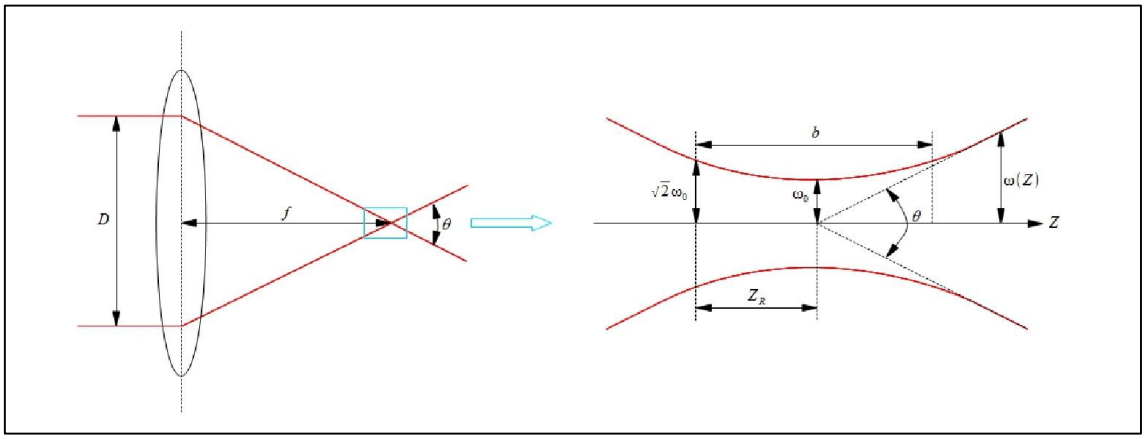

Figure 2-1 Gaussian beam waist diagram

Here we assume θ is small, so that half angle

$$\frac{\theta}{2} \approx sin\frac{\theta}{2} \approx \tan\frac{\theta}{2} = \frac{D}{2f} \qquad \text{Eq. (2-3)}$$

Where f is the focal length; D is the width of incoming light beam.

The beam waist diameter depends on the beam divergence angle as:

$$d_0 = 2\omega_0 = \frac{4\lambda}{\pi\theta} = \frac{4\lambda f}{\pi D} \qquad \text{Eq. (2-4)}$$

Where λ is the wavelength of the beam.

There is another important parameter in beam shaping which is numerical aperture (NA). NA is a dimensionless number that is defined to characterise the range of angles over which a lens can accept or emit light. NA is usually defined as the sine of the half angle multiplied by the refractive index of the medium:

$$NA = nsin(\theta/2) \qquad \text{Eq. (2-5)}$$

Where n is the index of refraction of the medium in which the lens is working.

The wavefront of a Gaussian beam at its beam waist is usually considered as planar, i.e. with infinite radius of curvature, which becomes finite and initially decrease with z, the distance from the beam waist on the propagation axis. At the Rayleigh length, the radius of curvature reaches a minimum value, then increase with larger z, eventually becoming proportional to z.

The Rayleigh range of the beam is:

$$z_R = \frac{\pi\omega_0^2}{\lambda} = \frac{4\lambda}{\pi\theta^2} = \left(\frac{4\lambda}{\pi}\right)\left(\frac{f}{D}\right)^2 \qquad \text{Eq. (2-6)}$$

At a distance from the waist equal to z_R , the diameter of beam spot is $\sqrt{2}$ the diameter at beam waist, i.e. $\sqrt{2}d_0$.

In practice, a Gaussian beam is tuned to be collimated so that the radius of the beam maintains constant in a reasonable length, i.e. divergence of the beam is minimised. Under this condition, wavefront of collimated beam is considered approximately planar.

Gaussian beams are just one possible solution to the paraxial wave equation. Other solutions to the paraxial form of the Helmholtz equation exist. Solving the equation in Cartesian coordinates leads to a family of solution well known as Hermite-Gaussian (HG) modes, while solving the equation in cylindrical coordinate leads to Laguerre-Gaussian (LG) mode. For both families, Gaussian beam is the lowest-order solution, while higher-order transverse modes are higher-order solutions in optical resonator.

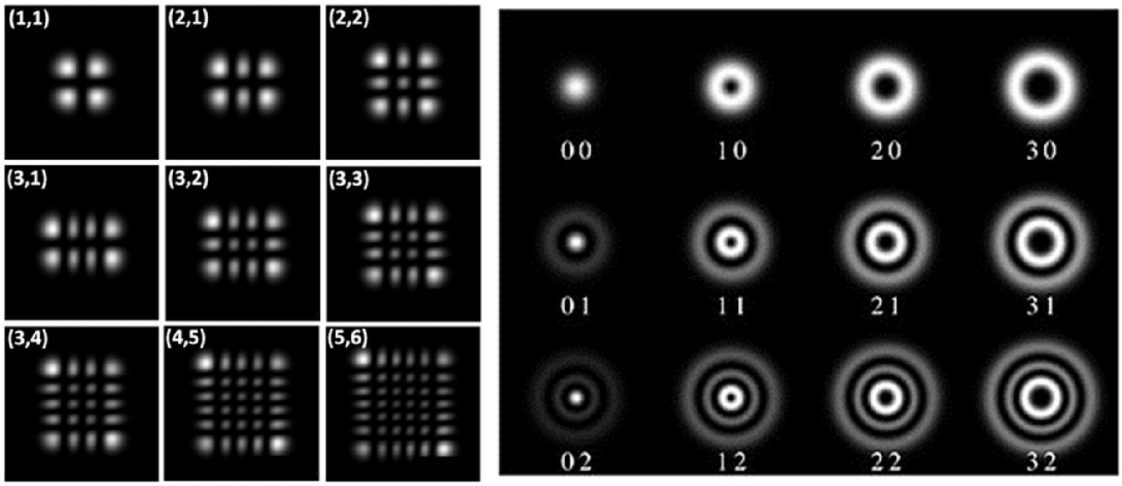

Figure 2-2 Transverse intensity distribution of higher-order Hermite-Gaussian modes [8] (left) and higher-order Laguerre-Gaussian modes laser beams (right).

Hermite-Gaussian modes are a convenient description for the output of lasers whose cavity design is not radially symmetric, but rather has a distinction between horizontal and vertical. If the symmetry is cylindrical, the natural solution of the paraxial wave equation are Laguerre-Gaussian mode. Different from HG beams, LG modes have helical phase along their propagation axis and carry an intrinsic rotational orbital angular momentum, which can be applied to rotate objects in optical tweezers [9].

Transverse electric field and intensity distribution of laser beams with higher-order transverse mode are shown in Figure 2-2. In the general case, if a complete basis set of solution is chosen, any real laser beam can be described as superposition of solution from this set. Although a wide range of beams can be produced directly from an optical cavity, the mode is still restricted to solutions of the wave equation. Arbitrary control of beam is not possible and especially dynamic control is very challenging. Hence other ways to perform beam shaping are needed.

2.1.2 Beam Shaping Optics

The earliest artificial beam shaping tool, the mirror, made from obsidian has been dated to around 6000 BC [10]. The oldest lens artefact can also be dated back

2700 ~ 2800 years, which were used as magnifying glass or as a burning-glass to start fires by concentrating sunlight [11]. The study of refraction is from 50 A.D. by Cleomedes and later by Claudius Ptolemy (130 A.D.) of Alexandria, even though the quantitative explanation of refraction was not described until the 10th century by Ibn Sahl [12] and later named and well known as Snell's law (Eq. (1-3) in 16th century.

In the early stages from the 13th century, lenses were widespread because of the invention of spectacles for vision correction. Quality of the lenses was improved only on empirical knowledge instead of optical theory [13]. The development of lenses led to the invention of the compound microscope and telescope around the 16th century. Later on, optical theory on refraction showed that spherical surface could not focus light perfectly onto a point, due to spherical aberration. This led to the study on aspherical lenses, which has complex surface profile to reduce or eliminate spherical aberration.

Refraction optics such as converging and diverging lenses are still the most common tools for shaping light beams. Moreover, there are other ways to modify light beams for special purposes.

Spiral phase plate (SSP) [14] can convert a fundamental mode Gaussian beam to a beam with spiral wavefront, i.e. a Laguerre-Gaussian beam. A spiral phase plate is made of a dielectric material which is transparent, and has a thickness which varies circularly around the plate, but is radially uniform. The thickness variation enables the spherical phase front of Gaussian beam turned to a spiral pattern, thus introduces angular momentum into the beam [15], which can be employed to rotate objects. More details will be given in Chapter 2.7 and Chapter 4.

Axicon lens is used to focus a Gaussian beam to a Bessel-Gaussian beam. A Bessel beam is a kind of wave whose amplitude is described by a Bessel function of the first kind. It can be an electromagnetic or acoustic beam. Creating a true Bessel beam with a plane wave would require infinite amount of energy because

it is unbounded. Axicon lens could make good approximation of it. With Bessel beam's non-diffractive and 'self-healing' (the beam can reconstruct after obstacle) properties, it is playing an increasingly important role in optical tweezing [16], [17] and microscopies [18].

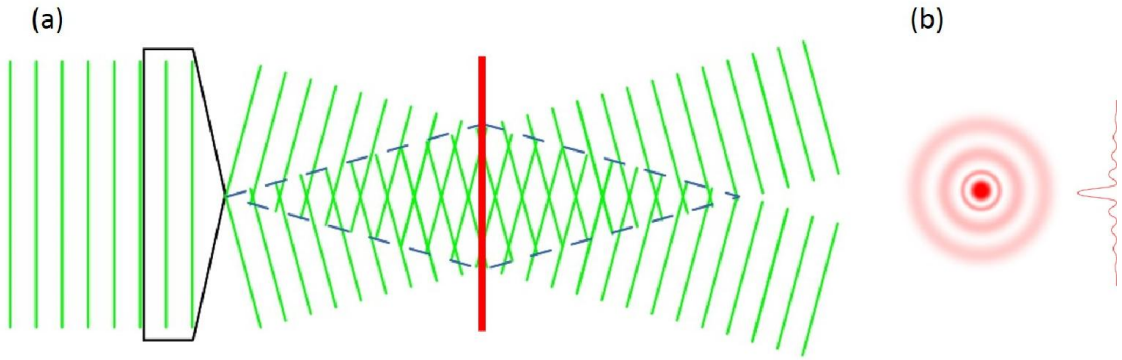

Figure 2-3 Graph of Bessel beam generation. (a) Bessel beam generated from Gaussian beam with Axicon lens. The diamond area indicates the section with Bessel profile. (b) Bessel profile at the position indicated by red line in (a).

Diffractive optical elements (DOEs), which are thin phase elements that operate by means of interference and diffraction to produce arbitrary distribution of light or to aid in the design of optical systems, are an important family of optical shaping elements. The transition from refraction with a normal lens to a diffractive optical element can graphically be understood by removing material which causes a phase delay of a multiple of the used wavelength. An approximation of DOEs is Fresnel lens [19], as shown in Figure 2-4.

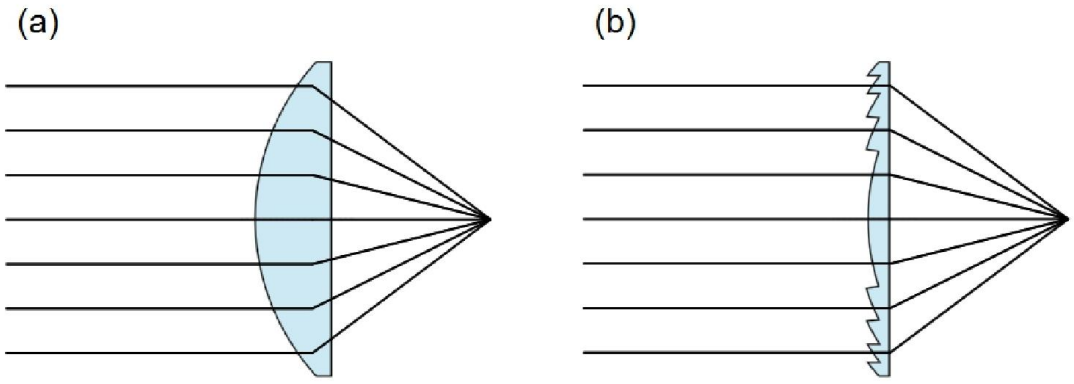

Figure 2-4 Comparison of (a) normal concave lens and (b) Fresnel lens

When a light beam normally incidents the plano side of a plano-convex lens, it would be focused to a spot on the other side of the lens. When the aperture is large and focal length of the lens is short, thickness of the lens would be large and that requires a large quantity of material. Fresnel lens has the same effect of plano-concave lens but allows the construction of large aperture and short focal length without the mass and volume of material that required by a conventional lens. DOEs works in a similar way, although the thickness of DOEs is usually in the wavelength level. For instance, for a phase-only DOE, encoding a two-dimensional optical element on it is accomplished by changing the optical path of incoming light beam at different area. Figure 2-5 shows the phase pattern on a DOE for creating the effect of an Axicon lens, which essentially is isometric concentric ring pattern.

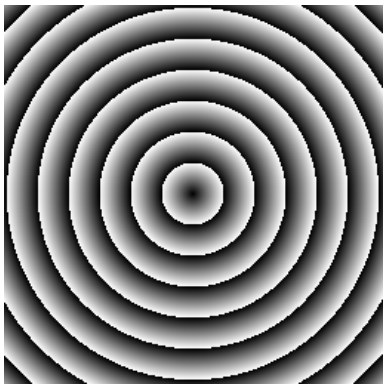

Figure 2-5 Phase pattern on a DOE for the effect of an Axicon lens.

A more general description of DOEs is that they are creating a desired holographic pattern. Holography enables 3D images (holograms) to be made. Traditionally, a hologram is created by interfering a reference beam and an imaging beam reflected from a 3D object. The hologram has both phase and amplitude information of the 3D object. By applying the reference beam onto the hologram, a 3D image of the object can be reconstructed, as shown in Figure 2-6. However, the 3D is not obligatory to create hologram; patterns on DOEs can be computed by working backwards from the desired 3D pattern.

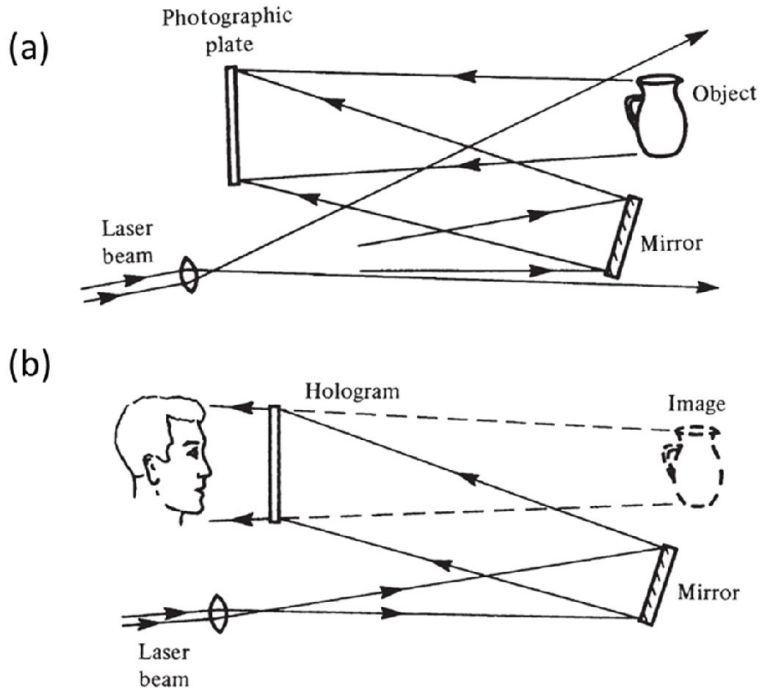

Figure 2-6 Hologram (a) Hologram recording: the photographic plate record the phase information by recording the interference pattern produced by the reference beam and the light waves scattered by the object. (b) Image construction: using the same reference light source, light diffracted by the hologram reconstructs the object wave [20].

Hence, a DOE can theoretically produce an arbitrary distribution of light. In real applications, DOEs are designed as beam splitters to split a laser beam into an array of spots; or line generators to generate a line with even amplitude, or diffusers to provide controlled illumination for specialized application, or Pitch-Fork hologram to generate LG beams.

Figure 2-7 Figure of commercial spatial light modulator from Boulder Nonlinear Systems (Photo source: Laser2000.se)

The invention of the liquid-crystal (LC) spatial light modulator (SLM) is a great milestone for beam shaping. Figure 2-7 shows a commercial spatial light modulator from Boulder Nonlinear Systems. An SLM is a device that modulates the phase and/or amplitude of a light beam. It can be thought as a dynamic DOE. The working area of an SLM is divided to little pixels. Each pixel is made of liquid crystal and controlled independently. By applying voltage on the liquid crystals, the orientation of the liquid crystals change, thus the phase states of light beam on each pixel changes because of birefringence of liquid crystal. Light beam is transmitted or reflected by the SLM is modulated to desired phase. By reconstruction of the light field, light beam is shaped as desired, such as diverging, converging lens, optical grating, spiral phase plate or Axicon lens. SLM has also been used to generate desired complex wavefront to calibrate the distortion in the optical system [21], [22].

As it is dynamic, the profile on an SLM can be updated in real time. This makes it particularly useful for aberration correction [23], not only in optical system [24], but also in turbid tissue *in vivo* [22] to help achieving better resolution and deeper penetration.

The refresh rate of some models can be up to 100 Hz or even more, which means SLMs can be used as an 'active' element for real time calibration and control. Since its appearance, SLM, as a hologram, has been widely employed in areas, for instance, creating 3D trapping pattern for 3D trapping in optical tweezers [25]. SLMs are also used to create Bessel or Airy beams with a ring or cubic-phase pattern respectively at the Fourier plane of a convex lens.

2.2 Acoustic Beam Shaping

As mentioned above, acoustic and optical beam share many similar properties. Hence shaping of acoustic beam is similar to that of optical beam from many aspects. Currently, ultrasound beam shaping depends on three main

approaches, which are (a) modifying the shape of transducer elements, or (b) introducing 'acoustic lens' for refraction of ultrasound beams, or (c) building transducer array with multiple elements, then construct desired beam through controlling phase of each element.

To minimise the acoustic loss at the interface between different components, the ultrasound setup is usually immersed in water to use water as a coupling medium. Still, the loss at interfaces and high acoustic attenuation restricts the working distance of ultrasound waves. Hence the numbers of acoustic shaping components needs to be minimised. In practise, ultrasound beam shaping is usually accomplished within the process of acoustic beam generation, instead of shaping it afterwards in light beam. In acoustic applications, this is usually called 'beam forming'.

Spherical shell transducers used in early high intensity focused ultrasound (HIFU) surgery [26] are examples of shaped transducers [27]. HIFU is a high-precision medical procedure that applies high-intensity focused ultrasound energy to locally heat and destroy diseased or damaged tissue. The single-element shell transducers allow focusing of acoustic beam at a single focal point with a diameter on the order of a wavelength, i.e. a few millimetres with frequency in MHz range.

Analogous to optical lenses, acoustic lenses are used to produce a sharp focus, especially in high resolution imaging devices to increase the lateral resolution which is determined by the size of focal point [28]. The lenses are usually placed right before the transducer and made of plastic, epoxy, rubber or liquid. Acoustic lenses are not as popular as optical lenses, because there are some disadvantages, for example (1) the lenses add volume in front of transducer, (2) multiple reflections between the lens surfaces causes reverberation and (3) the lenses introduce significant attenuation [29].

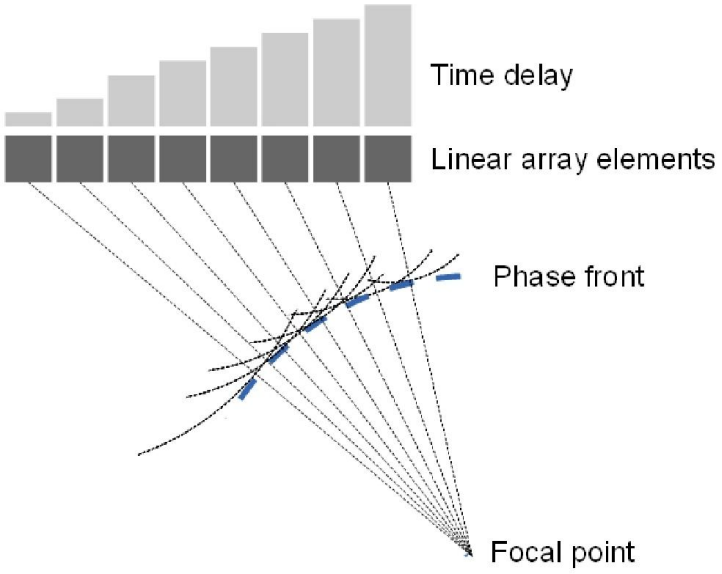

Figure 2-8 Graph of phase array. Independent phase control of each element leads to the forming of desired beam.

Phase-array transducers are composed of multiple elements that can transmit sound wave independently at different time. To control the shape of sound beam (usually the focal point of the beam), time delays are applied to the elements to create constructive interference of the wavefronts, similar to diffractive optical element. The principle is illustrated in Figure 2-8. Since it is based on the construction of waves, it is not exclusive in acoustic wave. For instance, phase array antennas are used in radar produce a directive radiation pattern. As a dynamic device, the counterpart of phase array in optics is the SLM. Hence similarly, acoustic phase array can be used for aberration correction as well, just like SLM in optics. However, the switch time needed for phase-controlling in acoustic phase array is much longer than SLM. This limited the real-time applications of acoustic phase array. Phase array is both the acoustic source and modulator while SLM is only the modulator with light.

Although phase array technology has been used for nearly 20 years [30], the principle behind it did not change. Nevertheless, benefitting from modern computing and manufacturing ability, array with more elements, more compact design and finer control can be produced. Phased arrays allow fast scanning of

the focal point, thus it is employed in many application such as medical ultrasonography, non-destructive testing (NDT), and HIFU.

Early transducers used in HIFU are single-element transducers with shell shape generating focused ultrasound. Their ablation is limited to the focal point, thus for multi-position application like large area treatment, the transducer need to be moved mechanically, which causes increase of operation time and decrease of surgery accuracy. Phase array transducers are able to dynamically change the heat distribution in targeting area and sonicate multiple points in sequence without relocating. Independent controlling of the active elements brings great opportunity for correcting aberration caused by the tissue, to maximise the energy at targeting area and helping increase penetration depth of the acoustic beam.

ExAblate 2100 conformal bone system is one of the latest HIFU systems designed for bone tumour surgery and features a 1000-element transducer. It will be used as beam generating and forming tool in Chapter 5 and Chapter 6.

Nevertheless, properties of light and sound waves are similar. Keeping the slightly difference in mind, applications in light could be applied in sound, and *vice versa*. To achieve these, optical and acoustic beams are shaped as desired. Imaging and manipulation, with optical and/or acoustic beam, will be discussed in this thesis.

2.3 Interaction of Light and Sound

Under most circumstances, light and sound was investigated separately, due to difference mechanisms. However, it is not found until late 19th century and early 20th century that, light and sound does interact with each other, results in photoacoustic (short as PA or optoacoustic) effect and acousto-optics effect, respectively.

PA effect is the formation of sound waves following light absorption in material sample. There are several different mechanisms to cause PA effect, however usually only one is concerned, photo-thermal effect, which is the primary mechanism. When the sample is illuminated with pulsed or periodical light, it absorbs the energy of light then results in localised temporal temperature rise, which causes volume expansion and contraction, and ultimately produces sound waves.

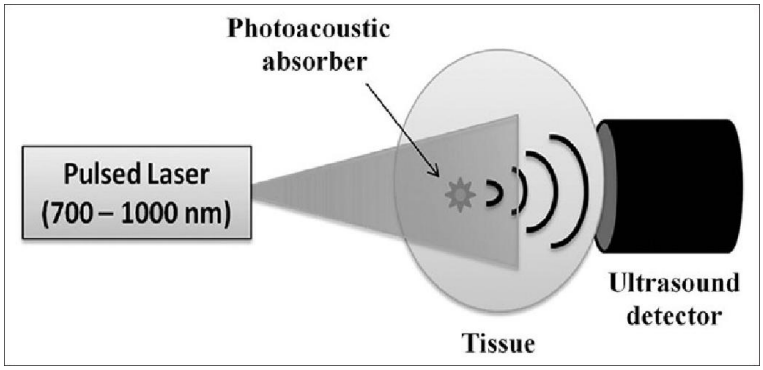

Figure 2-9 Illustration of photoacoustic effect [31].

PA effect has found its applications in many areas. One important area is to form images by acquiring the acoustic signals from the sample. This will be further discussed later in Chapter 2.6 and Chapter 4. Apart from imaging, PA effect has many other applications, such as for measuring light absorption spectrum, particularly for transparent sample where light absorption is very small [32].

Acousto-optics effect is essentially based on the change of the refractive index of a medium due to the presence of sound waves in that medium. Sound waves produce variation in the refractive index in the medium due to pressure fluctuation, and result in refractive index grating. This grating may be detected optically by refraction, diffraction and interference effect [33].

Due to the increasing availability and performance of lasers, acousto-optic effect has been used in many areas for the deflection, modulation, signal processing and frequency shifting of light beams, in the form of devices such as

acousto-optic modulator (AOM), acousto-optic deflector (AOD) and acousto-optic filter (AOF). For example, AODs are used in optical trapping with the high scanning speed for multiple-particle trapping, and in digital scanning light-sheet microscopy (DSLM) for creation of the light sheet by scanning a beam [34].

2.4 Optical Imaging

2.4.1 Traditional Optical Imaging Microscopies

Lenses have been employed to help the eye for more than 2000 years. Combining lenses leads to the invention of imaging systems, including microscopes.

The microscope is the instrument that people use to observe small objects or details of objects so small that cannot be seen by the naked eye. The scientific research about microscope is called microscopy. There are several kinds of microscopes: optical microscope which use light to image sample, or electron microscope which images samples with an electron beam, scanning probe microscopes such as scanning near-field optical microscope (SNOM) and atomic force microscope (AFM), and other microscopes. In this thesis, we will only focus on optical microscopes.

It is difficult to address who invented the microscope. It is often said that the first microscope was invented around 1590 by Dutch spectacle-maker Zacharias Janssen with help from his father Hans. They put several lenses in a tube and found that the object near the end of the tube appeared to be greatly enlarged, much larger than any simple magnifying glass could achieve. This microscope consisted of a converging lens and a diverging lens [35]. His microscope was capable of magnifying images about three times to ten times. Although it was rudimentary compared to a modern microscope which can easily achieve more than 100X magnification, Janssen's microscope was a great advance from single lens magnification. The use of two converging lenses was

suggested later and this arrangement forms the basis for the *compound microscope* which uses multiple lenses to collect light from specimen and then another lens to further enlarge the image of the specimen.

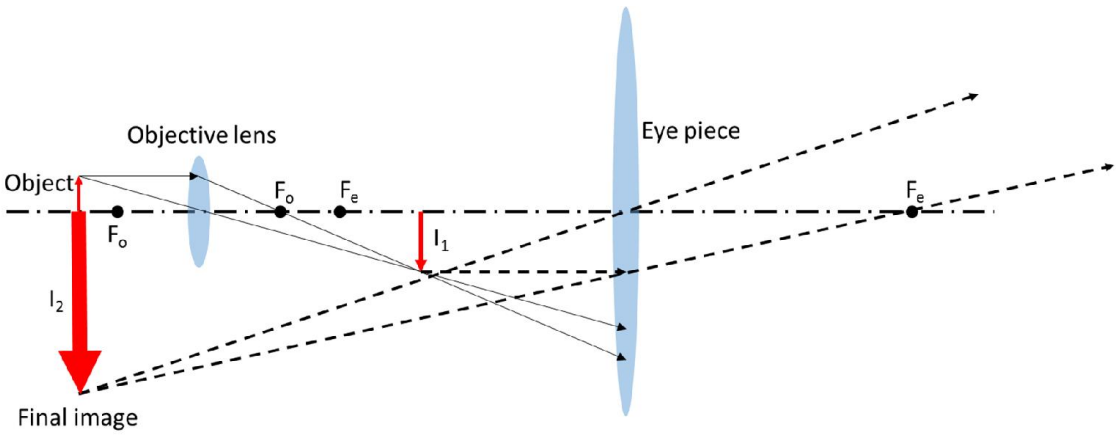

Figure 2-10 Principle of a conventional microscope.

The principle of a conventional microscope is shown in Figure 2-10. The observed target is mounted on a stand below (on the left of the graph) the microscope tube, which holds the objective lens and eye piece. The objective forms a real inverted and magnified image (I_1) of the object. The eyepiece acts like a magnifying glass and forms a virtual and magnified image (I_2) of the object.

Quality of the early microscopes was limited by the ability of manufacturing good optics. By late 17th century, another Dutch scientist Anton van Leeuwenhoek found a way to create very small, high-quality glass spheres as his lenses. Using those tiny lenses, he was the first to observe and describe single cells, muscle fibres, bacteria, microscopic blood vessels, etc. [36].

Ideally a convex lens should be able to focus light beam uniformly to a single point. Realistically, however, spherical and chromatic aberrations of lenses make it hard. Spherical aberration happens when the light rays strike the edge of lens, in comparison with those that strike near the centre; while chromatic aberration is due to the refractive index difference of different wavelength. With

more lenses introduced into microscopes, spherical and chromatic aberration was greatly reduced in the 18th and early 19th century, respectively [37].

Then, it was soon realized that the maximum resolution of a microscope is limited by the diffraction limit, which is related to the wavelength of light. In 1878, Ernst Abbe formulated a mathematical theory correlating resolution to the wavelength of light:

$$d = \frac{\lambda}{2NA} \qquad \text{Eq. (2-7)}$$

His formula makes it possible to calculate the maximum resolution in microscope [38].

In 1902, this observation limitation was overcome by the invention of the *ultramicroscope* by Richard Adolf Zsigmondy and Henry Siedentopf. Ultramicroscope is dark-field microscope based on light scattering. The background in ultramicroscope is left in dark and only scattered light from particles can be observed. It allowed the study of micro-particles with the size below or near the wavelength of light which is around 500 nanometres [39]. It is worth noticing that though the ultramicroscope enables observation of particles smaller than diffraction limit, the images of the particles are still bigger than diffraction limit. Along with the development of technology, now there are ways to break the resolution limitations with super resolution technology [40], [41] such as Structured Illumination Microscopy (SIM), Stimulated Emission Depletion (STED) microscopy and Photo Activated Localization Microscopy (PALM).

2.4.2 Modern Optical Microscopies

Driven largely by progress in areas like biology, there is increasing demand for microscopies for better contrast and resolution, both in time and space. Fortunately, since the invention of laser and other digital technology from the 1960s onwards, new types of modern microscopies have been developed:

1. Confocal Microscopy --- It is an optical imaging technique that uses point illumination and a pinhole to eliminate out-of-focus signal to increase optical resolution and contrast in the image. Both the axial and the lateral resolution in confocal microscopy are significantly enhanced. Another feature of confocal microscopy is its 'optical sectioning' ability, which refers to the ability to acquire images from a selected depth within a sample without mechanically sectioning. This also enable confocal microscope to construct 3D image of the sample. With highly enhanced resolution in confocal microscopes, sub-micrometre resolution can be easily achieved. Some form of confocal microscope setup can even break the diffraction limit [42] such as STED microscopy.

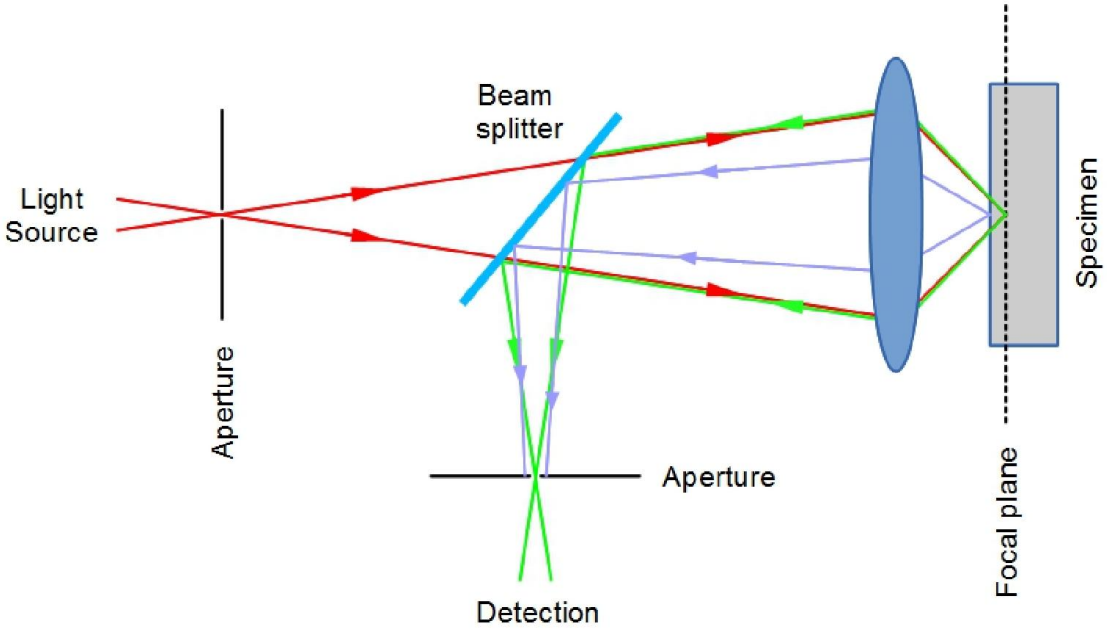

Figure 2-11 Confocal scanning principle

Since the idea of confocal microscopy was first introduced in 1957 [43], confocal scanning microscopy is becoming the most common and typical kind of modern microscopy. Confocal microscopy is now a routinely used optical technique across a wide range of biological science, from plant science to mammalian models. Its popularity is from its benefits over conventional wide field microscopy, the ability of removing out-of-focus signal, both in lateral and

depth of focus, imaging optical sections in thick samples and so creating high contrast 3D images. Because confocal microscopy has gained significant success, the performance of it is usually considered as benchmark for other microscopies.

Since only the signal very close to the focal plane can be detected in a confocal microscope, the resolution of the image, especially the axial resolution along the depth direction, is highly enhanced. However, the "trade-off" of this technique is that the imaging speed is considered rather low. To get a 2D image, the microscope needs to "scan" the whole interested area, as every time only a small point can be imaged. Additionally, the whole specimen is illuminated even though only a small part is imaged, this introduces great phototoxicity to the specimen. Last but not the least, as most of the light is blocked by the pinhole, the detected light intensity is low, which means longer exposure is often needed. This limits the use of confocal microscopy under conditions when fast acquisition is required, such as live cell and embryo development imaging.

Spinning disk confocal laser microscopy (SDCLM) increases the imaging speed of confocal microscope. Instead of mechanically scanning the narrow beam in confocal scanning microscopy, in SDCLM an expanded beam illuminates an array of micro-lenses arranged on a disk. Spinning disk could simulate the effect of mechanically scanning the laser beam to enable high imaging speed [44].

2. Multi-photon Excitation Microscopy --- It is a fluorescence imaging technique that uses multiple long-wavelength photons to excite one molecule in fluorescent dyes. The excitation of fluorophore needs the photons to have certain amount of energy which is defined by $E = hc/\lambda$. Hence the photons need to have certain wavelength. In multi-photon excitation microscopy, every excitation involves more than one photon; the energy of two or more photons is absorbed to excite one electron, then emits a photon from the fluorophore. Usually infrared light is employed for the benefit of penetration depth. Since excitation only happens with high intensity, usually at the focal point, background signal is highly suppressed. However, similar to confocal microscopy, the imaging speed

of multi-photon excitation microscopy is limited, because only one small point is under imaging at one time [45].

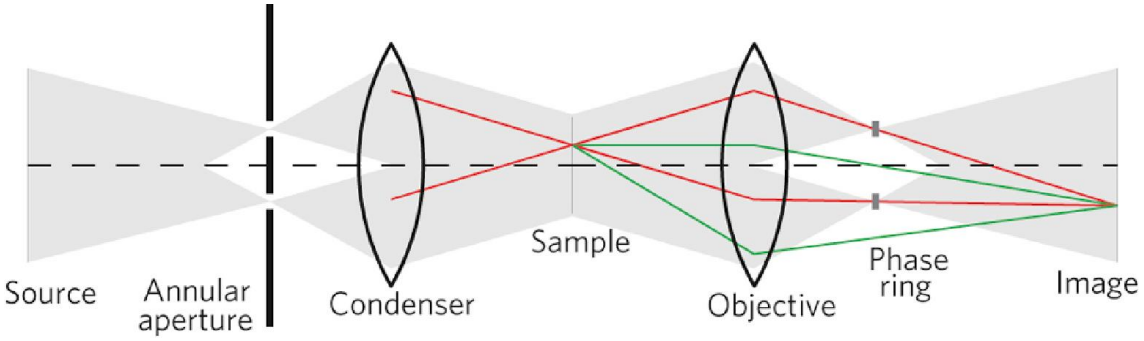

Figure 2-12 Principle of phase contrast microscope [46]

3. Phase contrast microscopy – It converts phase shifts in light passing through a transparent specimen to brightness changes in the image to enhance the contrast in image, as shown in Figure 2-12. In phase contrast microscope, illumination light (red) is shaped to a ring with condenser annulus, thus light from the specimen (green) will be scattered while the background light (red) is still kept as ring shape to be distinguished. Background light is tuned by phase shift ring. In some phase contrast microscopes, background light is further dimmed by another neutral density filter ring. Those two steps largely suppress the background light while highlighting the scattered light to emphasis the details in the observed sample. Phase contrast microscope reveals many cellular structures that are not visible with simple bright field microscope without staining which would affect or even kill the cells.

3. Light Sheet Microscopy --- It is also called Selective/Single Plane Illumination Microscopy (SPIM), or Light Sheet Fluorescence Microscopy (LSFM). It illuminates the target with a thin light sheet and the optical detector detects the illuminated plane at perpendicular axis.

Light sheet microscopy is also featured with optical sectioning ability, as the same in confocal microscopy, for only the illuminated part can be detected while the rest is left in dark. Axial resolution of light sheet microscopy is

determined by the thickness of the light sheet, which is from illumination part and independent from the detection unit. This means without high NA objective, high lateral resolution can still be achieved. Low NA objectives are providing larger field of view. These all made light sheet microscopy suitable for imaging large 3D sample.

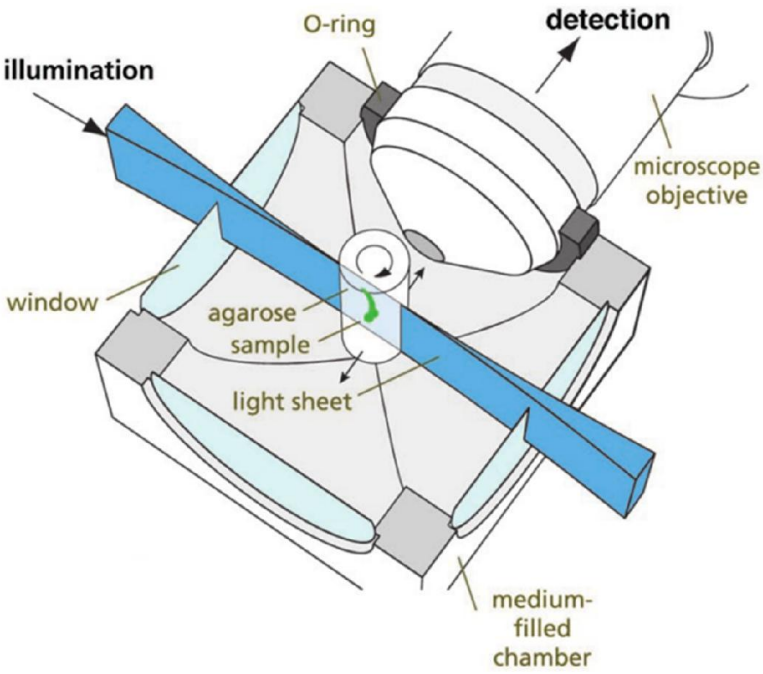

Figure 2-13 Schematic of sample orientation in SPIM [47]. The sample is embedded in a cylinder or syringe of agarose gel, which is held on a translation and rotation stage. The agarose cylinder is immersed in an aqueous medium that fills the chamber, and the solidified agarose is extruded from the syringe for imaging.

In addition, at every time point, only a thin layer of the specimen is illuminated and detected, thus the photo-toxicity and photo-bleaching are significantly reduced, which is a great improvement from both wide-field and confocal fluorescence microscopy. Since a 2D image is captured at a time, the imaging speed is greatly boosted. These features make LSFM suitable for long-term monitoring the development of samples.

It is only possible that with the progress in technology of computing power and camera performance that, LSFM can realized its potential in the last few

years. As a latterly developed method, light sheet microscopy's full potential is still being exploited. Other technologies, such as multi-photon excitation and structured illumination, are integrated into LSFM and make it capable of delivering even better results. Even though the lateral resolution LSFM providing is not as promising as confocal microscopes, and it has not overcame the diffraction limit, yet, LSFM with Bessel-beam illumination is pushing it to the edge and has achieved 0.3 μm lateral resolution [18].

2.4.3 Modern Microscopies Based on Beam Shaping

Along with general technology improvement, for instance in computing ability, camera performance and quality of optics, advanced beam shaping techniques in microscopies further enhance the resolution and even break resolution limitation, for example, in stimulated emission depletion (STED) microscopy and structured illumination microscopy (SIM). By scanning Bessel beam to create light sheet, Bessel beam light sheet microscopy can take advantage of self-reconstruction property of Bessel beam and increase penetration of light sheet into thick samples.

1. STED is a fluorescence microscopy technique which uses a combination of light pulses to induce fluorescence in a small sub-population of fluorescent molecules in a sample. In laser scanning fluorescence microscope, the resolution is determined by the size of excitation spot, which yields at diffraction limit. STED employs DOEs to generate LG beam with a doughnut shape ring to deplete fluorescence, and leave the centre area remaining allowing fluorescence, which can be smaller than diffraction limit spot. Thus it is able to achieve resolution better than the traditional confocal microscope. Lateral resolution of STED is typically between 30 to 80 nm, despite that values down to 2.4 nm have been reported [48]. Using different DOEs, lateral resolution on the order of 100 nm have been demonstrated [49]. However due to the low scanning speed and high exposure to the laser energy in STED, it is not suitable for live cell imaging.

2. Structured illumination microscopy – The main concept of structured illumination is to illuminate sample with patterned light and increase the resolution by measuring the fringes from the interference of the illumination pattern and the sample. Commercial structured illumination microscopy is only able to enhance the resolution by a factor of 2 to 100 nm, but it is easy to use because there is no specific requirement for the dye or sample preparing, which largely simplifies the process.

Saturated structured illumination microscopy (SSIM) exploits the nonlinear dependence of fluorophore emission rate on the intensity of the excitation laser. With the sacrifice of causing more photo-damage, SSIM is able to provide less than 50 nm lateral resolution.

Rather than thinking SIM of a type of microscopy, it is better to consider it as a kind of technique that can be adapted onto main other microscopies and increase resolution in common sense. For example, SIM is applied onto light-sheet microscopy in the form of digital scanning light sheet microscopy-structured illumination (DSLM-SI) [50].

3. Bessel beam illumination (BBI) – Similar to structured illumination, BBI is also a kind of illumination technique that can be applied onto various microscopies. There are several ways to create Bessel beam, includes the Axicon lens introduced before, DOEs and SLM. The main advantages of Bessel beam illumination are non-diffractive and self-reconstruction. Thus the negative effect of scattering on the light sheet is reduced and penetration of light sheet into thick samples increases at the same time.

Above techniques are only examples of beam shaping in modern microscopies; even for a certain class, there are multiple ways to realize it. Since it is not possible to cover all of them in this thesis, only these are most relevant to this thesis are introduced for a brief impression.

2.5 Acoustic Imaging

Acoustic imaging usually employs ultrasound as the probe, hence it is also called ultrasound imaging. Ultrasound is sound wave with frequency greater than the upper limit of the human hearing range which is approximately 20 kHz.

Speed of sound is approximately 343 m/s in air and 1484 m/s in water, both at 20 °C. It is 6 orders of magnitude lower than the speed of EM waves, which allows time of flight measurement much more easily in ultrasound, hence allowing the pulse echo recording for acoustic imaging. Acoustic imaging is through constructing echo signals, as shown Figure 2-14. Thus the contrast mechanism in acoustic imaging is based on impedance variation between different materials, which is not affected by optical transparency. This enables ultrasound imaging a useful tool for imaging opaque samples. Moreover, sound experiences much lower scattering than light because of its long wavelength. This makes the penetration of ultrasound imaging much deeper than optical imaging.

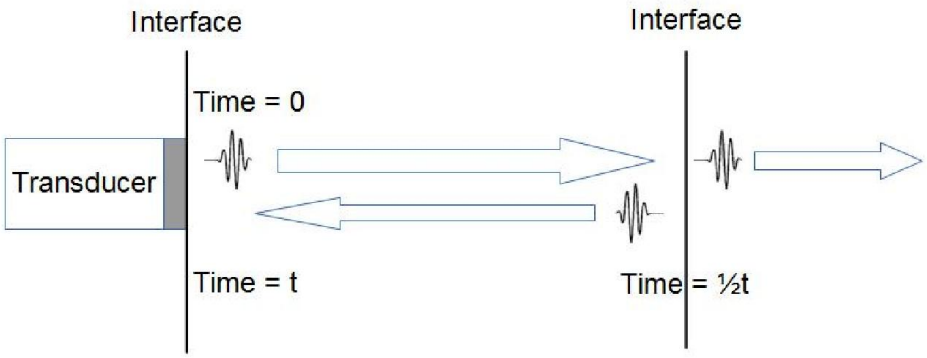

Figure 2-14 Sound imaging echo construction diagram

In traditional acoustic imaging method, to create an image, three steps are needed: (1) An ultrasonic wave is generated by a transducer. (2) Part of the wave is bounced back as echoes when it encounters acoustic impedance difference layer and received by transducer. (3) Images are produced with the echoes. This will solve the information on a 1D dimension. To increase the imaging speed,

there are usually phase array transducers in the ultrasonography probe to send sound pulses and receive echoes, enables real time 2D scanning.

In general, penetration depth of imaging system increases with the increase of wave wavelength, because with longer wavelength, there is less scattering, smaller attenuation coefficient, and stronger diffraction. This brings deeper penetration of ultrasound scanning than optical imaging methods due to the long wavelength of ultrasound. On the other hand, spatial resolution decreases with the increase of beam wavelength. Thus ultrasound imaging is more suitable for imaging large objects, for instance the human body. Another benefit of ultrasound imaging is that it is non-invasive when compared to radiography which employs X-ray and brings ionising radiation to the target.

Ultrasound scanning, being widely used in medical diagnosis, typically works in 2 to 18 MHz range to produces images of the internal organs, vessels and tissues. Medical ultrasonography is capable of penetrating into the body, enabling imaging deep organ structures such as liver and kidney. Although the resolution is not as promising as optical imaging, ultrasonography is still able to provide enough information for medical diagnosis or even perform therapeutic procedure.

Frequencies up to 50 – 100 MHz are used experimentally in bio-microscopy [51] to provide even higher image resolution, however, with the trade-off of penetration depth.

2.6 Hybrid Optical and Acoustic Imaging

Photoacoustic Microscopy (PAM) is also called Optoacoustic Microscopy, which is based on photoacoustic effect, as introduced in Chapter 2.3. When the sample is illuminated with a pulsed laser it will absorb the energy of light, then generate sound waves due to a thermal expansion. The acoustic waves can be detected by an ultrasound transducer and then used to form images.

The motivation for photoacoustic imaging is to combine ultrasonic penetration depth and high optical contrast due to optical absorption. In pure optical imaging, optical scattering degrades spatial resolution dramatically with depth. On the contrary, ultrasound scattering is two to three orders of magnitude weaker than optical scattering in biological tissues, thus ultrasound can provide a better resolution in depth greater than 1 mm. Pure ultrasound image construction is based on the detection of mechanical properties of the sample and often produce weak contrast, while contrast in PAM is based on optical absorption, which is related to the molecular composition of the tissue. For example, high optical absorption in oxygen saturation and haemoglobin provides high contrast for imaging microvascular network in tissue.

Upon absorption of a short laser pulse, the whole imaging area is simultaneously excited by thermoelastic expansion and generates acoustic pressure. The acoustic waves from the initial acoustic source reach the acoustic transducer with various time delays which depend on the distance between the sources and the transducer. The time delay is used for image forming, the same as in ultrasound imaging.

The imaging depth of photoacoustic imaging is mainly limited by the ultrasonic attenuation while the spatial resolution depends on both the optical setup and the ultrasound transducer used. The spatial resolution of photoacoustic imaging is scaleable with the detected ultrasonic bandwidth. Photoacoustic signals with 1 MHz bandwidth is able to provide approximately 1 mm spatial resolution [52]. If the bandwidth is increased to 10 MHz, approximately 0.1 mm resolution can be achieved, with the cost of ultrasonic penetration. A 50 MHz, ultrasound transducer provides 15 micron axial and 45 microns lateral resolution with approximately 3 mm imaging depth [3]. The lateral resolution can be further improved by tightly focusing the laser beam, termed optical-resolution photoacoustic microscope (OR-PAM). More details on AR-PAM will be given in Chapter 4.

2.7 Optical Manipulation

Modifying light beam is not only helping us observe, but also able to exert small and accurate forces on microscopic target. Optical trapping is one of the most important precise micro-object control methods, along with other methods such as acoustic, magnetic manipulation, dielectrophoresis and microfluidics.

Photons carry momentum in the form of linear momentum and angular momentum. When a light beam encounters an object, it exerts pressure onto the object when the photons are absorbed and/or scattered by the object. When the momentum of the light beam changes because of absorption, reflection or refraction by an object, from Newton's second law we know that, momentum transfer happens, and force is applied to that object.

If photons are reflected back from the target surface, it will result in a pushing force, described as radiation pressure. This was first predicted by Johannes Kepler in the 17th century when he noticed the tails of comets always points away from the sun. This concept was considered by James Clerk Maxwell in his description of electromagnetic radiation in the 19th century [53]. Radiation pressure was first demonstrated by P. N. Lebedev in 1901 remarkably with only an arc lamp [54]. Nowadays, use of radiation pressure is usually associated with the laser because of its high coherence, so that the power from the beam can be tightly focused to a high intensity spot.

There is another type of force which is also caused by momentum transfer from light, but the direction of the pressure is associated with the intensity distribution of the light beam, called gradient force. Gradient force is employed to trap and move particle (by moving the laser beam) since Ashkin et al from AT&T Bell laboratory developed optical tweezers setup in 1986 [55]. When a laser beam, typical profile of which is Gaussian beam with the maximum intensity in the middle, illuminates a transparent particle with refractive index larger than the surrounding medium, light is refracted and leaves the particle with a

different direction. Because of the intensity gradient in Gaussian beam, the combined force is towards the intensity maxima, which is the centre of the beam. If the beam is highly focused with intensity maxima at focal point, the force would drag the particle to the centre of the beam near the focal point, at where the gradient pressure and radiation pressure are balanced, as shown in Figure 2-15.

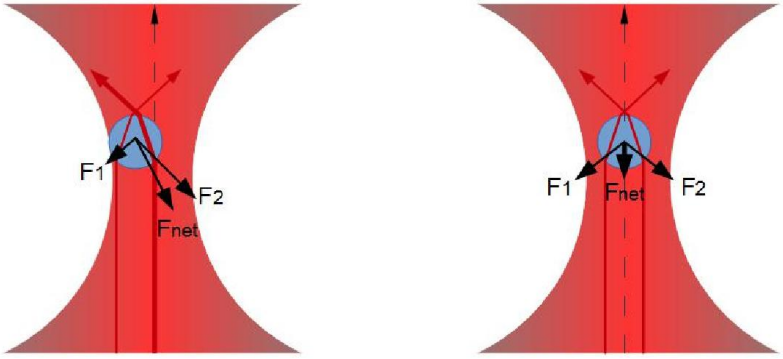

Figure 2-15 Graph of optical tweezing

To provide enough gradient, trapping is usually achieved with high NA microscope objectives (NA>1). Optical tweezers is capable of capturing and moving dielectric objects and biological cells, size ranges from tens of nanometres to hundreds of microns, provides force ranges from femtonewtons to nanonewtons [17]. Early optical traps were designed for particles much smaller than the wavelength of light, called Rayleigh particles, then it was applied to particles with size much larger than the wavelength of incident light, called Mie particles. It is also verified that the criteria for stability is satisfied for both Rayleigh and Mie particles [55].

Photons can carry angular momentum which involves polarization and wavefront of beam, named spin angular momentum and orbital angular momentum, respectively. Orbital angular momentum is the result of the vortex wavefront of light which can be found in special types of light beams, notably LG modes. Gaussian beams with planar wavefront can be tailored to vortex

wavefront to possess orbital angular momentum with special optics, like spiral phase plate (SPP) [14] or spatial light modulator with Pitch-Fork Hologram [56], [57]. Tailored beams with angular momentum were used with optical tweezers to rotate particles [17], [58].

Apart from rotation, tailored beam enables the creation of two- and even three-dimensional arrays of optical traps. Currently, the most powerful approach of multiple traps involves using of diffractive optical elements to create holographic optical tweezers [59]. Liquid-crystal SLM is one way of creating dynamic holographic optical tweezers by modulating the phase of incoming beam. For example, with holographic optical tweezing, David Grier's group has generated nearly 2000 traps in a plane and 400 traps in a 3D [60].

2.8 Acoustic Manipulation

Particles within an acoustic field also experience force because acoustic beams can carry momentum [61], [62]: linear momentum and orbital angular momentum. Unlike light beams, acoustic beams cannot carry spin angular momentum because they are longitudinal wave that has no transverse polarization. Acoustic radiation pressure was first described by A. Kundt and O. Lehman [63] in the 19th century, and then it was investigated by J. Rayleigh [64]. When an acoustic wave propagates in a fluid, sound energy propagates along the wave. If the sound energy density continuity is interrupted by an object, acoustic radiation force, similar to optical radiation force, is generated due to the reflection or absorbance of the acoustic wave by the surface of the target.

Acoustic force has been used in several ways to manipulate particles and usually works in ultrasonic range [65]–[67]. Compare to optical control, ultrasound manipulation has several advantages:

1. Wavelength of sound wave is much bigger than optical wave. Even the wavelength of MHz ultrasound is in tens to hundreds of microns range. Hence acoustic wave is more suitable for working with larger objects.

2. Radiation pressure is proportional to beam power divided by the wave speed. Sound wave is capable of delivering much larger power than light beam. Moreover, speed of sound in water is less than 1/200,000 of light speed in water. That means, achievable radiation force by acoustic beam is way larger than that of light beam. For instance, suspending heavy target like tungsten particles in the air has been demonstrated [68], [69] with standing sound wave.

3. Particles in acoustic standing waves are usually trapped in the pressure nodal planes which has plenty room for large amount of suspended particles, comparing to focusing point(s) in optical tweezers only for a limited number of targets.

4. Compared to optical tweezers, which requires laser and expensive optics components, the cost of acoustic device is much cheaper for volume production in future industry applications.

Table 2-1 comparison of optical and ultrasonic trapping

	Optical trapping	*Ultrasonic trapping*
Wavelength	Short (~ 1 μm)	Long (μm ~ mm)
Target size	Small (nm ~ μm)	Large (μm ~ cm)
Force	Small (pN)	Large (nN)
Working distance	Short (~10 μm)	Long (μm~ cm)
Target quantity	Few	Large quantity
Force and position precision	Good	Poor
Cost	Expensive	Cheap

Table 2-1 shows the general comparison of optical and ultrasonic trapping,

Recent research mainly focuses on using ultrasonic standing wave (USW) because it is able to generate larger trapping force [70], [71]. In a USW, particles in the acoustic field moves toward either the node or the antinode of the standing wave (pressure nodal planes), depending on properties of the particles, such as

compressibility and 'the relative density factor' which is the ratio of the particle and fluid densities [72], [73]. This has been widely used to aggregate or separate particles and biological cells [70], [71], [74]. However, the creation of standing waves relies on reflection. This restricts the working range of standing wave to be several wavelengths. In addition, the creation of standing wave requires the distance between active element and the reflector matches the wavelength of acoustic beam. This makes moving of the pressure node hard to implement.

Rather than just making use of acoustic waves with planar wavefronts in USW, transferring angular momentum of acoustic beam for rotation is also under research [75]–[78], similar to the situation in optical manipulation. Due to the difficulty of creating desired acoustic beam, access to advanced acoustic phase array is essential to flexible and dynamic manipulation.

2.9 Conservative Force vs. Non-conservative Force in Trapping

In optical tweezers, trapping is limited by competition between the gradient force acting to trap particles, and the radiation force acting to push particles out of the trap in the direction of propagation of the trapping beam.

The difference between gradient force and radiation force is fundamental. Gradient force is pointing to the point with potential energy minima thus it is conservative force, while pure radiation force does not need potential gradient it is a kind of non-conservative force.

The distinction between conservative and non-conservative forces can be traced back to the fundamental difference between those two kinds of force: if there is need to create potential well. For those involves conservative force, moving of the trapping objects would involve mechanically moving the potential well, while in contrast, it is not needed for the trapping with non-conservative force.

Some of the earliest experimental examples of remote manipulation with optical and acoustic fields took the form of levitation traps [79], [80]. The radiation force used in those demonstrations are from a beam used to push a target away from the source and balance against gravity, hence are positive and non-conservative pressure. The direction of those positive radiation forces is the same as the propagation direction of the beam, which results from either backscattering or absorption of the forward-direction momentum.

In contrast, most current optical and acoustic tweezing system [17], [55], [81] are examples of conservative gradient force in which particles are drawn towards potential energy minima, transforming the potential energy to kinetic energy. Time-evolving potential energy wells such as rotating anisotropic traps [82], or optical conveyors [83], [84] that continuously sweep potential energy minima to move trapped particles, are also examples of conservative force. Another example of conservative force is the force in standing wave acoustic trapping towards the potential minima.

Even though manipulation involving conservative force is able to provide accurate position targeting, using only non-conservative forces can offer exclusive benefits. It eliminates the need for a highly focused region in optical trapping or the necessary of creation of standing wave in ultrasonic trapping. Hence, the manipulation range can be extended significantly. Furthermore, without the limitation by the potential well, the manipulate-able target size can be extended to a much larger scale.

Chapter 3
Light-Sheet Tomography (LST) for *in situ* Imaging of Plant Root

When light scattering and absorption in the sample is not strong, scattered light from the sample is a good source for optical imaging with relatively high resolution, comparing to ultrasound.

In this chapter, a microscope system with light-sheet illumination will be demonstrated to image plant roots with scattered light. Imaging of plant roots can also be done with ultrasound imaging, but low resolution of ultrasound imaging is not enough for observing the micro-structure in the sample. Comparing to lately developed fluorescence imaging, scattering imaging still benefits from the vast varieties of samples and without the need to worry about complicated sample staining. In addition, equipment requirement is much lower than that of fluorescence setups.

3.1 Light-sheet Sectioning

3.1.1 Light-sheet Imaging Technology

As introduced in Chapter 2.4.2, light-sheet microscopes use a thin sheet of light to illuminate the target and an optical detector perpendicular to the illumination plane to take the image. The idea of light sheet was firstly

introduced in 1902 as the principle of *ultramicroscope* [39]. It was named 'ultra'-microscope because it is capable of detecting objects smaller than resolution limit, i.e. around 500 nanometres. It uses light from sun or a white lamp passing through a thin slit to form the light sheet, then illuminates onto scattering sample with sub-diffraction size. Based on scattering instead of reflection, this method allows the observation of particles with the size smaller than diffraction limit. The inventor of ultramicroscope Richard Adolf Zsigmondy was rewarded Nobel Prize in 1925 for his research of ultramicroscope.

Afterwards, there is not much improvement on the setup due to the technology limitation until the late 20th century. The development of modern microscopy is only possible with evolution in other areas, including: (1) the invention of the laser (originally as an acronym for Light Amplification by Stimulated Emission of Radiation) around 1960s [85], providing high power, coherent illumination, (2) the wide use of fluorescent dyes, especially the discovery of green fluorescence protein (GFP) in 1990s [86] which enabled marking special structure in specimen and improvement of resolution; (3) development of modern cameras and computers, etc.

With the help of modern technology, the light-sheet method was extended to Light-Sheet Fluorescence Microscopy (LSFM) which is having an ever increasing impact in biology research. There have been several different names of LSFM along the development of the technology. The first paper about fluorescence-label involved light-sheet microscope was published in 1993 by Voie et al, with the name of Orthogonal-Plane Fluorescence Optical Sectioning microscope (OPFOS) [87], for imaging structure of the cochlea. Resolution achieved by OPFOS was 10 μm laterally and 26 μm axially with samples of size in the millimetre range.

Although Voie has published several papers [87]–[89] about OPFOS, the research on LSFM was not noticeable until the publication of another paper in Science in 2004 [47] from European Molecular Biology Laboratory (EMBL) which

leads the research of LSFM development, with another name: Selective Plane Illumination Microscopy (SPIM, or Selective Plane Illumination Microscopy). SPIM was used to image GFP-labeled transgenic embryos of the teleost fish Medaka (Oryzias latipes) *in vivo* based on their confocal theta microscope [90], [91].

Confocal theta microscopy was first invented to improve axial resolution of confocal microscope by illuminating and imaging the sample at different angles to each other (best results when perpendicular). Like confocal microscopy, microscope objectives are used for illumination and imaging. The intersection of the PSFs (point spread function, uses to describe the response of an imaging system to a point object), from the illumination objective and imaging objective respectively, results in a smaller sample volume, thus improves the spatial resolution.

SPIM provided superior penetration depth, compared to confocal LSM, with high resolution (6 μm) at the depth of 500 μm inside the fish embryo, which cannot be achieved by confocal microscopy at this depth. Furthermore, benefiting from the low photo blenching of light-sheet technology, imaging stacks of the developing of the embryo was taken every 5 minutes over a period of 17 hours and the embryo completed embryogenesis normally without being affected. This proved that SPIM is suitable for long-term monitoring of sample development.

During the development of light-sheet microscopy, a number of other LSFMs were developed with different aspects. It is interesting to notice that each team has developed a different system would give it a different name and acronym (as shown in Table 3-1).

In 2002, Fuchs et al demonstrated a setup similar to OPFTS with a name of Thin Laser Light-Sheet Microscope (TLSM) to image microorganism in seawater [92].

In order to image large samples like intact mouse brain, dual-side illumination with light sheet was introduced to make the illumination more

uniform across the whole sample [93], which was named ultramicroscope again. In the same year, Huisken and Stainier from EMBL improved SPIM setup with dual-side illumination sequentially and pivoting light sheet to reduce stripes and shading [94] caused by blocking of illumination light. Apart from eliminating stripes and shading, the benefit of dual-side illumination is two-fold. Firstly, illumination on two sides can ensure the quality of the light sheet on both sides. Secondly, at each time, only half of the sample needs to be illuminated, which means the field of view (FOV) is halved. As a result, a thinner light sheet can be used for halved FOV, which improves optical sectioning and axial resolution. In the early setups like SPIM, only a cylindrical lens is used to form the light sheet. However, cylindrical lens can introduce aberration, comparing to well-calibrated optics like objectives. Thus in improved setups like mSPIM, objectives are used together with the cylindrical lens to create diffraction-limit light sheet, thus leads to better axial resolution.

A major problem of light-sheet microscopy is the spread out of the light sheet along the sample. The light sheet focused by a cylindrical lens with/without objective has a minimum thickness at beam waist, similar to when the beam is focused to a point, then the beam thickness increases on both sides of beam waist. The thickness at beam waist and the increasing speed of its speed is associated with the numerical aperture (NA) of the incoming light: the thinner the beam waist, the faster the thickness increases. To maintain the uniform illumination, the thickness of light sheet should be well maintained along the FOV [95]. Buytaert and Dirckx [96] tried to solve this problem by scanning the sample (middle ear specimen) along the illumination plane and then stitching images to form a well-focused image across the whole specimen. They named their setup high-resolution OPFOS (HROPFOS). With HROPFOS, in−plane resolution of 1 μm and slicing resolution of 2 μm were achieve. It was a big improvement comparing to the best axial resolution of 14 μm before.

Table 3-1 Table of variety of light sheet devices

Name and Acronym	*Year*	*Light Source*	*Light Sheet*	*Illumi-nation*	*Unique Feature*	*Advantage*	*Specimen Size*	*Authors*	*Refer-ence*
Ultramicroscopy	1903	Sunlight or lamp	Slit aperture	Single	Based on light scattering	detect object smaller than diffraction limit	Gold Beads ~500nm	R. Zsigmondy	[39]
Orthogonal-plane fluorescence optical sectioning microscopy (OPFOS)	1993	532 nm laser	Cylindrical lens	Single	Light sheet illumination	Optical sectioning	Cochlea >1 cm	A. VOIE	[87]
Theta confocal microscopy	1995	450, 550 nm laser	Pinhole	Single	Use pinhole to reduce illumination area	Photo-blenching reduced	<1 cm	S. Lindek & E. Stelzer	[91]
Thin light sheet microscopy (TLSM)	2002	540 nm laser	Cylindrical lens	Single	Light sheet illumination from the side	Improved contrast	microorganism in seawater >1 cm	E. Fuchs	[97]
Selective (Single) plane light sheet microscopy (SPIM)	2004	488 nm laser	Cylindrical lens	Single	sample rotation	Fast acquisition, good penetration	medaka embryo <1 cm	J. Huisken & E. Stelzer	[47]
Multidirection SPIM (mSPIM)	2007	489 nm laser	Pivoting cylindrical lens + objective	Dual	Pivoting light sheet, dual-side illumination	Reduced stripes and shading, increased resolution	zebrafish embryo <1 cm	J. Huisken	[94]
High-resolution OPFOS (HROPFOS)	2007	532 nm laser	Cylindrical lens	Single	Light sheet translated followed with image stitching	Constant thickness of light sheet	middle ear specimen >1 cm	J. Buytaert	[96]
Ultramicroscopy	2007	488 nm laser	Cylindrical lens	Dual	Dual-side illumination	Sealed chamber with clearing solution	Mouse brain >1 cm	H. Dodt	[93]
Oblique plane microscopy (OPM)	2008	532 nm laser	Cylindrical lens	Single	Tilted image plane	Extended FOV	<1 cm	C. Dunsby	[98]
Digital scanned laser light sheet fluorescence microscopy (DSLM)	2008	400~650 nm laser	f-theta lens	Dual	light sheet generated by beam scanning	Uniform light sheet, potential for structural illumination	zebrafish embryo <1 cm	P. Keller & E. Stelzer	[99]
Highly inclined and laminated optical sheet microscopy (HILO)	2010	491 nm laser	Scanned line	Single	Single lens for illumination and detection	Single lens	>1 cm	J. Mertz	[100]
DSLM with incoherent structured-illumination (DSLM-SI)	2011	400~650 nm laser	f-theta lens	Single	Structured illumination	improved imaging quality (contrast) and high imaging speed	Medaka fish embryo <1 cm	P. Keller & E. Stelzer	[50]
Two-photon SPIM (2P-SPIM)	2011	448 nm	objectives	Dual	2-photon illumination	improved signal rate and more isotropic resolution	fly embryo <1 cm	T. Truong & S. Fraser	[101]
Simultaneous Multiview light sheet microscopy (SiMView)	2012	491, 532, 561, 594nm laser	objectives	Dual	4 optical arms	faster imaging speed and optimized for bigger sample	fly embryo <1 cm	P. Keller	[102]
Multiview SPIM(MuVi-SPIM)	2012	405~685 nm laser	objectives	Dual	4 optical arms, simultaneous multiview	faster imaging speed with long period time imaging	fly embryo <1 cm	L. Hufnagel	[103]
Lightsheet Z.1	2012	405~635nm	objectives	Dual	Commercial product	Compact product, simplified control and image processing	<1 μm ~ 4 mm	Zeiss	[104]

In another device named objective-coupled planar illumination (OCPI) microscopy, the illuminator and the observing objective were attached together [105], [106]. This device was used to study the pheromone-sensing neurons of the mouse vomeronasal organ.

Dunsby [98] developed oblique plane microscopy (OPM) which used a single, high NA objective to both illuminate and collect the fluorescence with an oblique light sheet.

Mertz and Kim [100] described a HiLo light-sheet microscope which uses structured illumination to eliminate out-of-focus signal to improve image quality.

A big evolution of LSFM happened in 2008 with the invention of digital scanned laser light-sheet fluorescence microscopy (DSLM) [34], [99], [107] from EMBL. In DSLM, instead of using cylindrical lens to form the light sheet, the incoming laser is focused with f-theta scan lens to a line and scanned at image plane to form the light sheet. This scanning process significantly improved the quality of illumination. F-theta lens is designed to provide a flat field, instead of a circular plane by a spherical lens, at the image plane of the scanning system. Similar effect can be achieved by a well-calibrated objective lens, hence later light-sheet microscope designs opted for objective lenses. The beam scanning frequency is much higher than frame rate, hence the illumination is even for the exposure time of each image. Compare to conventional SPIM setup, DSLM has several advantages: (1) With better calibrated optics components, beam quality of DSLM is greatly improved. (2) DSLM can provide uniform illumination to each line in the specimen, which is important to quantitative imaging of large specimen. (3) All the illumination energy is focused to a single line, which provides much higher illumination efficiency of 95%, as compared with 3% in standard SPIM. (4) DSLM allowed the potential of introducing structured illumination, which can significantly improve the contrast and resolution, especially in large scattering samples. DSLM was used to record nuclei

localization and movement in a zebrafish embryo over 24 hours of development [34].

To address the image quality and contrast decreasing caused by specimen scattering, selective plane illumination microscopy with structured illumination (SPIM-SI) [108] was invented by placing a mechanical ruling in conjugate image plane in the illumination arm in SPIM. This approach was improved with the introduction of DSLM-SI (DSLM-structured illumination) in 2010 [50]. In DSLM-SI, the illumination-laser-beam intensity is modulated electronically by an acousto-optical tunable filter (AOTF) in a sinusoidal way to provide structured illumination patterns. Long-term imaging of zebrafish development for 58 hours and multi-view of early Drosophila melanogaster development was performed with DSLM-SI.

Truong et al [101] integrated two-photon imaging method and DSLM together, and invented two-photon scanned light-sheet microscopy to image fly embryo. They named it 2P-SPIM even though they were using the DSLM setup. Although 2P-SPIM cannot provide equivalent signal rate (fluorescence signal output per input laser power) as DSLM, it still has 100-fold higher signal rate than cylindrically focused setup like SPIM [109], and it can achieve similar signal rate as 2P-LSM (two-photon laser scanning microscopy) with only 1/10 of illumination NA. Moreover, 2P-SPIM can provide larger sample depth to SPIM due to two reasons: 1, Near-infrared excitation light used in 2P ensured less scattering of illumination; 2, Thickness increment deep in sample caused by scattering is less important because 2P excitation only happens at the highest intensity part of the beam. Those features provide higher imaging depth with more isotropic resolution.

By combining the features of Bessel beam illumination, structured illumination, plane illumination and two-photon illumination, Planchon et al [18] extended the edge of DSLM performance and achieved 3D isotropic resolution down to ~0.3 μm with imaging speed of 200 image plane per second.

It is worth noticing that two papers got published on *Nature* on the same issue in July 2012 introducing multiview method of light-sheet microscopy. Called SiMView (simultaneous multiview) by Tomer et al [102] from Howard Hughes Medical Institute USA and MuVi-SPIM (Multiview SPIM) by Krzic et al [103] from EMBL Germany, the 4-optical-arm light-sheet microscopes eliminates the need to rotate the sample, thus suitable for high-speed imaging. Temporal resolution achieved by SiMView is 30s with 450 frames of 10MB data.

Ahrens et al [110] in EMBL extended the capability of SiMView at imaging speed approximately tenfold for imaging neurons in zebrafish. More than 80% of all neuron in the whole brain were monitored at 0.8 Hz. This speed improvement was done by: (1) Laser scanning in two directions and movement of the detection objective, thus eliminating the need for sample movement. (2) Replacement of sCMOS camera and CameraLink frame grabbers with faster hardware. The complementary performance improvements result in 0.8 Hz recording speed of 800 * 600 * 200um^3 with 20X magnification, therefore capable of revealing functionally defined circuits across the whole zebrafish brain.

Not long after the first SPIM paper published [47], company Carl Zeiss and EMBL commercially announced producing products based on LSFM in 2005. However the imaging result of SPIM then was still suffering from drawbacks, uneven illumination, stripes on image and slow imaging speed, for instance. While light-sheet technology is becoming more and more advanced, the first commercial light-sheet product came out in 2013 from Carl Zeiss with the name of Lightsheet Z. 1 [104]. Lightsheet Z.1 combines many features in LSFM, such as scanning light sheet, rotating sample holder, dual and pivot illumination, and sCMOS cameras, etc. It is capable of imaging samples of various sizes, from < 1 μm to 4mm, and is 3D sample friendly because there is no need to use cover slip. Lightsheet Z. 1 offers biologists an easy approach to take advantage of the latest technology without the hassle of optics background however, with an expensive price tag (approximate £200,000-£250,000).

For a simpler and cheaper solution, website OpenSPIM.org [111] delivered by The Max Planck Institute of Molecular Cell Biology and Genetics (MPI-CBG) provides all the information to build a single-illumination or dual-illumination SPIM setup, from hardware to software and even imaging processing methods. OpenSPIM is a more flexible solution but requires more background knowledge in optics. Comparing to Lightsheet Z.1, the achievable resolution from OpenSPIM is not as promising; however, it has many applications where the requirement for resolution is not as high. Moreover, low cost of OpenSPIM means 10s of devices can be built for large-sample-quantity applications.

A challenge when working with LSFM is processing the tremendous amount of data produced. For instance, a full frame produced by latest sCMOS camera is 11 MB or 16 MB, depending on the dynamic range chosen. For a large specimen which requires 100 Z-stacks or more, such as fly embryos [101], a single 3D image would results in more than 1 GB of data. Fast development of embryos demands for good temporal resolution. Imaging the whole embryos every minute for 10 hours will produce more than 600GB data. Sequentially dual-illumination or multi-view can even double or 4-fold the amount and results in as much as 4TB data [102] in only 6 hours. Large amount of data processing is requiring for both faster hardware and software development.

3.1.2 Samples

As we can see, due to its light-sectioning feature, light-sheet microscopes are more suitable for imaging 3D, large, transparent samples, such as cochlea [87]–[89], mouse brain [93], medaka embryo [47], [50], zebrafish embryo [34], [94], [99], fly embryo [101]–[103], etc.

Furthermore, it is also suitable for long-term monitoring the development of samples due to its low photo damaging and photo-toxicity brought to specimen, as well as low photo bleaching to fluorophore [34], [47], [50], [94], [101], [102].

3.1.3 Why Imaging Plant Root?

The agriculture revolution in the mid-20th century greatly increased the productivity of crops around the world. However after half a century, with dramatically increased population growth, agriculture is now facing even more challenges than before. This includes the reducing application of fertiliser due to its harmful effect to the environment [112]. In addition, climate change and reduction of usable farmland are bringing more challenges to agro industries. Improving of crop production is crucial to human living condition.

Plant nutrient use efficiency (NUE) is defined as fresh weight or product yield per content of nutrient. The root of plants is playing the role for the plant's take of resources from the soil [113] and plant's NUE is influenced by numerous root properties such as the architecture of the root system [114]. Thus manipulation of root phenotype to improve NUE and therefore production has great potential to improve the production of agriculture. To engineer more efficient root systems we need better understanding of root mechanisms. In other words, we need to be able to monitor the growth condition of plant roots. However, existing methods suffer from limitations [115], for instance: manual sampling of roots is slow, destructive and inaccurate; increasingly popular used X-ray micro-tomography is expensive and lacking in throughput.

Fortunately, the newly development transparent soils [116] has provided a possibility to take the advantage of light-sheet microscopy for imaging plant roots *in situ* with a straight forward and low cost solution.

3.1.4 Light-sheet Tomography

We have developed a new form of non-fluorescent light-sheet imaging which we demonstrate here. This method uses the elastic scattering of light from a sample when illuminated by a light sheet. The scattering is imaged orthogonally to the light sheet such that only scattered light arrives at the camera.

The use of scattering rather than fluorescence as a contrast mechanism, as in LSFM [117], makes this imaging technique similar to diffuse optical tomography but, as we use it here exclusively with samples containing a low volume density of scatterers, 3D images can be built up directly from the optical sections taken by scanning the sample through the light sheet.

We term this technique Light-sheet Tomography (LST). As an example of the utility of LST we show imaging of various fibrous structures such as paper and high density foam, both of which contain complex 3D surfaces. The method is particularly well suited to imaging roots and taking advantage of the low scattering of recently developed transparent soil [116] and low density of root structures. We demonstrate the application of LST to imaging roots live and *in situ* and show that the resolution obtained is sufficient to observe microscopic root traits such as root hairs. Avoiding the need for fluorescence also means plants can be rapidly phenotyped without the need for further genetic manipulation to introduce fluorescent proteins or the need for staining.

As introduced before, the axial resolution of a light-sheet microscope is associated with the thickness of the light sheet, which is defined by the properties of the incoming light rather than the numerical aperture of the imaging objective, thus the axial resolution is independent to the imaging objective. Therefore good axial resolution can be obtained with low cost and low magnification objectives [47], [118], [119]; this also benefits us with larger field of view. LST only illuminates the volume of the sample which is being imaged, with out-of-focus structures left "in the dark". As a result the light dose experienced by the root is kept to a minimum, both in terms of the duration of the illumination and the total amount of light experienced, and the background signal is kept to a minimum. This low light dose is vital as too much light could potentially affect the growth of the roots, changing their behaviour and reducing the validity of any measurements. This gives LST a strong advantage over other imaging techniques such as confocal microscopy where the whole sample is illuminated regardless

of how much of the sample is in focus [43], [120]. Hence, long time monitoring of plant root growth can be obtained using LST. In addition, since LST can obtain a B-scan in a single exposure, the imaging speed is improved when compared with confocal microscopy, laser scanning microscopies or computed tomography approaches which require 3D reconstruction [121]. These advantages make LST an ideal tool for taking images of living plants in a low cost high-throughput setup.

3.2 Materials and Methods

3.2.1 Light-sheet Setup

A low-cost light-sheet tomography system was built, as shown in Figure 3-1. The major advantage of this system is that it is cheap and easy to operate, thus suitable for biologists to use. Standard optical elements were used and the total cost of the setup is less than £1500 excluding the PC, software, laser and the camera.

To achieve low cost and easy alignment, only essential components in LSFM are used without compromising the advantages of light-sheet method. A frequency-doubled solid-state laser (FCD488-020, JDSU, USA, wavelength 488nm, continues wave, maximum power 20mW) is used as the illumination source with 488 nm wavelength allowing future co-registration of LST and LSFM images in a single device. The output power of the laser is controlled by introducing a set of neutral density filters (NEK01, Absorptive ND Filter Kit, Thorlabs). The diameter of the laser output is 0.7 mm and a telescope consisting of two plano-convex lenses [focal length (FL) = 50 mm & FL = 500 mm, Thorlabs, UK] is used to form a beam expander with enlarge factor = 10 to increase the diameter of the beam to 7 mm. The central element of this setup is the cylindrical lens (LJ1567L1-A, FL = 100 mm, AR-coated: 350-700 nm, Thorlabs). Introducing another well-calibrated objective after the cylindrical lens to illuminate the

specimen will increase the quality of the light beam [94], but it will increase the cost of this setup. Moreover, using objective for illumination will also shorten the working distance, which is not idea for big samples like plant roots. Testing of the light sheet thickness was carried out in Chapter Calibration3.3.1. An adjustable mechanical slit (VA100, 0~6 mm, Thorlabs) is used before the cylindrical lens to change the diameter of the incoming beam, hence adjusting the effective NA of the illumination and adjusting the thickness of the light sheet itself. The imaging path consists of an objective (4×/0.1 or 10×/0.25, infinity corrected, Olympus, UK), a tube lens (U-TLU-1-2, FL = 180 mm, Olympus) and a camera [EC1280, (1280 × 1024) pixel resolution, 6.7 μm per pixel, PROSILICA, Canada; or Neo, (2560 × 2160) pixel resolution, 6.5 μm per pixel, Andor, UK].

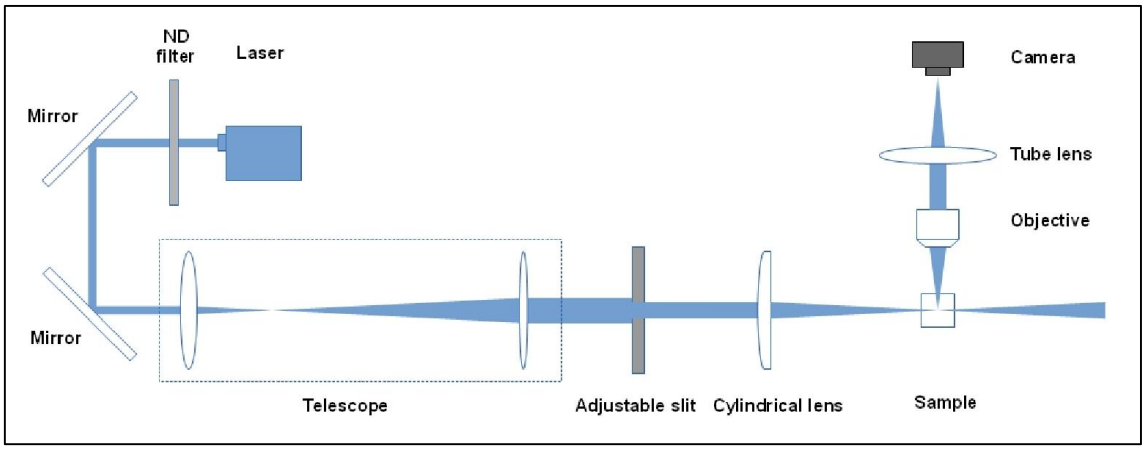

Figure 3-1 Setup of the LST (top view). A 488 nm wavelength solid-state laser is used as the illumination source. The output power of the laser is controlled with ND filters. Beam is expanded with a 10 time beam expander. An adjustable mechanical slit is used before the cylindrical lens to change the diameter of the incoming beam and adjusting the effective NA of the illumination and adjusting the thickness of the light sheet itself. The imaging path consists of an objective, a tube lens and a camera.

With a 10X objective, the field of view of this setup is 858 μm × 686 μm, which can be increased by using a lower magnification objective. Recording the data of each sample was performed while moving the sample along the observation axis, manually or automatically. For each sample, more than 100

frames were taken to build a 3D image, which gave an increment between stacks of approximately 8 μm.

For later automatic monitoring of lettuce root development, the setup was improved to suit the situation. It was achieved by introducing high resolution motorized translation stages (M111.12S, PI, Germany) and high quantum efficiency sCMOS Neo camera (16.6 x 14mm sensor size) into the system. A 4X objective (NA 0.1, Olympus) was used to provide a larger field of view. With the sCMOS chip on Neo camera (16.6 x 14.0 mm), the FOV is 4.15 x 3.5 mm. This could be further increased by programming the PI stages to allow multi-position recording. The NA of incoming light was adjusted to 0.009 to provide an appropriate Rayleigh range with 35 μm waist thickness. An optical chamber is used to minimized the aberration while sample moving due to refractive index change.

3.2.2 Light Sheet Geometry

As introduced in Chapter 2.1.1, Gaussian beam has a smallest ω_0 at beam waist. Gaussian beam either diverges from or converges to this beam waist. The beam waist diameter of a TEM_{00} mode beam depends on the beam divergence angle as:

$$d_0 = 2\omega_0 = \frac{4\lambda}{\pi\Theta_{div}} = \frac{4\lambda f}{\pi D} \qquad \text{Eq. (3-1)}$$

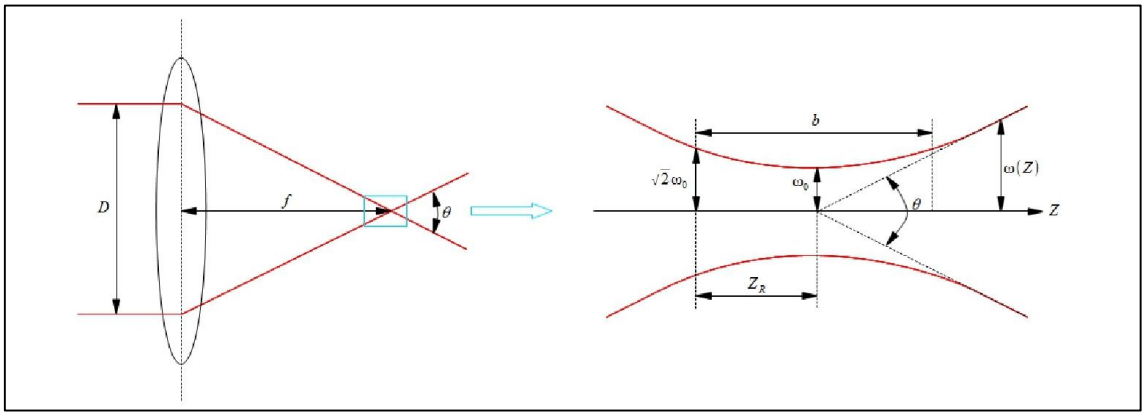

Figure 3-2 Gaussian beam waist diagram

In light-sheet setups, instead of focusing the beam down to a spot, the cylindrical lens focuses the beam at one direction to a light sheet. Similarly, the thickness of the light sheet gets to minimum at the focal line of the cylindrical lens. Similar to the beam waist, the minimum thickness of the light sheet depends on the beam divergence, i.e. numerical aperture of the incoming light, which is proportional to the width of the laser beam diameter D [gbur2001rayleigh]:

$$d_0 = 2\omega_0 = \frac{4\lambda f}{\pi D} = \frac{2\lambda}{\pi * NA} \qquad \text{Eq. (3-2)}$$

The Rayleigh range of the beam is defined as: at a distance from the waist equal to z_R , the diameter of beam spot is $\sqrt{2}$ the diameter at beam waist, i.e. $\sqrt{2}d_0$.

$$z_R = \frac{\pi\omega_0^2}{\lambda} = \frac{\lambda}{\pi * NA^2} = \left(\frac{4\lambda}{\pi}\right)\left(\frac{f}{D}\right)^2 \qquad \text{Eq. (3-3)}$$

To get an image with uniform axial depth, the Rayleigh range of light sheet should be larger than the imaged area, i.e. FOV [118]. From the equation above we can see that Rayleigh range is also associated with the width of incoming beam and focal length of cylindrical lens. The width of the incoming laser beam was set by the adjustable slit to be 4 mm. This makes the theoretical thickness to be 15.5 μm in the ideal case (with the focal length of the cylindrical lens 100 mm) with 780 μm Rayleigh range for EC1280 camera with 10X objective. The thickness can be decreased by simply changing to a short-focal-length cylindrical lens or increasing the width of the incoming beam, though this will lead to a shorter Rayleigh range and a spreading of the light sheet across the sample.

3.2.3 Sample Orientation

Before imaging of plant roots was performed the performance of the LST system was assessed using two test materials with complex structures: lens cleaning tissue and dense foam. Since the samples are not transparent, to obtain the image, we set the (flat) samples at 45° to the illumination plane and the observing axis as shown in Figure 3-3, hence ensuring optical sectioning of the

sample with an illumination depth of $\sqrt{2}$ times the thickness of the light sheet as observed by the camera.

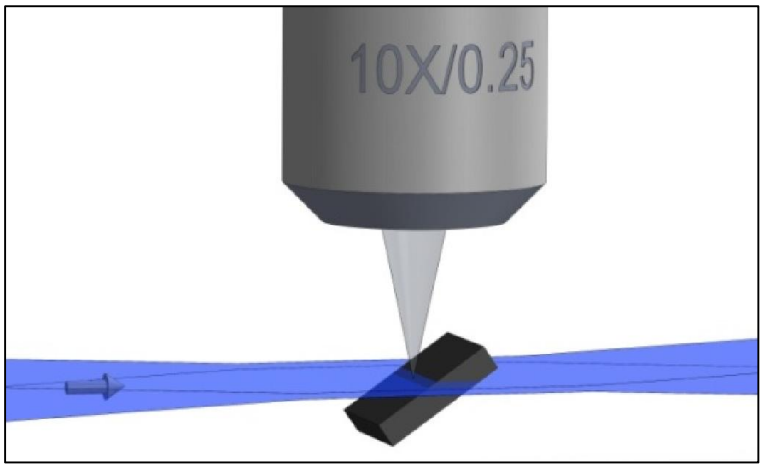

Figure 3-3 Orientation of the sample

All the images were taken with a 10× objective. 3D datasets were constructed by recording a video while moving the sample towards the objective at 10 μm/s. A 3D image of the sample was reconstructed by using the ImageJ plugin "3D viewer".

3.2.4 Optical Chamber to Eliminate Light Path Difference

For arabidopsis samples, because the diameter of plant root is small (~100 μm), light path distance change due to refractive index mismatch caused by sample moving is negligible. However when once comes across larger lettuce with approximately 1 mm root, the light path difference is enough to cause out of focus from the objective. Water immersed objectives were used in LSFM setups [47], [94], [118], [119] to eliminate the effect.

In LST, an air objective along with an optical cell filled with water was used to minimize this effect. Since the resolution is not as important as in LSFM setup, this arrangement is sufficient.

3.2.5 Transparent Soil Preparation

Before getting on to plants, transparent soil made from Nafion were prepared for root growth. Nafion (Ion Power Inc., USA) in the form of 4 mm × 3 mm pellets in acid (NR50 1100) and precursor (R1 100) forms were used. Nafion particles were smashed with a freezer mill (6850, SPEX SamplePrep, UK). The final particle size range was 200– 1600 μm. Cation exchanging Nafion particles were made by ensuring full conversion to the acid form by washing in a solution of 15% v / v KOH, 35% v / v DMSO and 50% dH_2O at 80 °C for 5 hours, then with dH_2O (milliQ) at room temperature for 30 minutes followed by several dH_2O rinses. This was followed by 2 washes in 15% v / v nitric acid at room temperature: 1 wash for 1 hour and 1 wash overnight. The particles were treated with 1M sulphuric acid for 1 hour at 65 °C, and the acid was removed and replaced with dH_2O at 65 °C for 1 hour. After cooling, the particles were washed several times with dH_2O. They were then washed in a 3 wt % H_2O_2 solution at 65 °C for 1 hour and allowed to cool. The particles were rinsed again multiple times with fresh dH_2O [122]. To titrate the particles with mineral ions, concentrated (i.e. undiluted) MSR media [123] were used to immerse the particles. These were shaken at 30 °C for 30 minutes before renewing the nutrient solution. This was repeated until the pH of the nutrient solution was neutral and stable after adding it to the particles. The particles were rinsed with dH_2O to remove excess MSR media. Before use, the particles were autoclaved, submerged in dH_2O for sterilisation. This procedure can be used to recycle Nafion particles for future use.

3.2.6 Plant Culture

Arabidopsis plant in transparent soil was prepared for still imaging. Time lapse imaging of root growth was carried out with *Latuca sativa* (lettuce, var. capitata, Seed Parade, UK) roots because roots of *Latuca sativa* have higher elongation rate. Plants can grow well in transparent soil. Lettuce plants both in

Phytagel and transparent soil are studied because either media has its advantage: plants in Phytagel can provide better image quality due to uniform media while transparent soil is more similar to real soil condition for plants.

Before imaging the root, the Nafion particles need to be saturated with refractive index matched solution (20% sorbitol) to get a clear light path. This would stop plants from further growing because plants cannot get nutrition or oxygen from the solution at such high concentration. Percoll® can be used instead of sorbitol solution because Percoll® is colloid solution and therefore has limited effects on root growth.

To create a suitable living condition for the plant with clear light path, a) Phytagel with half-strength M&S basal medium and b) transparent soil saturated with Percoll® was used as base. 85% Percoll® was used for RI matching

1) Arabidopsis in transparent soil

Wild type Arabidopsis Thaliana, ecotype C24, was used. The seeds were sterilized on filter paper by ethanol washes. Seedlings were germinated in Petri dishes with MSR nutrient media [124] solidified with 6 g/L phytagel (Sigma P8169) before being transferred to transparent soil. Plants were incubated and grown at 20°C with 16 hours light: 8 hours darkness. Growth period was 1 – 2 weeks post-germination. Transparent soil [116] was used as the particulate growth substrate in glass cuvettes (four clear sides 12 mm x 12 mm x 45 mm 4.5 mL, fisher).

2) Lettuce in Phytagel

On day one of setting up the samples, *Latuca sativa* seeds were sterilized by washing in 10% bleach (Domestos, Unilever UK Ltd.) for 20 minutes followed by several sterile dH_2O washes. The seeds were sown separately in cuvettes containing 7 g/L phytagel with half-strength M&S basal medium with tip of seeds inserted into gel. This allowed the plants growing into the gel. Cuvettes were sealed with Nescofilm to conserve water and also avoid contamination. The

"under-ground" part of the cuvettes was covered with aluminium foil to create dark condition for the roots, similar to the real condition in normal soil. All the procedures above were done in a laminar flow cabinet to prevent contamination.

The cuvettes were kept in a temperature controlled room at 20 degrees with 16 hours light: 8 hours darkness each day. The plants were growing in the room for 7 days before imaging.

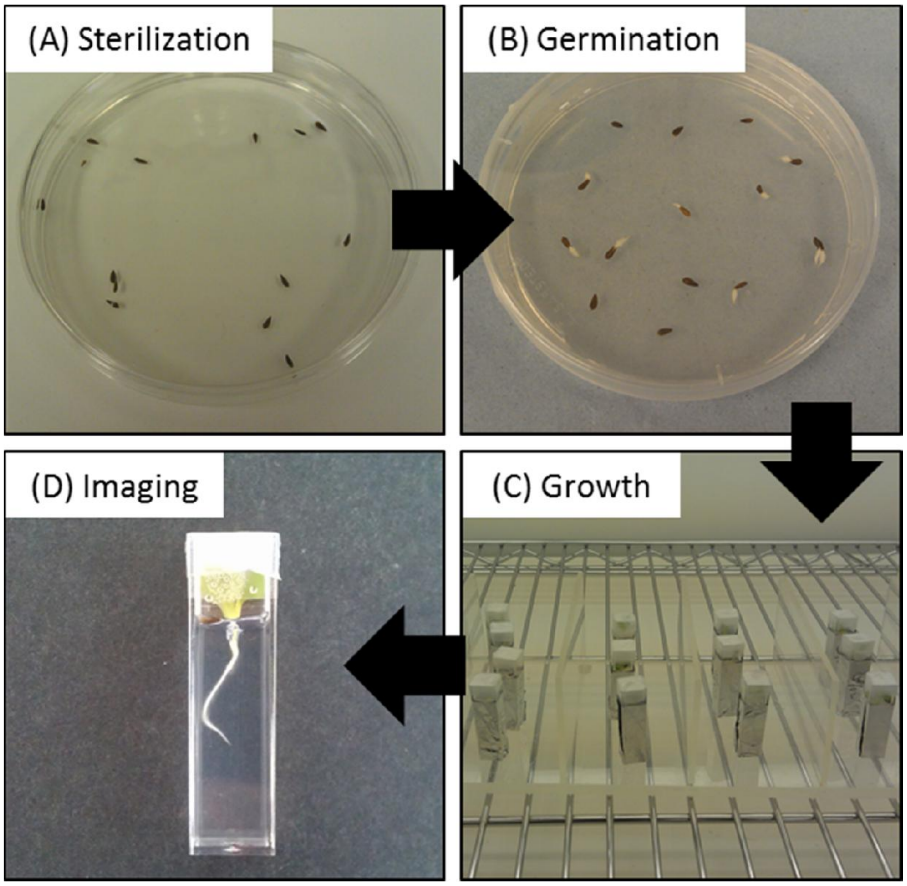

Figure 3-4 Preparing of lettuce plant. Seeds were sterilized by washing in low-concentration bleach followed by several sterile dH_2O washes (A). The seeds germinated in petri dish with suitable medium (B) and then plants were sown separately in cuvettes. Cuvettes were sealed and half-covered with aluminium foil to create dark condition for the roots (C). After several days, it is ready for imaging (D).

3) Lettuce in transparent soil

Similar procedure was followed as preparing lettuce plant in Phytagel, however the growth media was changed to Percoll® saturated Nafion particles.

Concentration of Percoll® was 70% to provide the best refractive index matching (RI=1.34).

3.3 Result and Discuss

3.3.1 Calibration

In order to investigate the resolving power of LST under ideal conditions we constructed a target consisting of micro particles set in a polyacrylamide (PAA) gel. This arrangement also allowed the thickness of the light sheet to be determined experimentally. The gel was set in a small cuvette containing 2 μm polystyrene microspheres [(1.998 ± 0.022) μm, NIST certified, Thermo, USA]. The thickness of the light sheet was measured using microsphere targets. The sample was translated along the axis of observation, and images of the microspheres were captured at intervals of 0.5 μm. The size of the sheet was then estimated as the length interval for which the chosen microsphere could be detected in the image. 10 targets were used and the width of the light sheet determined to be (19.2±2) μm. This value is larger than predicted above, most likely due to spherical aberration introduced by the cylindrical lens.

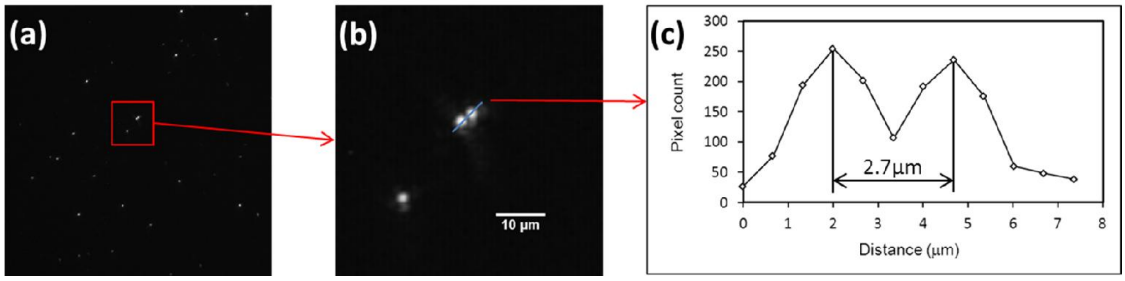

Figure 3-5 (a) Image of 2μm calibrated colloids in PAA under 10× objective. (b) Amplification of the image (a). (c) Profile of two spheres on the image, yielding a resolution of 2.7μm.

The resolution in the x-y plane was performed by analysing the local maxima of pixel intensity generated by the microspheres (Figure 3-5a). An estimate of the resolution of the system was determined from the smallest

distance between microspheres for which distinct peaks are resolvable (Figure 3-5b). The distance was assessed using a line scan bisecting the centre of a pair of apparently adjacent microspheres Figure 3-5c. The result indicates that our LST set-up can achieve a transverse resolution higher than 3 μm which is significantly smaller than the smallest feature that needs to be resolved for basic plant root phenotyping. This measuring result does not show the true limit of the resolution of the system. A better result on resolution maybe achieved with sub-resolution colloid.

To address the imaging depth of the system, a target consisting of a suture (0.10 ~ 0.149 mm diameter, W8830, blue, Johnson & Johnson) in transparent soil was examined. The space between grains in the transparent soil was saturated with 20% (w/v) sorbitol to provide RI matching. Images of the suture at different depths (2 mm ~ 5 mm, every 0.5 mm) were taken and the diameter of the suture on the images was calculated. The result showed that at depth from 2 mm to 4 mm, the apparent diameter of the images raised slightly from approximately 160 μm to 180 μm. However, image quality reduced more significantly when imaging deeper than 4 mm. In this case the transparency of the medium directly affects output image quality by degrading both the lateral resolution and the quality of light sheet, leading to a poorer axial resolution. In fact it is imperfections in the refractive index matching in the soil which set the limit on the resolution of the system. Hence sample preparation is critical both in the initial preparation of the sample and in maintaining the index matching as the plant grows.

3.3.2 Testing Samples

The first test material consisted of samples of lens cleaning tissue, an ideal test object due to its open fibrous structure. The tissue paper is typical of the kind of low density material that LST is particularly suited to imaging, and has fibres with diameter of approximately 20 μm (measured using bright field imaging, Figure 3-6a), which is about twice the size of the average cell in a root hair. The

results show that imaging using LST produced good contrast throughout the whole thickness of the sample (~120 μm) (Figure 3-6b) and we have used the data for 3D reconstruction.

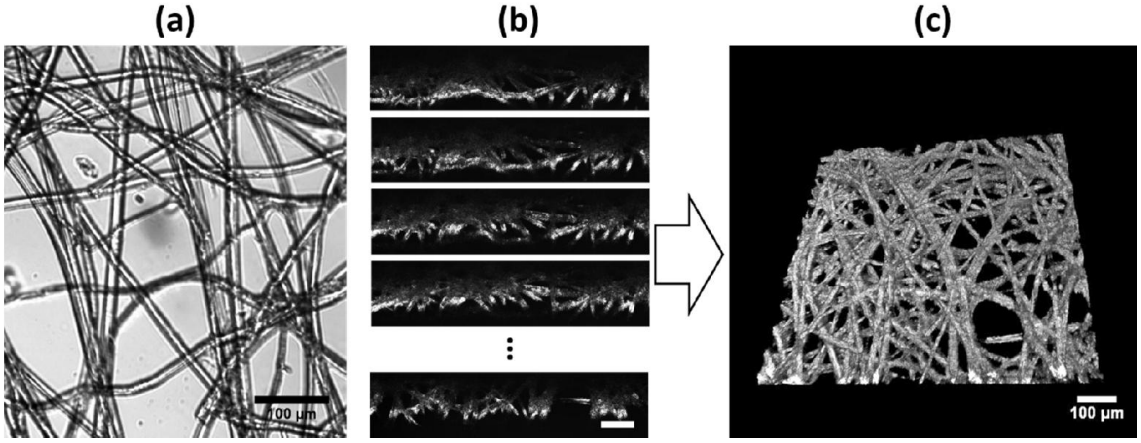

Figure 3-6 Images of lens tissue. (a) Brightfield image of the paper under 10× magnification showing 2D structure of lens tissue. (b) Individual sections of the sample illuminated by the light sheet. The laser was incident from the "bottom" of the images. Images were cropped to 1280×300 pixels to high light the details. The thickness of the laser sheet is 15.5μm by calculation and the laser power is 94uW. Scale bar 100 μm. (c) 3D image of the paper constructed by combining stacks of 2D images with ImageJ.

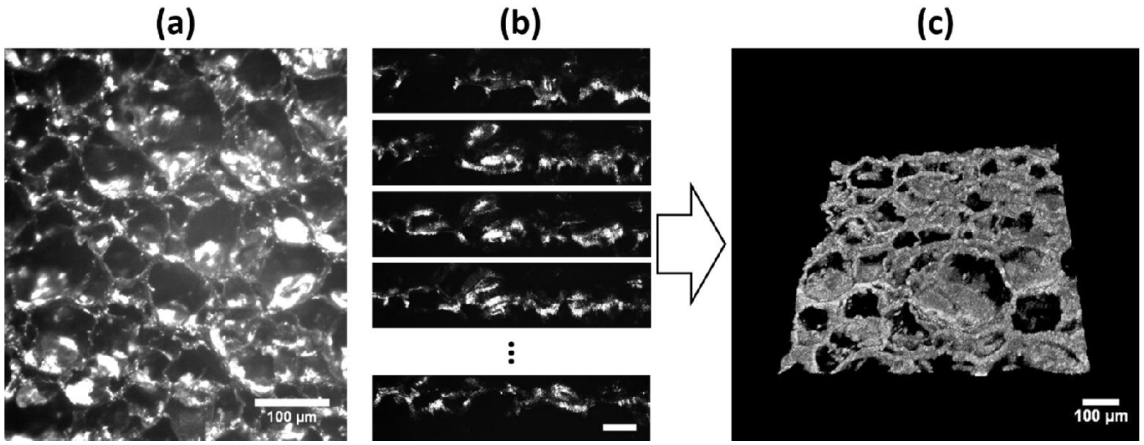

Figure 3-7 Images of dense foam. (a) Bright field image of the dense foam under 10× magnifications. (b) Different stacks of the sample by laser-sheet section. Images were cropped to 1280*300 pixels. The thickness of the laser sheet is 15.5μm and the power of input laser is 1.40mW. Scale bar 100 μm. (c) 3D image of the sample.

We have also used dense foam to illustrate imaging of a highly absorbing sample with complex surface topography. Since light absorption of these foams

was much higher than for the lens tissue, the power of the laser was increased to 1.40 mW.

On these samples, LST produced good contrast up to a depth of 200 μm in dense foam (Figure 3-7b), and 3D reconstruction of the data showed the system is suitable for imaging the topography of highly uneven surfaces (Figure 3-7b).

3.3.3 Three Dimensional Arabidopsis Roots

Arabidopsis root in transparent soil was imaged with 10X objective and EC1280 camera. Immediately before imaging, MSR nutrient media with 20% (w/v) sorbitol was added to saturate the substrate to allow transparency, Figure 3-8b. Thus images can be taken directly without the need to remove the sample from the soil.

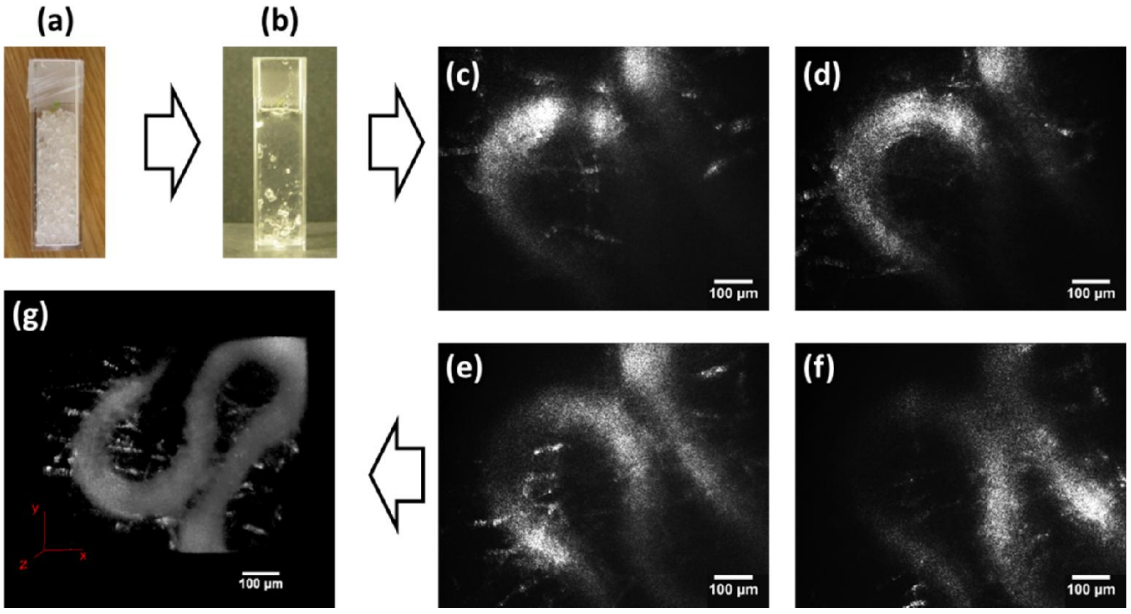

Figure 3-8 Root of a live *A. thaliana*. (a) Plant growing in transparent soil. (b) Sample after addition of refractive index matched solution. (c-f) Images slices obtained using LST demonstrate it allows detection of root hairs (e) and coarse anatomic features (c,d,f). LST is also suitable to image *A. thaliana* root 3D structure (g).Brightness in the image indicates the scattering from the sample.

Images of *Arabidopsis Thaliana* roots were obtained approximately 10 days after germination. Image sequences were taken perpendicular to the face of the

glass cuvettes. Images could be obtained throughout the depth of the roots (Figure 3-8 c-f) and had resolution sufficient to resolve anatomic features such as root hairs (Figure 3-8 e) or epidermis and cortex cells (Figure 3-8 d and e). Better sharpness was obtained when the light sheet was closer to the camera (Figure 3-8 d). 3D images of *A. thaliana* roots (Figure 3-8 g), revealed the structure of epidermal tissue and its spiral arrangement of cells. These results demonstrate the ability of LST to quantify microscopic root traits *in situ* and in a substrate that mimics soil physical structure. The root morphologies observed with LST in transparent soil [Figure 3-8] are atypical of those observed when plants are grown in gels where roots grow longer and straighter [116] but match those seen for *ex vivo* root samples from real soil.

3.3.4 Time-Lapse Imaging of Root Growth

1) Lettuce root in Phytagel

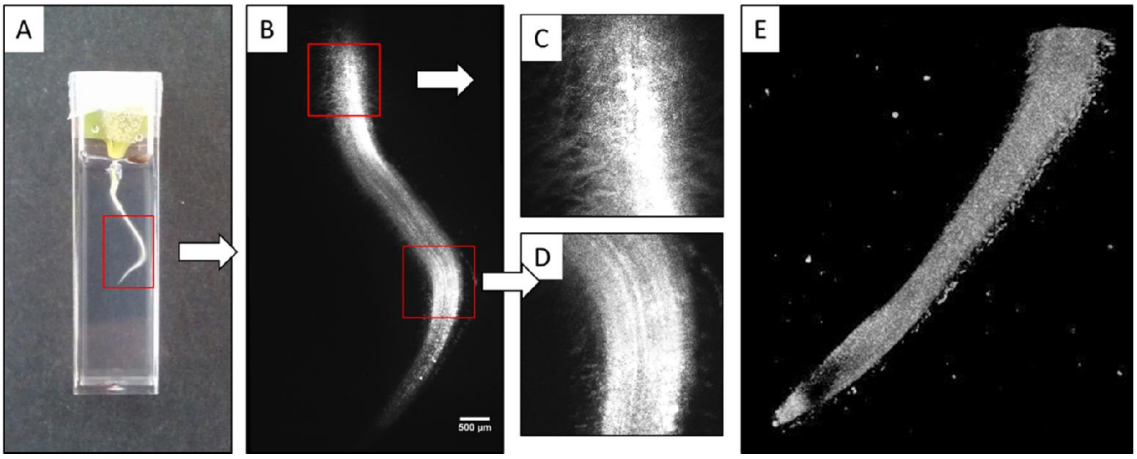

Figure 3-9 Lettuce root. (A) Lettuce root in cuvette. (B) Combined 2D root image. (C,D) Amplification from image (B). (E) 3D image of lettuce root.

On the day of imaging, i.e., day eight of sample setting, a cuvette was mounted onto the motorised stage with a piece of thick paper attached to it. The paper is working as an obstructer which allows upper part of the plant to get light for photosynthesis while the root part is still kept in the dark to allow producing high contrast images. A Thorlabs lamp (OSL1-EC, Thorlabs) was

simulating the light condition and providing energy for plant. Images along Z axis with interval of 6.5 μm were taken every 15 minutes for 18 hours. Thus we got 72 sets of image sequence for a plant. Step number along Z axis may vary with the orientation of the root: from 100 frames to 150 frames.

Figure 3-9 shows an image of the root in a large area. This image is combined from 3 separate images along the direction of root. Root hair and cell structure in the root can be clearly distinguished. Method for 3D reconstruction of the plant root Figure 3-9E is similar to Chapter 3.3.3.

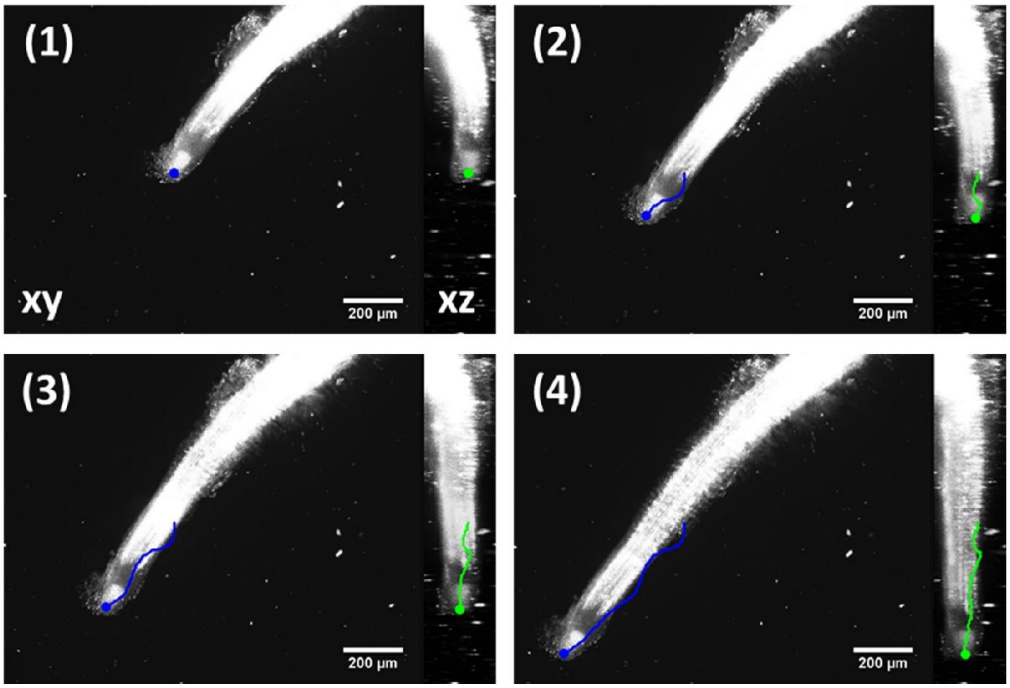

Figure 3-10 Images of lettuce root change in 18 hours. 1~4 indicate different time point with time interval of 6 hours. XY plane was obtained from Z projection of image stacks while XZ plane was reconstructed from 150-image sequence. Movement trajectory was achieved from manual tracking plugin in ImageJ.

Plant growth can be observed by taking frames of each time points to shows the maximum intensity projection in XY and XZ projection of the root, as shown in Figure 3-10. When roots were grown in gel, features of the root anatomy such as root hairs and root cap were clearly visible in both projections. Very little movement was observed in the region of root hairs which confirm division and cell elongation zone is between root cap and root hair [125].

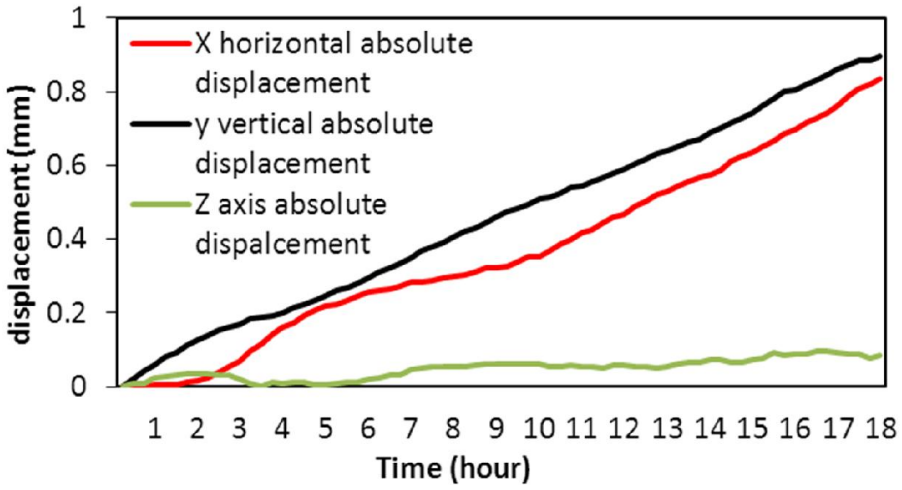

Figure 3-11 Moving speed of root cap with an overall average of 80 μm/hour

Tracking of the root tip was achieved manually. The position of the root tip was identified visually and marked manually so that the position of the root could be recorded at each time frame using ImageJ. The list of three dimensional coordinates was then used to determine the tip velocity in 3D space. The root tip velocity measured on a single sample using this approach indicated that root elongate at 80 μm/h on average. The elongation rate is therefore slower than that observed in a natural environment (1-2 cm per day). This is likely due to a lack of aeration of the media.

2) Lettuce root in transparent soil

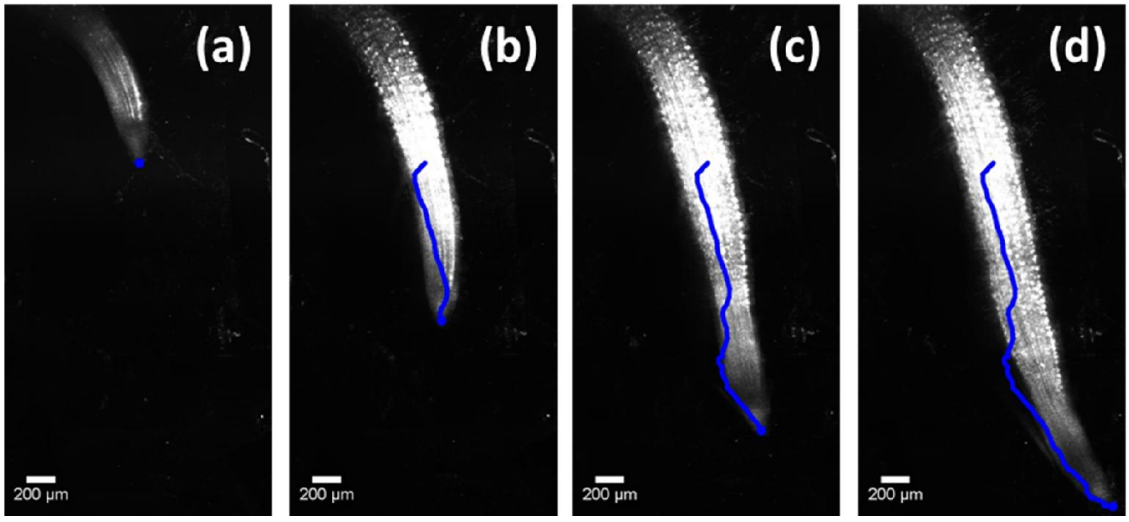

Figure 3-12 XY plane projected images of lettuce root at different time points. (a)-(d) are images taken at respectively 0h, 5h, 10h and 15h after the start of the experiment.

For comparison, Lettuce plants grown in transparent soil were analysed using the protocol described above. Images captured with interval of 15 minutes for 24 hours. Figure 3-12 shows the projections of root at time point 0, 5, 10 and 15 hours, respectively. The root tip grew out of range after 15 hours. In transparent soils, the quality of the light sheet is reduced due to inhomogeneous RI of the media cause by imperfect matching of the liquid and the particles, but also by the presence of air trapped in small cavities. The matching liquid based on Percoll® introduces also scattering in the liquid phase. The combination of these factors causes a severe reduction in the axial resolution of the images. However the image quality was still sufficient to extract quantitative information on root growth, with the root tip speed of one sample being 190 μm/s, significantly larger than that in Phytagel.

3.3.5 Conclusion

Light-sheet microscopy methods based on shaping light beam to thin sheet are playing an increasingly important role in biological studies. Due to the advantages of the light-sheet imaging method and newly developed transparent soils, a low-cost light-sheet tomography (LST) setup with the ability to take *in situ* 3D images of plant roots has been demonstrated for a better understanding of root-soil interaction.

A distinct advantage of the method is the very low light dose to which the roots are subjected whilst being able to maintain sufficient resolution to image the 3D microstructure of the root system. Results show that LST is a promising new technique for the study of root-soil interactions. With the use of newly developed transparent soils, it is possible to track root movements *in situ* during 18 hours or longer. Although the instrument presented did not achieve those obtained with microscopes such as LSFM, the important anatomical features needed for phenotyping such as root hairs and tissue structure could be observed. Another advantage of LST is that image formation does not rely on fluorescence

and genetically engineered lines expressing reporter genes. The technique is therefore widely applicable to most crop species. The simplicity and low cost of LST is also essential. In the future, portable instruments could be developed using the same concept and applied in glasshouses.

Though the use of scattering as a contrast mechanism means LST will not usually be able to achieve a resolution as good as that of LSFM. However it yields similar information in a much simpler and cheaper device, without the need for labelling or staining of the sample. In fact it is very complementary to LSFM: any LSFM system could easily be adapted to use for LST through the replacement of colour filters with neutral density filters and appropriate sample preparation. It is envisaged that the range of uses for LST could also be extended through the use of optical clearing techniques similar to those we use for rendering the soil transparent in this letter. In suitable samples it is still able to produce images with a resolution of less than 3 microns with only basic image reconstruction and without any need for image processing. This resolution, the overall quality of the images and the suitability for more densely scattering samples could be increased by the introduction of techniques such as structured illumination and de-convolution.

The lateral resolution obtainable with the setup presented in this study was shown to be 2.7 μm or greater with the main limitation on resolution being the accuracy of the refractive index matching in the sample.

We have shown the feasibility of the system for plant root phenotyping when combined with novel transparent soils by obtaining images of plant roots *in situ*. Clear 3D images were obtained without using fluorescence. Long term monitoring of lettuce root during 18 hours and tracking of root cap movement were achieved, yielding quantitative information on root growth rate.

Chapter 4
Light-Sheet Photoacoustic Imaging

When the scatterer density is low in the sample, optical imaging with scattered light can provide high resolution with good contrast. However, as discussed in Chapter 2.6, when optical scattering predominates for deep penetration or the scatterer density is so high that degrade spatial resolution, it is not the best option. On the other hand photoacoustic imaging, which is based on optical absorption to generate low-scattering acoustic signal, provides good contrast and resolution, and deep penetration for viewing the optical-absorbing structure deep inside the sample. In this chapter, a PA imaging system based on light-sheet illumination will be demonstrated.

4.1 Background

Photoacoustic imaging is also called optoacoustic imaging or thermoacoustic imaging, for it is based on the photoacoustic effect. The photoacoustic effect was reported as early as 1880 [126] but was limited by the technology at the time and it did not gain much application. Recently, with the development of short-pulse laser and high frequency acoustic transducers, work on photoacoustic imaging has come a long way [3].

Photoacoustic imaging is based on optical excitation and ultrasonic detection. Absorption of photons by molecules thermoelastically induces pressure waves, known as photoacoustic effect. During this process, energy from a nanosecond-pulsed laser is absorbed by the biological sample and results in a localized temperature rise, which induces thermal expansion and pressure waves. Approximately, a temperature rise of 1 mK results in a pressure rise of 800 Pa, which is above the noise level of a typical ultrasonic transducer [127]. After propagating through the sample, the ultrasound signal is detected by an ultrasound transducer (or a set of transducers) to form an image.

In photoacoustic imaging, optical energy is converted to ultrasonic energy and propagates as sound waves, which experience much less scatting. The conversion from optical wave to acoustic wave can bring several advantages:

1. Photoacoustic imaging breaks through the optical diffusion limit by taking advantage of much lower acoustic scattering in tissue [128].

2. Due to the different absorption efficiency of different molecules at different optical wavelength, optical contrasts according to chemical composition can be revealed.

3. Photoacoustic imaging is able to provide background-information free detection because generation of ultrasound is based on optical absorption; low absorption structure in the sample presents weak or no signal.

4. Compared to fluorescence imaging, photoacoustic imaging has larger application because all molecules are optically absorbing at some wavelengths and can be potentially imaged with photoacoustic imaging while much less molecules are fluorescent.

The optical absorption in biological samples is related to the molecular composition of the tissue. For instance, the absorbing spectrum of haemoglobin changes with the concentration of oxygen it carries. Oxygenated haemoglobin absorbs strongly up to 600 nm, and then its absorption drops very steeply. In contrast, the absorption of deoxygenated haemoglobin does not drop much at the

same wavelength. It decreases with increasing wavelength but stays relatively high. The oxygen saturation of haemoglobin is highly related to the metabolic state, hence it is an important diagnostic parameter, and potentially to quantify the hallmarks of cancer, for rapidly growing cancer cells need extra blood to develop a dense microvascular network around themselves to perpetuate tumour growth [129]. This makes photoacoustic imaging suitable for early detection of cancer development.

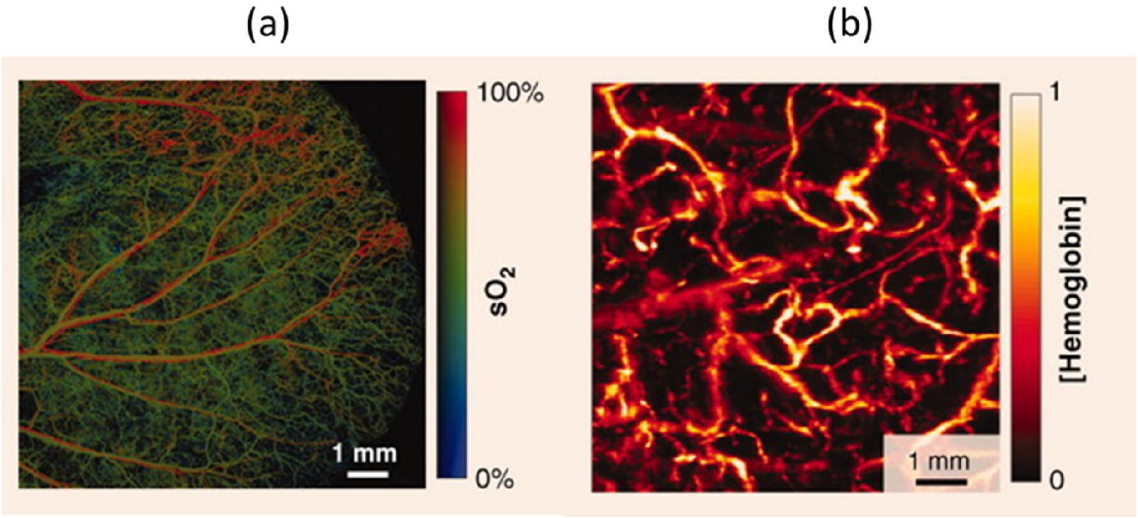

Figure 4-1 Reconstructed image of (a) optical resolution PAM of sO_2 in a mouse ear and (b) acoustic resolution PAM of normalized total haemoglobin concentration in a human palm [127].

In conventional photoacoustic imaging, which is mainly focused-scanning photoacoustic imaging, both the optical excitation and the ultrasonic detection are focused to increase lateral resolution, and the focus points are usually confocal to maximize sensitivity. Each laser pulse produces a one-dimensional depth-resolved image without mechanical scanning, called A-scan (amplitude scan). Then 2D transverse scanning would produce a 3D imaging. The axial resolution in PAM is reconstructed from the acoustic time, while the lateral resolution is determined by the overlap of the focus points. The image-construction strategy is the same as in ultrasound imaging. In the quantitative definition, resolution is the full widths at half maximum of the imaging system

responses to a point target which is usually smaller than the resolution. Depending on whether the optical or acoustic focus is better, PAM is classified into optical-resolution PAM (OR-PAM) [130], [131] and acoustic-resolution PAM (AR-PAM) [132], as shown in Figure 4-1.

OR-PAM is able to provide lateral resolution at cellular or even subcellular scale, ranging from hundreds of nanometres to microns [130]. As introduced above, the lateral resolution which is determined by the focus. Quantitively, the lateral resolution of OR-RAM is given by [127]

$$R_{lat,OR} = 0.51\ \lambda/NA \qquad \text{Eq. (4-1)}$$

Where λ is the optical wavelength and NA is the numerical aperture. The constant 0.51 is given by the full width at half maximum (FWHM) of the Airy disk intensity distribution.

Due to the short optical wavelength, micron scale focus can be easily achieved within optics, while on the contrary, if such resolution to be achieved with solo acoustic imaging, the centre frequency of the acoustic signal would have to be at least 300 MHz. At such high frequency, ultrasonic waves experience severe energy lost and can only propagate a few hundreds of microns in normal tissue, not even to mention the difficulty of fabrication of ultrasonic transducer at such high frequency. The advantage of OR-PAM is that the optical focusing can confine the photoacoustic signal for high lateral resolution while still maintaining imaging depth. The OR-PAM system in [130] achieved resolution down to single capillaries with imaging depth of 1.2 mm.

On the other hand, AR-PAM can break the optical diffusion limit and push the detection depth to a few millimetres by taking advantage of much lower acoustic scattering. The lateral resolution of AR-PAM is given by

$$\mathrm{R}_{lat,AR} = 0.71\ v_s/(NA * f_0) \qquad \text{Eq. (4-2)}$$

Where v_s is the speed of sound, NA is the acoustic numerical aperture, and f_0 is the photoacoustic center frequency, which is determined by the laser pulse

width, the targeted tissue depth, and the ultrasonic transducer's frequency response. For instance, with f_0 = 50MHz and NA = 0.44, AR-PAM has achieved a lateral resolution of 45 μm and an imaging depth of 3 mm [132]. Microvascular networks, as well as nevus, can be photo-acoustically imaged and analysed. To further increase the imaging depth to centimetres, even despite the lateral resolution, would require a more powerful laser, as well as lower pulse repetition rate. This not just delivers more energy and hence, more potentially bringing damage to the target, but also slows the transverse scanning process and makes it too slow for clinical applications.

To speed up the data acquisition, advanced ultrasonic array detectors are used for photoacoustic detection. With this array detector, the whole region of interest is illuminated by the laser, and the excited ultrasound signal is detected simultaneously by the transducers on the array. With the position information of each transducer, an inverse algorithm is applied to reconstruct an image [133], [134].

Despite the difference between the lateral resolution of OR-PAM and AR-PAM, the axial resolution of PAM system depends on both the width of the laser pulse and the width of the impulse response of the transducer. Pulse duration determines the centre frequency of generated ultrasound signal. For example, a visible laser with a pulse duration of 10 us or shorter is able to excite photoacoustic signal up to 100 MHz [3]. The spatial resolution of PAM, as well as the maximum imaging depth, is scaleable with the detected ultrasonic bandwidth [135]. For example, photoacoustic signals with 1 MHz bandwidth can provide approximately 1 mm spatial resolution because the velocity of sound in soft tissue is around 1.5 mm/μs. If the bandwidth is increased to 10 MHz, corresponding spatial resolution would be 0.1 mm, with the trade-off of penetration depth.

To achieve a better signal to noise ratio, a high energy pulse is preferred because the amplitude of the ultrasound signal is proportional to the absorbed

energy by the target. However, the energy of each pulse is limited for safety reasons. Usually the NA of the ultrasonic transducer is large enough to provide high signal to noise ratio, hence only one pulse laser alone is able to provide an A scan. However, the repetition rate of high-power pulsed laser is usually very low (at 10 Hz level), which is the main limitation of the scanning speed.

The reconstruction of an image is actually recovery of the initial distribution of absorbed energy from ultrasound signals acquired outside the object. Commonly in conventional PAM, as introduced before, reconstruction of a 2D image would involve B-scan (a cross-section scan, achieved by mechanically scanning the transducer). Since the interval of mechanical scanning determines the spatial resolution, to maintain the resolution of the imaging system, the amount of data for a reconstruction would increase with the size of the sample. For a large sample, the amount of data needed for a reconstruction is very large.

An alternative is section imaging. The detection of the ultrasound signal is limited to a 2D section within the investigated object by only illuminating a section of the object. Acquiring of the ultrasound signal is accomplished with a single-element cylindrical detector. The signal is taken while rotating the object. Then the image reconstruction within the optical section is done by back projecting the signals onto circles around the detector positions with radius $v_s * t$, where v_s is the speed of sound and t is the time of flight of the acoustic wave from the source to the detector, which can be synchronized from the burst of the laser pulse. However, this back projection is only accurate if the sensor is a point-like detector and has negligible size, which is usually not true because small size limits the amplitude of acquired signal. The finite size of the detector would cause blur at the periphery[136].

A way of avoiding the blur is using an ultrasound transducer larger than the object [137]. Here, we used a cylindrically focusing ultrasound transducer with PVDF active element, which extends in the cylinder axis direction and exceeds the size of the object to be imaged, so that the signal at a given time is

related to an integral of the initial pressure distribution along direction of the cylinder axis [138].

In this setup, since the arrangement of the rotation scanning is used, a 2D imaging reconstruction of large sample requires fewer scans than a complete tomography imaging, and leads to a faster process.

4.2 Materials and Methods

4.2.1 Acoustic Transducer Making

A cylindrically focusing transducer was built for detecting the ultrasonic signal.

Broadband transducers require the matching of the backing material and the piezoelectric element, and the matching of piezoelectric element to the coupling liquid. Hence, commercial PVDF film is an ideal active element with good flexibility, low acoustic impedance and natural low thickness: 1) The flexibility allows it to form arbitrary arc; 2) Low acoustic impedance provides good matching conditions to the backing material and the coupling medium, which is water under this condition; 3) Low thickness of PVDF as active element means that high centre frequency of the detection broadband can be achieved, and further leads to high spatial resolution.

The numerical aperture was chosen to be 0.5, which is a good trade-off between resolution and depth of field. The length of the cylinder (along the focal line of the cylinder) is 50 mm which extends the diameter of the target (5 mm diameter). The height of the cylinder is 25 mm, hence the focal length of the cylinder is also 25 mm to achieve the NA of 0.5. To achieve high lateral resolution, which is determined by the performance of the acoustic transducer, 28 μm thick PVDF film was used was the transducer active element.

An electrical wire was attached onto the positive electrode of the PVDF film with silver conductive epoxy. Then they were incubated at 80 degrees for 15

minutes to harden the conductive epoxy. This procedure also gives the connection point better conductivity. After cooling down, the PVDF film was covered onto the cylindrical mandrel, with the wire facing upwards. The casing was fixed onto the film and the tube temporarily with a clamp. The gap between the case and the film was padded with silicon grease to provide a sealed condition for filling the backing liquid.

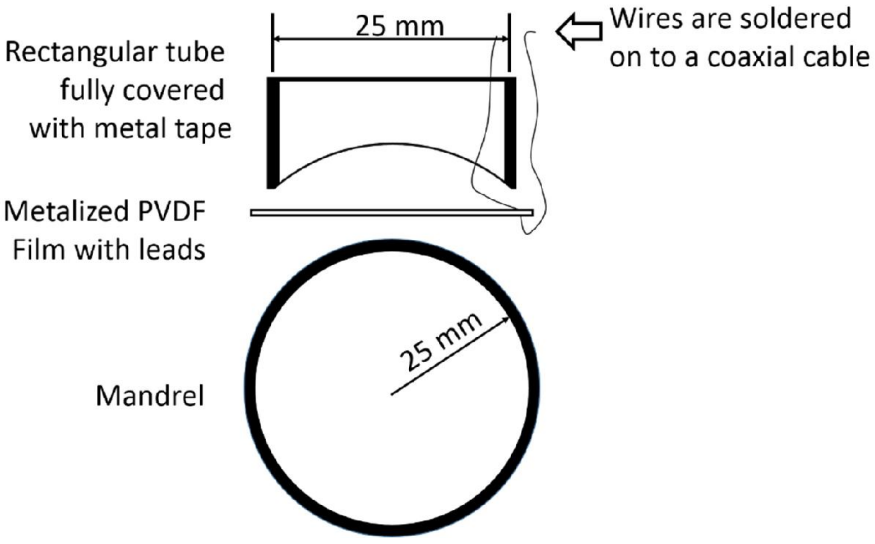

Figure 4-2 Assembly procedure for line-focus ultrasound transducer.

The required acoustic impedance of backing is $3.9*10^6$ kg/m^{2}s, which matches the acoustic impedance of PVDF film and therefore provides good range resolution. To achieve this impedance, a mixture of alumina (3 μm) and epoxy (volume fraction of 0.15 : 0.85) was used. The backing liquid was mixed under room temperature, then it was poured into the sealed casing and left at room temperature for 24 hours to wait for solidifying. The second wire was then attached onto the negative electrode of PVDF with silver conductive epoxy under the same procedure as the first one.

To increase the accuracy of this receiver, proper shielding is needed to minimise electrical interference on the transducer. The length of the leads which are connected onto the electrodes is kept at minimum, then the wires are soldered onto a coaxial cable. The back of the transducer is fully covered with metal tape.

The metal tape, the case of the transducer and the PVDF film, which are conductive, form a Faraday cage and then are connected onto the cathode.

4.2.2 Light-sheet Quality Comparison

The simplest way to create a light sheet from a light beam is to use a cylindrical lens, which is the method employed in Chapter 3. However, the light sheet generated this way suffers from non-uniformity of intensity distribution along the light sheet. This is because a laser beam is usually a Gaussian beam and has Gaussian intensity distribution from the first place. Cylindrical lens simply focuses the beam on one of the dimensions, thus has no improvement on this.

Another popular method is to introduce a laser scanner to scan a normal focused light beam up and down [34], usually with an acoustic-optic deflector (AOD). This method not only is able to provide even illumination along the sheet, but also allows use of other illumination methods, such as Bessel beam to improve the penetration depth [18], Airy beam to increase the FOV and structured illumination to improve the resolution [139]. However, introduction of an AOF will lead to increased cost of the system, and even more importantly, complexity of the system.

Apart from the cylindrical lens and scanned beam, there are other convenient methods to create light sheets, for example, with engineered line diffusers and Powell lenses.

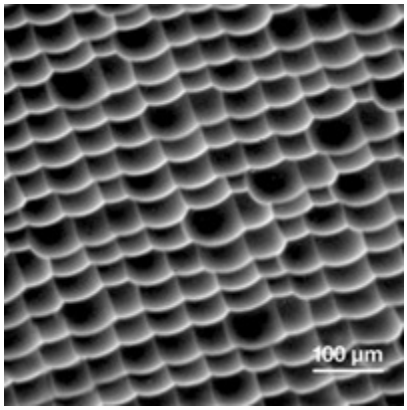

Figure 4-3 Micro structure of line generator (Photo source: Thorlabs.de)

An engineered line diffuser is a kind of DOE. It consists of micro-cavity units, as shown in Figure 4-3. The micro structure leads to diffraction of the beam and results in different diffraction patterns according to the dimensions of the structure.

A Powell lens resembles a round prism with a curved roof line. The curvature of the roof line varies with the size of the incoming laser beam. A Powell lens is sometimes called laser line generator as well. The Powell lens' round roof is a complex two-dimensional aspheric curve that decreases the light in the central area while increasing the light level at the line's end, and results in a uniformly illuminated line, as shown in Figure 4-4.

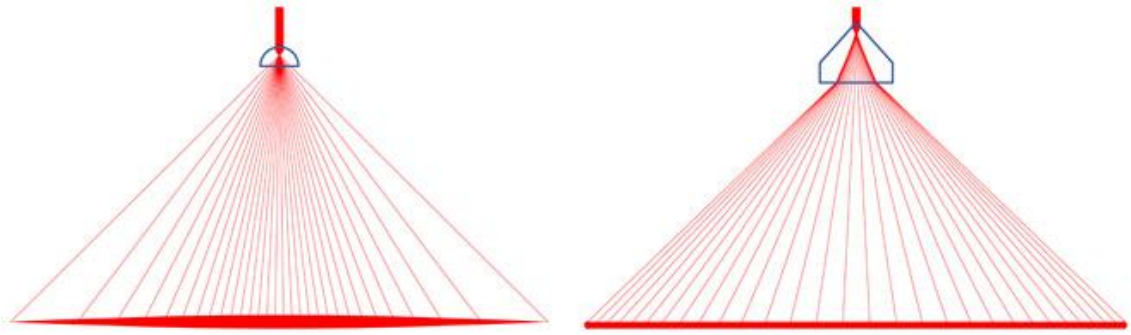

Figure 4-4 Comparison of the irradiation distribution of generated light sheet from a cylindrical lens and a powell lens (Photo source: laserlineoptics.com)

Here, the light sheets created by a cylindrical lens (LJ1567L1-A, FL = 100.00 mm, Thorlabs), an engineered line diffuser (ED1-L4100, 0.4º x 100º, Thorlabs) and a Powell lens (1-PL-1-B9101, laser beam width 1 mm, Fan angle 10º, Altechna, Lithuania) are compared to determine which is a better option for light sheet generation.

For the testing, a frequency-doubled solid-state laser (FCD488-020, JDSU, USA, wavelength 488nm, continues wave) was used as the illumination source. This laser provides better laser profile than the pulsed laser which would be used for photoacoustic signal generation.

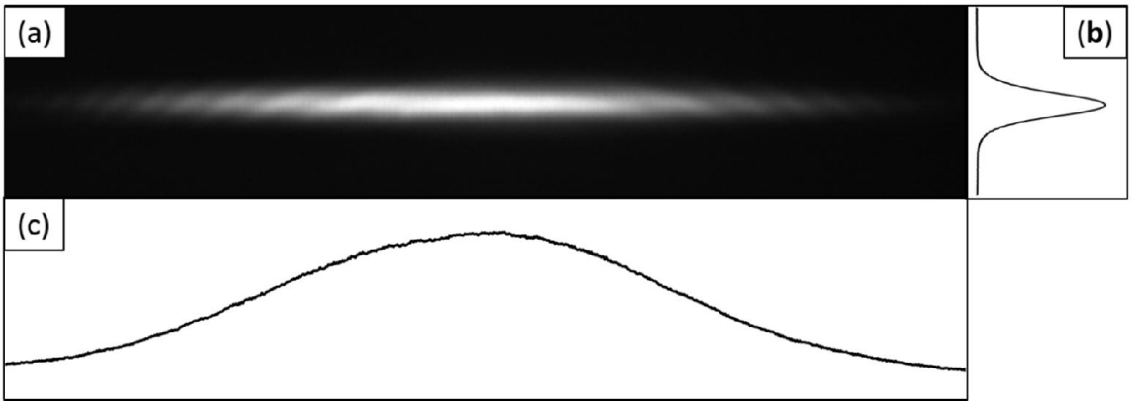

Figure 4-5 Light sheet and its profile from cylindrical lens. (a) Image of the focal line at focal point of cylindrical lens. (b,c) Plotted profile of selected region.

Figure 4-5 shows the beam profile of the light sheet created by the cylindrical lens. It is clearly shown that irradiation density of the focal line along both axes is still approximately Gaussian.

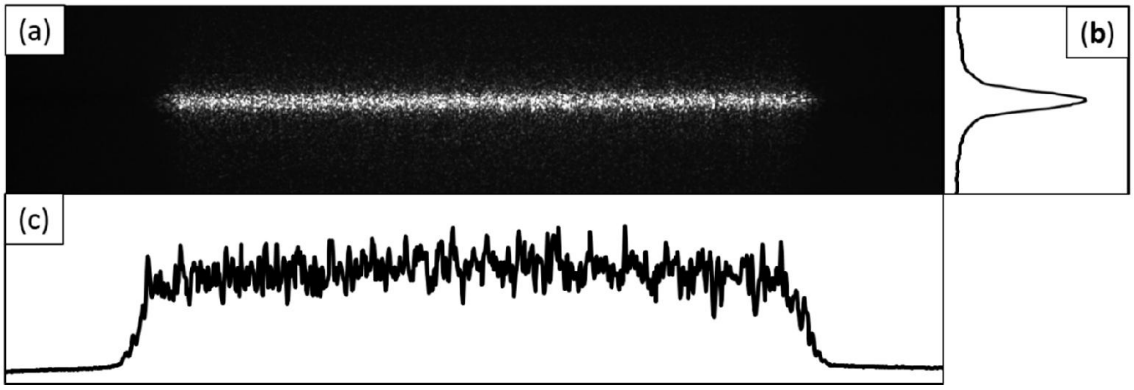

Figure 4-6 Light sheet and its profile from an engineered line generator. (a) Image of the focal line generated by engineered line generator. (b,c) Plotted profile of selected region.

Figure 4-6 shows the beam profile of the light sheet created by the engineered line generator. The beam profile along the line is well controlled and displays non-Gaussian intensity distribution. However, to ensure the diffuser is stable against variation in the input beam's intensity profile, the distribution of micro-cavities in the diffuser is randomized, which leads to the speckles beside the light sheet. In addition, diffraction perpendicular to the line results in the increase of light sheet thickness. This means for a given width of light sheet, the thickness of it is increased.

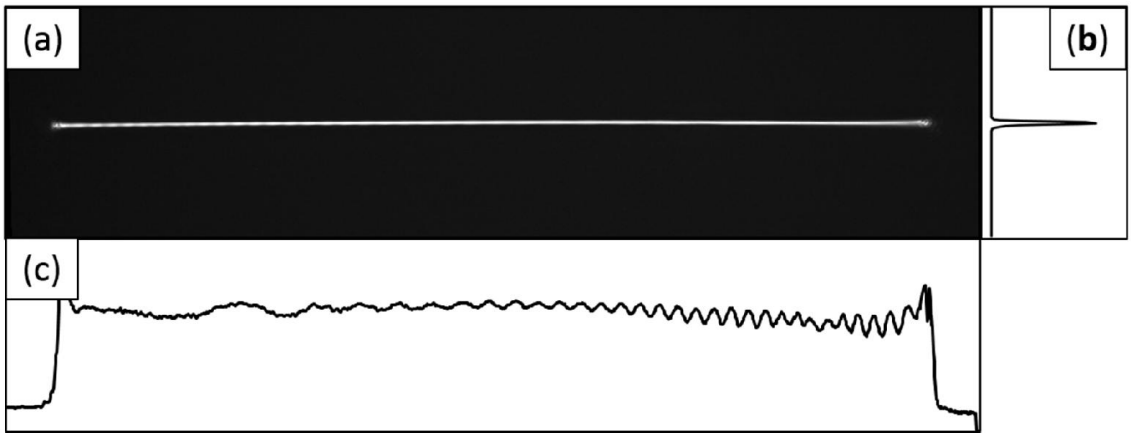

Figure 4-7 Light sheet and its profile from an Powell lens. (a) Image of the focal line generated by line generator. (b,c) Plotted profile of selected region.

Figure 4-7 shows the beam profile of the light sheet created by the Powell lens. The irradiation density along the line is maintained better. The ratio between the thickness and the width of the light sheet is greater than engineered line diffuser. It is worth notice that the roof line of Powell lens relocates the Gaussian profile of laser beam, but the energy distribution within the beam varies with the size of the laser beam. Hence Powell lenses are designed for a specific laser beam width. If the laser beam width differs from the Powell lens' designed laser beam width, the resulted light sheet will be affected. This is only a minor drawback, and can be tackled by a telescope with an optimised ratio.

From the results, we can see that Powell lens is the best choice for our purpose. It provides a wide light sheet and even illumination along the focus line.

4.2.3 Optical Arrangement

A 532 nm pulsed frequency-doubled Nd:YAG laser (Minilite II, Continuum, USA) was used to provide illumination. It has pulse width of 3 ~ 5 ns at maximum repetition rate of 15 Hz. The output power of the laser is controlled by a combination of a half-wave plate (WPH05M-532, 532 nm, Thorlabs) and a polarising beam splitter (PBS201, AR coating 420 - 680 nm, Thorlabs). The beam size at the aperture of the laser is 3 mm. It is rescaled with a telescope (FL = 100 mm and FL = 300 achromatic doublets from achromatic lens kit, LSB08-A, AR

coating 400 - 700 nm, Thorlabs) to 1mm. Then the beam is illuminated onto the Powell lens (1-PL-1-B9101, laser beam width 1 mm, Fan angle 10º, Altechna, Lithuania). An objective (4×/0.1, infinity corrected, Olympus, UK) is used after the Powell lens to collect the fast diverging light beam and forms a light sheet.

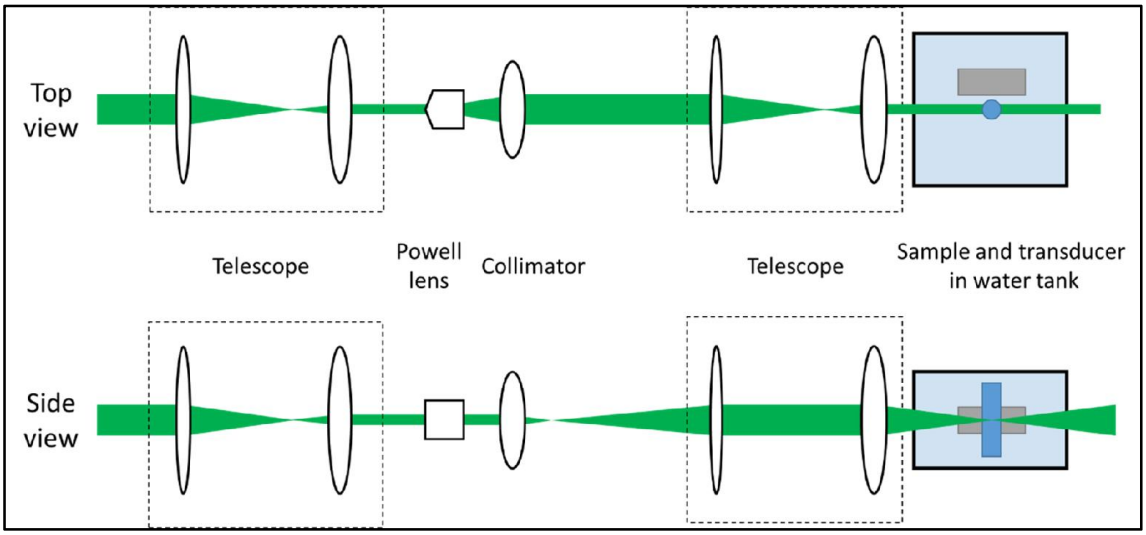

Figure 4-8 Optical arrangement for light-sheet photoacoustic imaging. A telescope scales the size of the beam to suit the Powell lens. The highly diverging light sheet is collected with a collimator, then the light sheet is imaged to the sample in a water chamber with a second telescope. Acoustic signal is collected with an ultrasound transducer.

Because of the limited distance from the objective and the focal line, another telescope is employed after the objective to image the light sheet and provides larger room for placing the water tank for sample. Achromatic doublets with FL = 250 mm and FL = 150 mm are chosen for the telescope. This set can also optimise the dimension of the light sheet with width of 5 mm and thickness 20 μm. The light sheet then enters a transparent water tank with sample and transducer.

4.2.4 Experimental Arrangement

The photoacoustic signal from the PVDF transducer is very weak. Hence the signal is amplified by 66 dB with a Pulser / Receiver (DPR 300, Imaginant Inc. USA). This pulser / receiver was also employed for testing the transducer

(Chapter 4.3.1). The PVDF transducer is connected to the 'receiver input connector' on the pulser / receiver. The received acoustic signal is amplified and output from 'receiver output connector', then goes to the oscilloscope (DSO 1014A, Agilent, USA). A PC is connected to oscilloscope via USB port for centre controlling and data saving.

For acquiring accurate data, synchronization of the events is essential. The Minilite laser provides a synchronization signal on the rear panel for easy synchronizing events. Its Q-SWITCH SYNC OUT signal, which lasts for 15 micro-seconds, occurs ~60 ns before the Q-switch opens. Considering the size of the sample (mm range) and the propagation speed of sound in water (1480 m/s), the interested time scale is in the micro-second scale. Hence a nano-second error is negligible, such as the time needed for the laser beam to travel from aperture to the sample, and the time needed for the synchronization signal to travel from the back panel of the laser to the oscilloscope. In brief, we can simply think that, at the rise of the Q-SWITCH SYNC OUT signal, the laser reaches the sample and induces the ultrasound. The distance between the sample and the transducer determines the time interval between the rise of the synchronization signal and beginning of time zone of interest.

The test sample is made of an electrical wire with a diameter of 140 μm embedded in Agar. The whole agar is held within a syringe, then attached onto an automatic rotation stage (PRM1/MZ8, Thorlabs). To record the data of an x-y-plane, the sample was rotated over 360º in 360 steps, with an increment of 1º on each step.

Stage motion and data acquisition were controlled in virtual instrument software LabVIEW. The execution process is shown in Figure 4-9. After the oscilloscope is initialized, it waits for the triggering signal from the laser. After receiving triggering signal on port 1, it records the acoustic signal on port 2 from the transducer with relevant delay which is calculated from the distance between the sample and the transducer. The data is then saved in a datasheet file on PC.

This is followed by an automatic stage rotation of 1°. This loop is executed 360 times and all the data is added onto the same datasheet file.

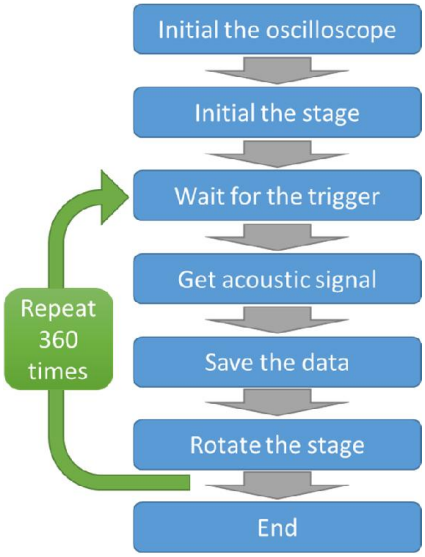

Figure 4-9 Execute process in LabVIEW

4.3 Results and Discuss

4.3.1 Transducer

To test the central frequency of the transducer, the admittance of the transducer was analysed. The real component of the admittance, called conductance, defines how easily the current to flow, and here, reflects the central frequency of the transducer.

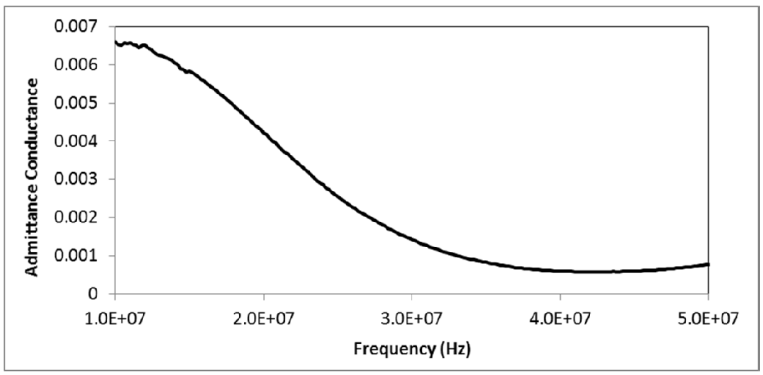

Figure 4-10 Admittance of the transducer

Figure 4-10 shows the conductance of the transducer versus frequency. It shows no obvious response from the transducer. This is mainly because the acoustic impedance of the backing material is the same as the PVDF film, which leads to a highly damped transducer.

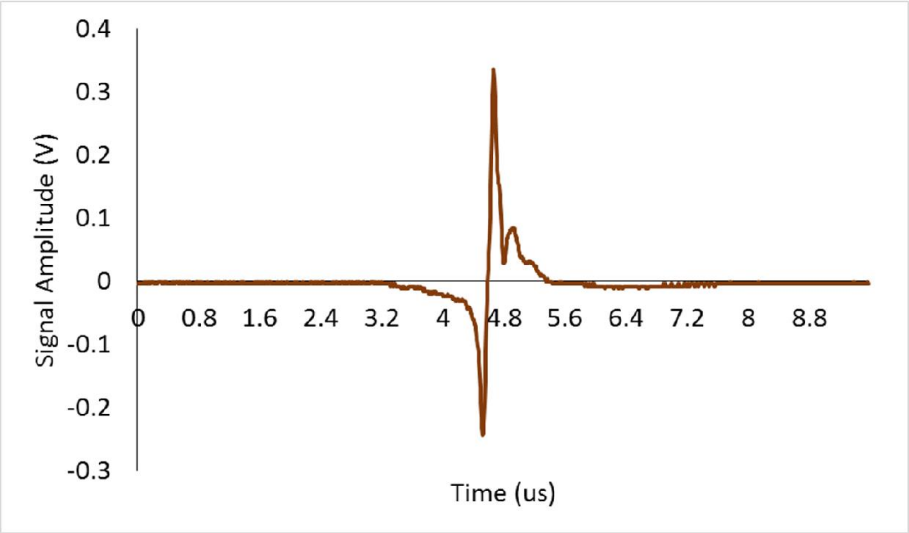

Figure 4-11 Waveform of the cylindrical transducer of an echo from a 10 MHz commercial transducer.

To test the response of this cylindrical line-focusing transducer, another commercial ultrasonic transducer (IMG5010 10MHz transducers Sonatest, UK) was placed on the focal line of this cylindrical detector, and driven by a Pulser / Receiver (DPR 300, Imaginant Inc. USA). The signal was picked up by the cylindrical transducer and shown in Figure 4-11.

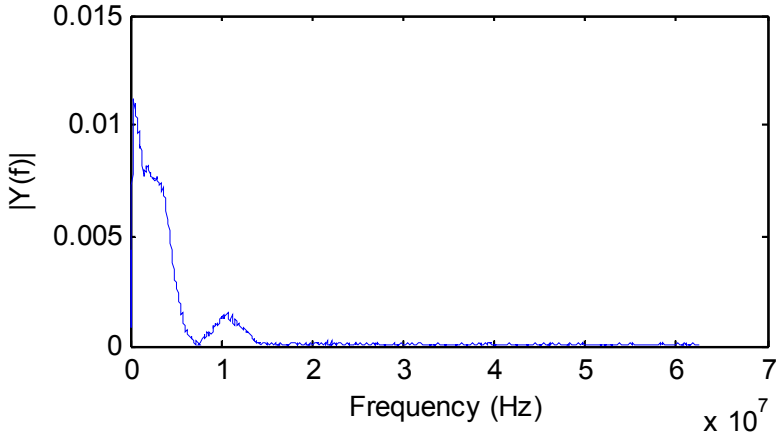

Figure 4-12 Spectrum of the signal acquired from a 10 MHz transducer

Figure 4-12 shows the spectrum of the signal in Figure 4-11. It shows that this home-made transducer is able to pick up signal up to around 15 MHz. However as this testing result is limited by the frequency of the sound source, higher frequency signals could be potentially measured if a higher frequency sound source was used.

4.3.2 Photoacoustic Imaging Results

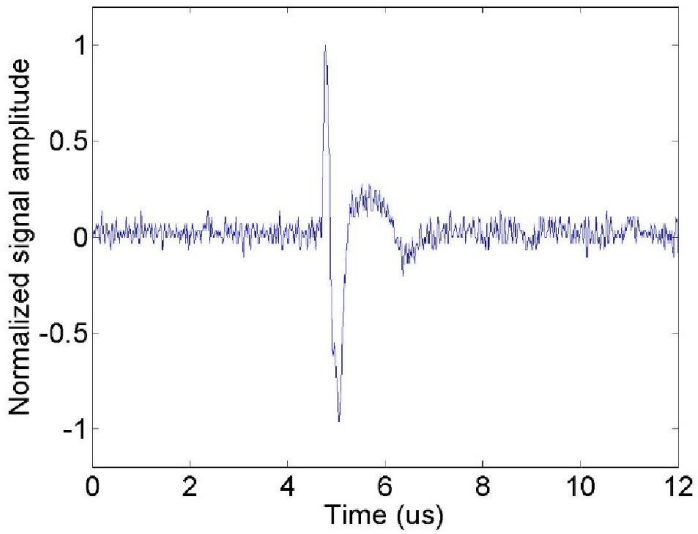

Figure 4-13 1D plot of the raw data

Agar samples with electrical wires of diameter 0.14 mm were imaged. Three different samples were tested, with 1, 2, and 4 wires respectively.

Figure 4-13 shows a sample data of a single scan. This data contains the information of distance between the transducer and the object(s), in this case, only a single wire.

To reconstruct a complete image, the sample was rotated 360 degrees with an interval of 1° each.

Figure 4-14 shows a complete data set of a 2D scan. The amplitude of the signal is normalized and shown as a different colour. Because of the rotation, the distance between the transducer and the target changes periodically. To construct

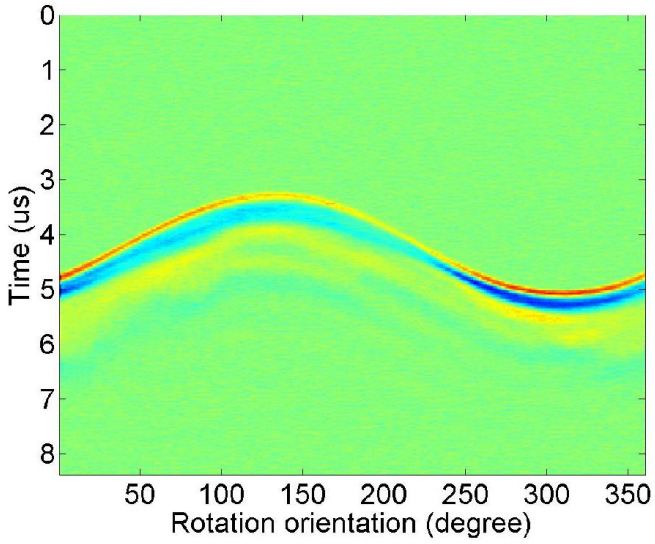

Figure 4-14 2D scan of a sample with one wire. Rotation of the sample results in the sine pattern of the signal.

a 2D image, the data was inverse Radon transformed [140], and the time relevant data was converted to length with the sound speed in water. The inverse Radon transformation of data in Figure 4-14 results in a 2D image of the sample, as shown in Figure 4-15. The amplitude of the signal is converted to brightness on the image.

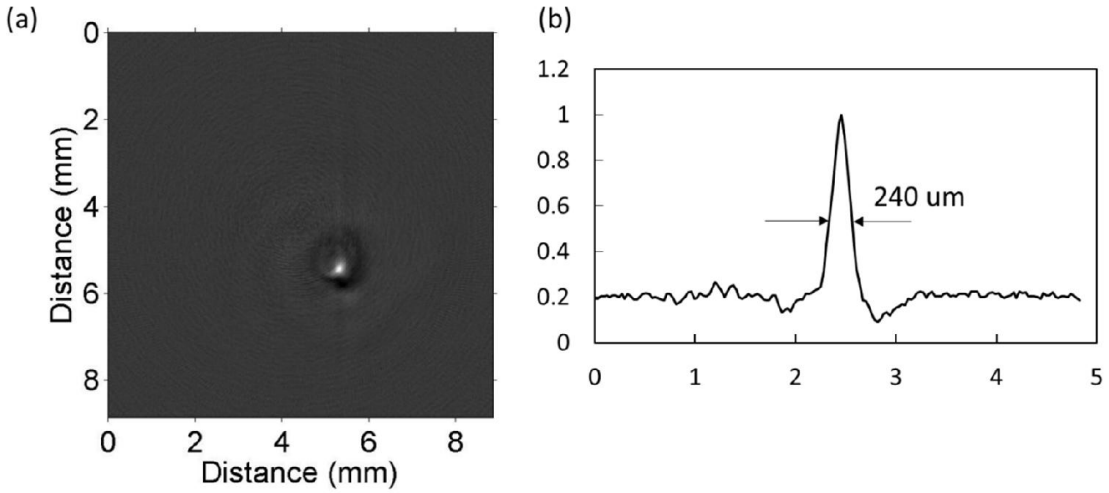

Figure 4-15 (a) Image of a single wire with a diameter of 140 μm in Agar. (b) Profile in of it shows a resolution of 240 μm.

A section of the image is taken and the profile is shown in Figure 4-15 (b), a width of 240 μm was measured. This resolution is lower than expected, which is

below 110 μm with a 28 μm thick PVDF film. With this experimental arrangement the resolution of the image is mainly determined by the performance of the acoustic transducer, which can be limited by the manufacturing quality. This can be potentially improved further.

More samples with two and four electrical wires were tested, as shown in Figure 4-16. The images are displayed with false colour to emphasize the amplitude. It shows that, even though the construction of the image is based on data taken with rotation, it is still capable of imaging the structure in large samples.

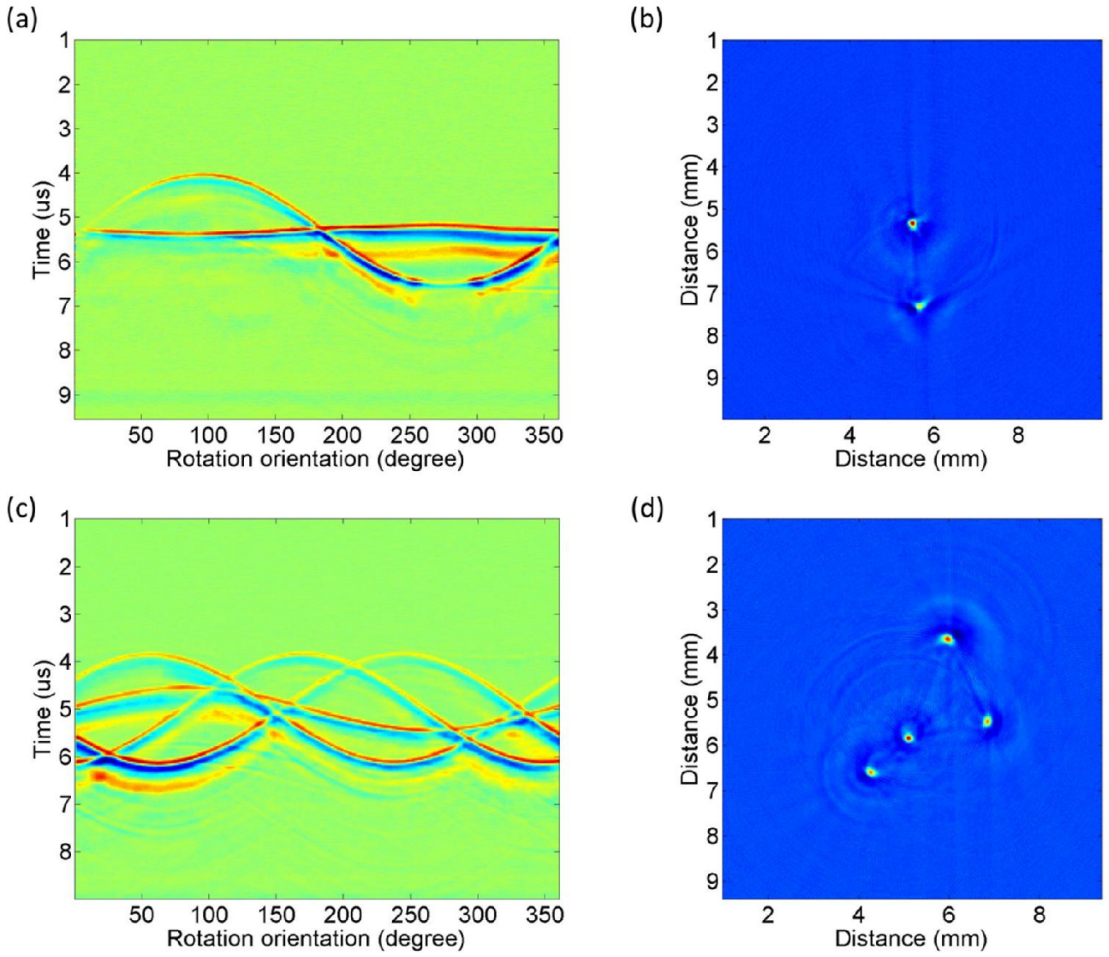

Figure 4-16 (a) 2D scan of two wires in Agar. (b) Reconstructed image of data from (a). (c) 2D scan of four wires in Agar. (b) Reconstructed image of data from (c).

Resolution perpendicular to the imaging plane is determined by the optical arrangement, for only the illuminated section can produce an ultrasound signal.

In our arrangement, it equals to the thickness of the light sheet, which is calculated to be 20 μm.

4.4 Conclusion

Photoacoustic imaging based on photoacoustic effect is gaining in importance in biological research. Taking the advantage of both light-sheet illumination and cylindrically line focusing, a light-sheet photoacoustic imaging system has been demonstrated.

Light-sheet illumination is a generic microscopic technique that has been mainly used for fluorescence imaging [95], as well as scattering imaging [141]. Due to its optical sectioning property, which means only illuminated part can be observed, the axial resolution is mainly determined by the thickness of the light sheet, and axial resolution is improved over bright-field microscopies. Moreover, light sheet illumination limits the dose of irradiation introduced onto the sample, hence photo-damage is greatly reduced.

A cylindrical line focusing PVDF film ultrasound transducer is customised for detecting acoustic signal generated by the target due to light-sheet illumination. The effect of finite detector size is avoided by using an integrating geometry with a detector larger than the investigated object. Signal acquisition is accomplished by rotating the sample within the light sheet, which has the same effect as rotating the transducer around a fixed imaging target. Image reconstruction is achieved by back projecting the signal with an inverse Radon transform.

In the photoacoustic effect, the amplitude of the acoustic signal is related to the optical energy incident onto the investigated object. Hence uniformity of the laser irradiation is essential for generation of an accurate acoustic signal. The optical profile of the light sheet generated from 1) cylindrical lens 2) engineered line diffuser and 3) Powell lens were compared, among which the Powell lens

provides the most uniform optical energy distribution. Hence the Powell lens is chosen to be used in optical setup.

The lateral resolution obtained with this setup is 240 μm with a 5 mm size sample. The main limitation on the resolution is the quality of the acoustic transducer. Although the resolution in PAM is not as comparable as in optical microscopies, PAM still benefits from other advantages, such as the large penetration depth due to less acoustic attenuation, and the optical contrast due to the natural property of the photoacoustic effect.

We have demonstrated a light-sheet illumination photoacoustic imaging system, with automatic control for data acquisition. 2D images of the samples were reconstructed.

Chapter 5

The Real Sonic Screw-driver: Acoustic Angular Momentum Transfer

Beam shaping is not only used in microscopy and imaging, like introduced in the last two chapter, it is also used for manipulation, both from the point of view of practical applications and to help bring better understanding of the fundamental nature of waves. Wave-matter interaction and manipulation is an actively investigated in optics. Scattering of light results in forces exerted on the target, which is used in optical tweezers devices for trapping and moving particles and cells. Light beams are suitable for precise manipulation of microscopic targets. . However, with large targets, optical devices are not suitable anymore, mainly because the force does not scale up with the dimension of the target due to the short wavelength, hence it could not provide enough force.

The concept in optical manipulation can be translated onto another form of waves, ultrasound waves. Ultrasound waves can be created with relatively high power transducers, which means more power (or momentums) can be carried in the beam. The long wavelength of sound waves also makes it possible to apply large forces to macroscopic targets. In this chapter, a 1000-element acoustic transducer array is employed to form acoustic helical beams with high

topological charge, to lift and rotate an acoustic absorber. Further quantitative study will be carried out to validate the ratio between angular and linear momentum, which is impractical to measure in a single experiment in optics due to the mismatched magnitude of the two quantities.

5.1 Background

Since the first demonstration of angular momentum transfer from a light beam to an object [142]; [58], a whole field on orbital angular momentum properties of optical vortices and novel modes such as Bessel and Laguerre-Gaussian beams has grown up. Many applications have arisen from the information content and rotational control that can be gained from a transfer of angular momentum from light to microscopic object [143] and basic physic research continues in this field [144].

Recently, analogous ultrasonic fields which contain orbital angular momentum have been explored [77], [78], and at the same time, theoretical predictions have been done to quantify the orbital angular momentum contained in helical acoustic beams[145]–[147].

There are many notable similarities between orbital angular momentum in acoustic beams and optical beams. Both photons and phonons carry $l\hbar$ of angular momentum and $\hbar\omega$ energy (where l is the topological charge of the vortex and ω the frequency of the wave), that means the ratio of angular momentum flux to power for both optics and acoustic is given by l/ω [148]. Despite the very fundamental nature of this ratio, neither optical nor acoustical experiments have ever managed to verify it in a single experiment. The main reason for this lack of direct experimental evidence is that, until now, no experiment has been able to accurately and simultaneously measure both linear momentum and orbital angular momentum.

In this chapter, we use a 1000-element ultrasound transducer array to achieve an unprecedented level of control on acoustic field, thus allowing us to produce a complete set of propagating ultrasound beams with the highest topological charge to date. This level of control allowed us to combine the measurement of both the linear and angular momentum of a beam simultaneously in a single experiment. Furthermore, the results achieved with high degree of precision and accuracy shows that they are adequate to test the fundamental ratio of orbital angular momentum to energy and the ratio does indeed hold.

5.1.1 Optical Orbital Angular Momentum

That light carries linear momentum is well known from the work of both Planck and Einstein, and since 1970s this is regularly observed in the lab in optical manipulation experiments. The linear momentum in light beam is h/λ per photon, where h is the Planck constant.

Additionally, light is able to carry angular momentum: both spin angular momentum (SAM) and orbital angular momentum (OAM) [149]. To be more specific, the spin angular momentum of light corresponds to the polarization state of the light beam and was studied early since 1936 [150]. If a light beam is circularly polarized, or more commonly elliptically polarized, each photon possesses $\pm\hbar = h/2\pi$ momentum. Orbital angular momentum was not discovered until 1992. A group at Leiden University in the Netherland identified that light beams with a helical phase structure carry an orbital angular momentum [151]. The orbital angular momentum of light is $l\hbar$ per photon [142], where l is the topological charge, corresponding to the number of phase cycles in one wavelength.

Both spin angular momentum and orbital angular momentum are along the propagation axis but the spin angular momentum has only two states, corresponding to the polarization direction, while the orbital component has a

number of states, with l taking any integer value. The bigger l, the more orbital angular momentum is in the photon. Hence orbital angular momentum in a photon can be much larger than its spin angular momentum.

It is worth noticing that spin angular momentum and orbital angular momentum are independent which means that a beam can carry either or both independently. An 'optical spanner' device demonstrated this and controlled spin and orbital angular momentum separately [9].

Production of spin angular momentum in light beams can be achieved with a quarter-wave plate which converts linear into circular polarized light. In the meantime, giving a light beam orbital angular momentum involves using cylindrical mode converters [142], spiral phase plates [14], or pitchfork holograms [56] with SLM.

When angular momentum is exerted on to a particle, it will cause the particle to rotate. However, from the naming of the two angular momentum we can get that, when the object is not in the beam propagation axis, the spin angular momentum will give a rotation to the particle around its own centre, while the orbital angular momentum will generate a revolution of the particle around the beam axis [58],[9].

Light beam with helical phase structure, or corkscrew shape wavefont, is called optical vortex. Topological charge of an optical vortex is always an integer, and can be positive or negative, depending on the direction of the twist. The higher the number of the twist, the faster the wavefront is spinning around aixs. Because of the light 'twisting' of an optical vortex, light waves at the axis cancel and results in a dark hole in the centre, as shown in Figure 5-1.

The most common form or helical beam is the so-called Laguerre-Gaussian (LG) mode. It is also known as 'doughnut' beam with an intensity amplitude minimum in the centre along the longitudinal axis. Allen et al demonstrated that the production of orbital angular momentum in light through Laguerre-Gaussian mode from Hermite-Gaussian beam with astigmatic optical elements. Moreover,

this momentum was successfully transferred to a microscopic particle, causing it to spin on the beam axis [142]. Later, this momentum transfer was demonstrated in an "optical spanner" experiment in which a focused LG beam is absorbed by a microscopic particle, leading the particle to rotate [9]. The rotation speed was investigated with the light beam with both spin angular momentum and orbital angular momentum (with $l = 1$). When the spin angular momentum and orbital angular momentum were in the same direction, the speed doubled; while they were at opposite direction, the speed cancelled. This confirmed that a Laguerre-Gaussian mode with $l = 1$ has a well-defined orbital angular momentum corresponding to $\hbar$ per photon.

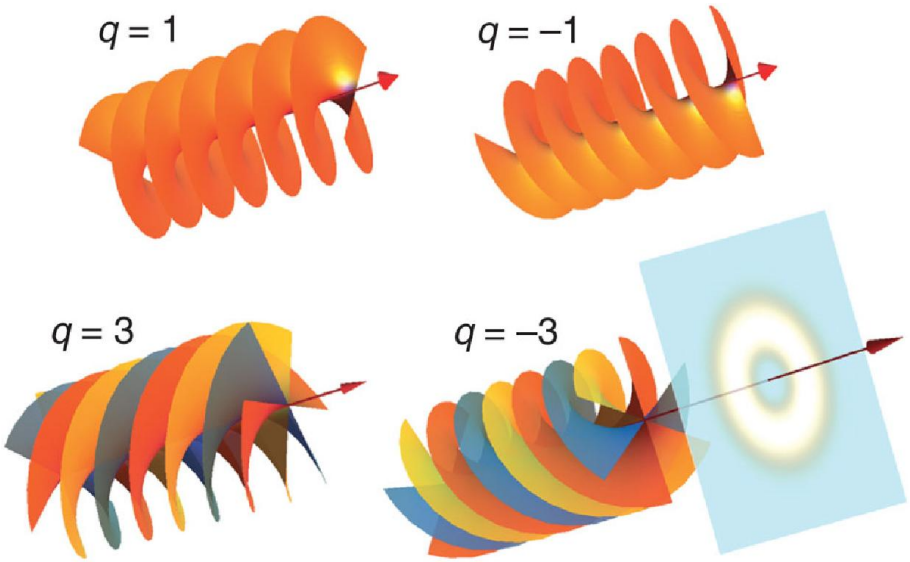

Figure 5-1 Schematics of the vortex-beam optical field with wavefront helical structures for topological charges $l = \pm 1$ and $= \pm 3$. The associated doughnut-shaped transverse intensity distribution is shown in the last example [152].

The orbital angular momentum in a vortex light beam makes it a very helpful tool to induce rotation of the trapped particles [58], [153]. Making use of the dark hollow of the centre along the propagation axis, high order LG mode beams are used to trap absorptive or reflective particles [58] due to scattering force, as well as dielectric low-index particles such as hollow glass spheres [154] due to the gradient force. The optical doughnut modes have also a good

application in trapping and guiding neutral atoms in 'atomic funnels' in the context of laser cooling [155], [156].

5.1.2 Orbital Angular Momentum in Acoustic Beam

Although described above as quantized in terms of photons, neither the spin nor orbital angular momentum, or energy, is solely a property of electromagnetic radiation, rather a generic property of all waves. However, since an acoustic beam is transmitting in gases and liquids as longitudinal beam rather than transverse wave, which means it is described as a scalar rather than a vector and hence has no polarization states. This means acoustic beams cannot carry spin angular momentum, but no such restriction exists on their orbital angular momentum, in other words, acoustic beams can carry orbital angular momentum.

Even though an acoustic beam is able to carry orbital angular momentum, experimental demonstration is hard to realize because acoustic helical beams with high topological charge are hard to produce.

An acoustic transducer similar to an optical spiral phase plate was built with to generate an acoustic helical beam [145]. It was composed of an annular sheet of PVDF attached at its outer edge to a ring of marine brass. The ring was cut at a point so that the ring could be twisted like the coil of a spring. By adjusting the height difference of the cut, corresponding to the wavelength of wave, a spiral-wavefront acoustic beam with $l = 1$ can be produced. This design was effective but had the limitation that, it could only work at certain frequency corresponding to the offset distance, with frequency changes requiring manual resetting.

This apparatus was improved with four-panel (four elements) configuration, each panel of which is individually addressed, and with appropriate phase to generate a helical beam [146]. The phase increase of the elements was 90 degrees rather than continuous. Because of the limited number

of elements and phase steps, this apparatus was only capable of producing a first order acoustical vortex.

An ultrasonic beam with a vortex wavefront was also obtained with an optoacoustic technique [157]. It was produced by illuminating a specially structured absorbing surface in a water tank with pulsed laser. The absorbing surface has a profile with a screw dislocation, which enable the shaping of helical beam. When illuminated by the laser, the absorber generates an ultrasonic wave with the desired wavefront in the water tank. They defined this technique as the optoacoustic realization of a diffractive acoustical element. However the result showed that only beam with $l = 1$ had the desired beam shape.

Comparison of orbital angular momentum in acoustic beams and that in optical beams was investigated [147], [158] by Thomas and Marchiano: they synthesized first and higher order acoustical vortices by using the inverse filter technique, implemented with hexagonal arrays of more than 50 piezoelectric transducers individually addressed.

In 2008, parallel works from two groups are presented to demonstrate momentum transfer from helical acoustical beam. K. D. Skeldon et al [78], have predicted and confirmed the orbital angular momentum content in acoustic beams. They used 16 loudspeakers, eight of which were used at any given time, each driven by an individual amplifier to generate the beams. The speakers have 8 phase output states ($\pi/4$ each step), thus the system was capable of providing acoustical vortex beams with $l = \pm 1$. With this setup, the helical property of the beam by observing the rotational Doppler shift, which results from the rotation between observed angular velocity and the beam source was also confirmed.

Volke-Sepúlveda et al [77], [159] also demonstrated the interaction with the matter and the transfer of their angular momentum content. Arrays of 4 and 8 individually controlled loudspeakers placed around a circle were used to generate acoustical vortices of first and second order. The helical beam creation device was similar to [146] but it was operating in continuous wave mode instead

of pulsed wave as in the former demonstration. A torsion pendulum with an optical fibre was used to measure the acoustic torque applied by the acoustical vortices. In addition, they demonstrated that second order vortex was delivering larger torque than that exerted by the first order. It was the first demonstration of acoustical angular momentum transfer with a vortex larger than the first order.

A few other methods to rotate objects with sound waves was demonstrated, for instance, by using a cavity with a square cross-section at resonant frequency [76], [160], or a rectangle with different lengths with a specific ratio [161]. Trapping rotating small particles with an acoustic needle which was vibrating at a flexural mode was also demonstrated [75]. These method did not involve angular momentum in acoustic beams. Moreover, all of them involved closed cavities and thus have the limitation of preventing free access to the sample.

5.1.3 Ratio of Orbital Angular Momentum to Energy in Vortex Beams

John Lekner demonstrated, in theory, that the angular momentum flux in acoustic beam is always equal to l/ω times the energy flux [148]

$$< L >= \frac{l}{\omega_B} < E > \qquad \text{Eq. (5-1)}$$

Where

$< L >$ is the angular momentum flux

$< E >$ is the energy flux

l is the topological charge

ω_B is the angular frequency of the beam

This equation was originally from the optical counterpart [142] and has been investigated in [78], [146], [162]. Though this ratio has a fundamental basis in physics, it has never previously been directly observed in a single experiment.

In the case of optics, this is mainly because that it is difficult to match efficiencies of the energy transfer, as linear momentum transfer relies on high

efficiency of scattering and angular momentum transfer usually depends on absorption and often has a low efficiency in an optical target. In addition, an optical tweezers setup requires a highly focused light beam, this would introduce a wide incident angle and bring distortion to the helical wave front.

In an acoustic study, as introduced in the last subchapter, previous work only worked with first and second order helical beams due to limited numbers of transducers [77], [78], [145], [146], [159], operating in audible range and were not able to produce a range of propagating ''Laguerre-Gaussian'' beam with versatile topological charge l.

In this chapter, we used a matrix array with approximately 1000 elements to explore both the linear and angular momentum carried by ultrasonic beams with much higher order helical vortices. With accurate measurement of levitation on a macroscopic acoustic absorber and its angular velocity, not only the angular momentum transfer is observed, but also the ratio of orbital angular momentum and energy in vortex beams [Eq. (5-1)] is confirmed.

5.2 Materials and Methods

5.2.1 Experimental Setup

The setup for measuring the levitation and rotation of a target in an acoustic vortex is shown in Figure 5-3. A commercial high intensity focused ultrasound system (ExAblate 2100, Insightec, Israel) was used to generate the helical beams. The ultrasound system, compromised of a 550 kHz matrix array with approximately 1000 elements, was developed for focused ultrasound surgery (FUS). The particular clinical application for this system is the palliative treatment of bone metastases (tumours), for which a matrix array must be able to be positioned on any anatomical location.

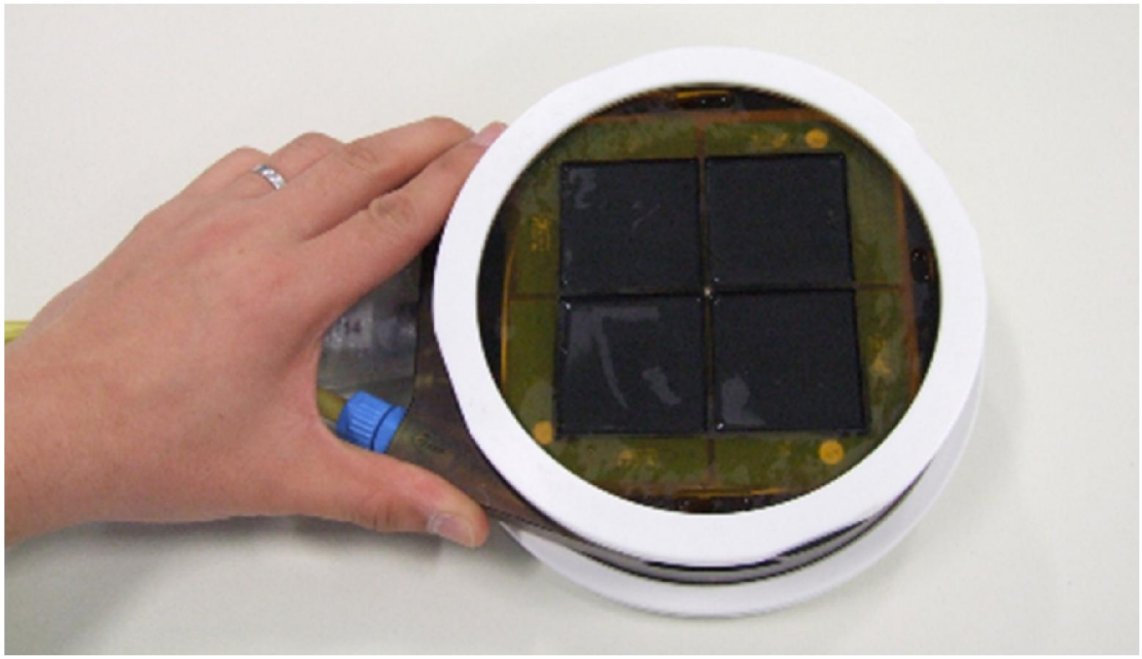

Figure 5-2 1000-element transducer array. This array is used in experiments for both Chapter 5 and Chapter 6.

The remote matrix array, shown in Figure 5-2, has a 74 mm square aperture and has a fluid chamber encased by an acoustically transparent membrane for acoustic coupling into tissue. Degassed water is circulating in the membrane to a water cooling system to prevent overheating of the elements. The array and control system are designed for both focusing and steering the beam within a 3D region of interest. The system instrumentation, therefore, is capable of generating high power continuous wave (CW) ultrasound beams with relative phases specified for individual elements, discretized to steps of $\pi/4$ by its software. By application of a pre-set phase to each element, the ultrasound beam can be focused at a desired location in a 3D region to treat a tumour in bone. Although the system is usually used with magnetic resonance image (MRI) guidance to specify the focal position from which source phases are calculated, we control directly both which elements are active, and the phases of transmitting elements during sonication, i.e. a CW excitation of the array elements. For all experiments, an approximately circular sub-aperture of the array was active to produce a cylindrical beam shape.

The target in these experiments was an 87 g, 100 mm diameter, 10 mm thick disk of acoustic absorber material (Aptflex F28, Precision Acoustics, Dorchester, UK); the disk is approximately 33 wavelengths (550 KHz) across at the operating frequency of the array. The acoustic absorber was placed in an optically transparent chamber with an acoustically transparent Mylar base, which was positioned above the matrix array (Figure 5-3).

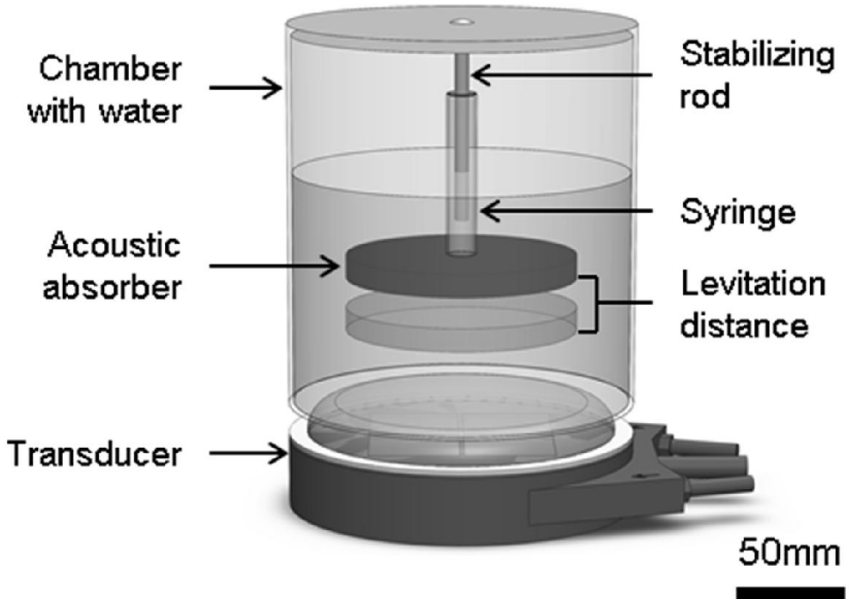

Figure 5-3 Diagram of experimental setup for levitating and rotating acoustic absorber target with transducer array at the base of a chamber filled with degassed water

The chamber was filled with degassed water to avoid cavitation during the experiments. A 5 ml plastic syringe body attached to the acoustic absorber provided alignment for both levitation and rotation about a stabilising rod suspended from the transparent chamber cover. In addition, the density of the Aptflex F28 material is 1.01 g/m^3, which is very close to that of water, thus the extra buoyancy force provided by the hollow syringe is enough to help it reach equilibrium state. The rod served only to stabilise the rotation and did not exert any vertical forces on the target (except for friction, which did not affect its equilibrium position and was also negligible in this case). With no applied field, the absorber or syringe assembly reached a neutrally buoyant position

approximately 35 mm above the array. The acoustically transparent membrane of the chamber base was coupled with a thin layer of water to the flattened, water-filled chamber housing the array. Those two layers of membranes were carefully coupled together so that no air bubbles were left between them, to avoid acoustic reflection due to impedance difference at the boundary of membrane and air.

The array and chamber were placed in a bespoke frame to keep the chamber stable. Two video cameras were positioned one at the side of and above the chamber. The one on the side was used to record the levitation and the one on the top was recording the rotation of the acoustic absorber during a sonication (the act of applying sound energy to target).

The total acoustic power, PA, generated by the array, as calibrated by the ExAblate FUS system, was varied with 23 W, 39W and 55 W to test the relationship between transferred angular momentum and applied power. The sonication lasts for 20 seconds in each case. This time length can ensure that an equilibrium state and constant angular velocity was reached for the angular momentum calculations. Enough interval time between each sonication was kept to make sure that the absorber disk and the water flow stopped before another sonication starts.

Then the videos recorded from the side were analysed to determine the axial displacement of the acoustic absorber, corresponding to the axial radiation force. The terminal angular velocity of the absorber, including the acceleration process, was extracted from the videos recorded from the top.

5.2.2 Applied Phase Profiles

To test the relationship between topological charge and angular momentum in the ultrasonic beam, azimuthal phase profiles φ with $0 \leq |l| \leq 12$, were applied to the array. In addition to the azimuthal phase shifts, radial phase shifts can be applied to the array aperture to focus the beam spherically to a specified

distance. For the present tests, the beam was focused at 70 or 100 mm above the transducer array, or left unfocused. When the beam was focused at 70 mm above the array, the energy from the beam was focused tightly onto the absorber, which causes the burn on the absorber. Thus experiment with beam focused at 70 mm was reduced and only the data set with acoustic power 55 W was tested.

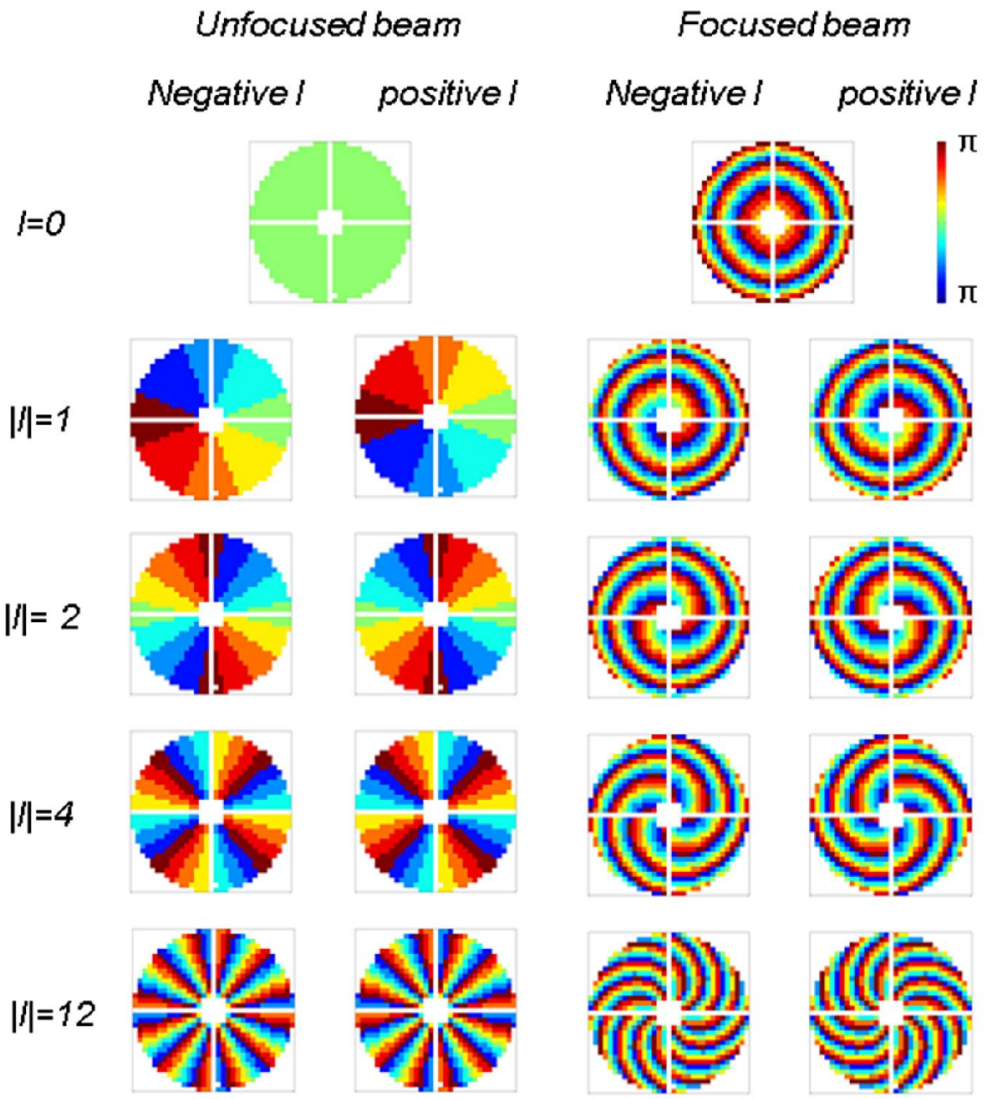

Figure 5-4 Applied phase profiles on the transducer array. Grey square indicates the real aperture of the array while white area indicated inactive elements (four corners) or grid on the array (two cross lines and the small square in the middle).

Examples of the phase profiles applied to the array are shown in Figure 5-4. The aperture of the transducer array is square, thus the elements at corners are turned off to create an approximately circular acoustic beam. Since the phase

output of the elements has only 8 discrete states with an interval of $\pi/4$, along with the finite number of source element, we only tested phase profiles with topological charge l up to ± 12. Figure 5-4 demonstrated that those high order helical beams can be produced without evidence of aliasing.

5.3 Result and Discuss

5.3.1 Simulation

(Simulation of acoustic field in Matlab was done by Christine E. M. Démoré.)

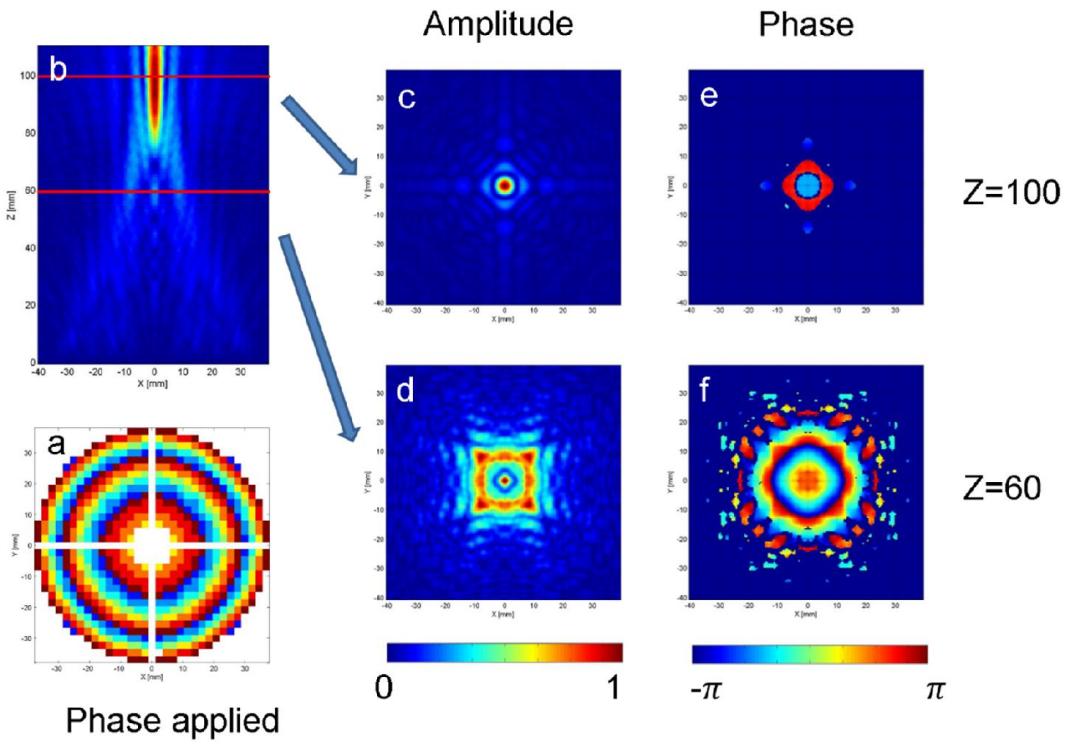

Figure 5-5 Simulation of acoustic field. The beam is focusing at 100 mm above the transducer with topological charge $l = 0$. (a) Applied phase on the elements. (b) Pressure amplitude on XZ plane with an intensity maximum at *Z* = 100 mm. (c, e) Amplitude and phase of XY plane at *Z* = 100mm. (d, f) Amplitude and phase of XY plane at *Z* = 60 mm. Apart from (b) with dimension of 80 mm × 110 mm, the others are all displayed with area of 80 mm × 80 mm, i.e. the aperture of the transducer array.

To predict the result and further verify results from measurement, the acoustic field was simulated in Matlab based on a Fourier acoustics approach [163], with the information of the geometry of the transducer array and property

of the elements. The transducer array was assumed to be in an open free space filled with water.

Figure 5-5 shows an example of complete simulation result of the acoustic beam generated with the transducer array, which focuses at 100 mm above the transducer with topological charge $l = 0$, i.e. normal focused beam without vortex.

Figure 5-6 shows the simulated acoustic field of ultrasonic beams with various topological charge l =1, 6 and 12, unfocused and focused at 100 mm above the transducer.

From the simulated results, we can see the doughnut shape of the pressure field with intensity minimums in the centre along the beam propagation axis, which meets our expectation.

In addition, with appropriately applied phases, the simulation results suggested that within 50 mm above the transducer (where the acoustic absorber would be), the ultrasonic beams do not diverge much, thus the reflection of acoustic power from the plastic chamber is negligible, which makes the open space assumption valid.

5.3.2 Hydrophone Test

The real ultrasound field was characterized in a three-dimensional ($1 \times 1 \times 1$ m^3) scanning tank, with a needle hydrophone (0.2 mm Probe, Precision Acoustics, UK). Free-field profiles were generated, and subsequently used to validate the fields for the transducer located within the chamber. Hydrophone test is able to directly provide both amplitude and phase information in an acoustic field, by referencing to a constant signal with the same frequency. It is worth noticed that in optics, phase cannot be measured directly without the interference technique.

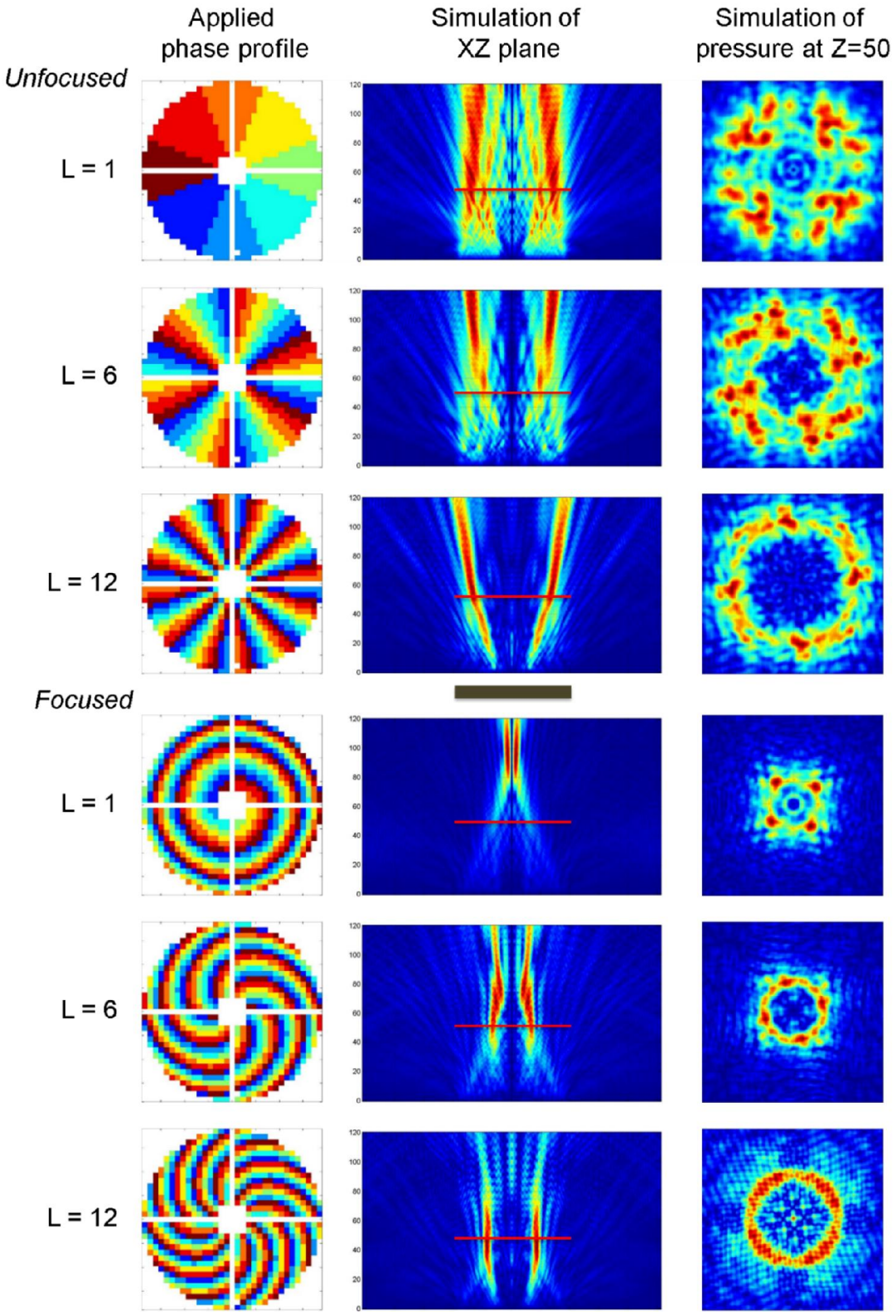

Figure 5-6 Simulation of the pressure in the acoustic field, unfocused beam or focused at 100 mm above the transducer array. The first column is the applied phase profiles on the transducer array, aperture 80 × 80 mm. The second column is the pressure graph of simulated XZ plane area 200 × 120 mm. The grey bar indicates the size and position of the acoustic array. The red lines indicate the height of the third column which is the simulated pressure field of XY plane at Z = 50 mm.

Three phase profiles were applied to the ExAblate 2100 transducer array and the acoustic field was scanned at the XY plane about 60 mm above the transducer, the same height as shown in Figure 5-5. The result from hydrophone scanning demonstrated good agreement with the Matlab simulation of the pressure field.

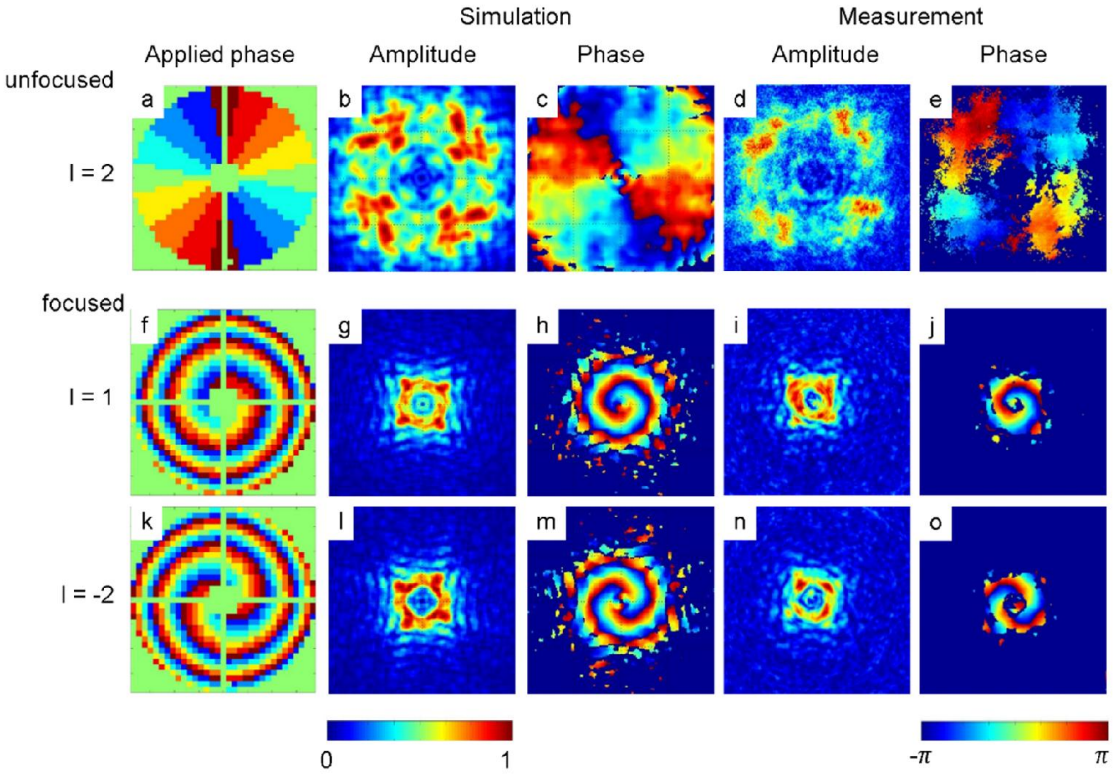

Figure 5-7 Applied phase profiles of transducer array, simulated and measured pressure of helical beams with topological charge l at a plane approximately 60 mm above the transducer surface. Display area is 80 mm square.

5.3.3 Levitation Force

The experimental demonstration of the angular momentum in an ultrasonic beam is given by the observation of angular momentum transferred to the acoustic absorber target. When acoustic beams impinge upon the absorber they are almost entirely absorbed (>95%) and the absorber is seen to be levitated to a new equilibrium position, along with the rotation starting with the acceleration

of angular velocity until reaching a stable angular velocity, for the duration of the sonication (20 seconds in total).

The observed rotation direction changes with the sign of the vortex wave front in applied phase profile. This demonstrated that the rotation of the absorber is due to the angular momentum transferred from the sound beam, rather than the radiation pressure caused by the asymmetry of the beam or the setup. In addition, it can be further validated that when ultrasonic beams without vortex ($l = 0$) were produced, the absorber was only levitated because of the radiation force, but not rotated.

From the recorded videos, evident levitation can be observed; angular rotation of the absorber can also be automatically tracked by the movement of the marker on the absorber. Rotation of the absorber was not perfectly circular, and the acoustic absorber did not always stay completely parallel to the array during levitation because only the top of the syringe was in contact with the stabilising rod, which allowed the acoustic absorber to sway off centre. Nevertheless, before the end of the sonication, the levitated position and angular velocity of the absorber reached a stable state, allowing the exerted acoustic radiation force and orbital angular momentum to be quantified.

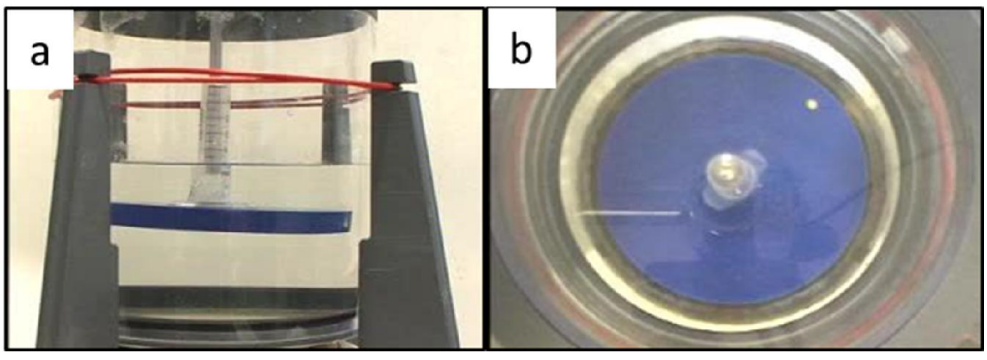

Figure 5-8 Video capture, (a) Side view enables the levitation force measurement. (b) Top view enables the extraction of angular motion information. (Video available at: http://www.youtube.com/watch?v=SeB69CcLEI8)

The variation of the levitation of the acoustic absorber disk, h, between its position at the beginning and at equilibrium during sonication, can be extracted

from video taken from the side by the graduated marks on the syringe. Thus the acoustic radiation force on the target because of an incident acoustic beam, which is determined from the apparent change in the buoyancy force, can be obtained. The axial force, F_z, from the acoustic beam is given by

$$F_z = \rho g A h \qquad \text{Eq. (5-2)}$$

Where ρ is the density of water (1000 kg m^{-3})

g is the acceleration due to gravity

A is the cross-sectional areal of the syringe, which related to the column of displaced water is given by

$$A = \frac{1}{4}\pi D^2 \qquad \text{Eq. (5-3)}$$

Where D is the outer diameter of the syringe.

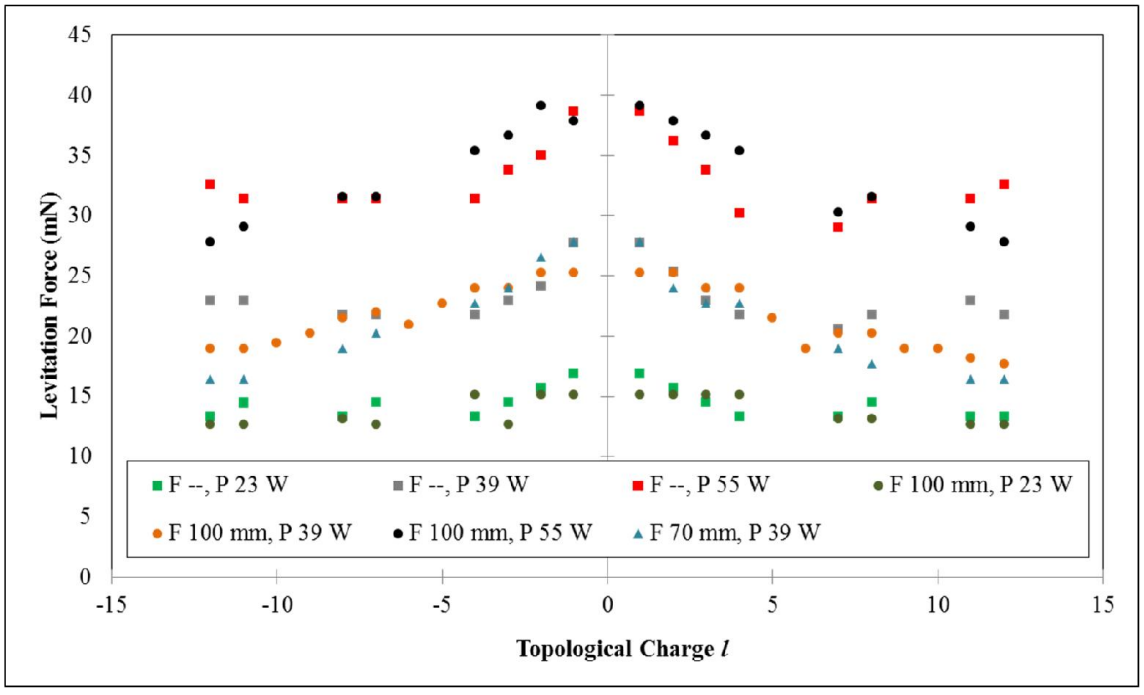

Figure 5-9 Levitation force F_Z v.s. topological charge l. Extracted from the change of syringe high before the sonication and during the sonication when an equilibrium states is reached. Levitation force increases with the increment of the power (P 23W, P 39W and P 55W), and the focal distance (F 70mm, F 100mm and F -- which means unfocused).

The variation of the levitation force, i.e. the acoustic radiation force on the absorber is shown in Figure 5-9. The beam was focused at 70 mm, 100 mm above the transducer array or not focused (marked as F--), and the calibrated output acoustic power was varied with 23 W, 39 W and 55 W. A systematic increase in the levitation distance with power was evidently shown, as expected, due to the increased axial acoustic radiation pressure. The trend of reduced levitation force, with increased number of l was also observed. The change of levitation force with focal distance is not significant.

5.3.4 Angular Velocity

The top view camera allowed us to observe the rotational motion from the acceleration phase through to terminal stable angular velocity. A contrasting-colour marker on the acoustic absorber used allowed a tracking algorithm to be applied to extract accurate and precise angular position information on the absorber, thus the instantaneous angular velocity, not just final angular velocity at balance [164]. An example data set for the absorber motion in a single sonication of 20 second is shown below in Figure 5-10:

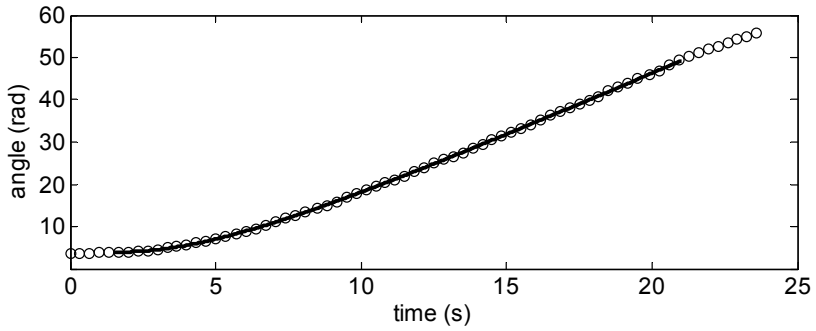

Figure 5-10 Example of the angular motion of the acoustic absorber, shown as empty circles. The solid line shows the curve fitting result of equation of motion [Eq. (5-17)].

Sonication started about 2 seconds after the video started. We can notice that the absorber accelerated until getting to a stable state with a constant angular

velocity until the end of sonication, and then started to slow down when the sonication is over after 20 seconds.

The observed relationship between the stable angular velocity and the topological charge of the ultrasound beams is shown in Figure 5-11. As with the last subchapter, the beam was focused at 70 mm, 100 mm above the transducer array or not focused (marked as F--), and the output acoustic power was varied to be 23 W, 39 W and 55 W.

From the result we can notice that the angular velocity increases generally linearly with l at low order of topological charge. In addition, the change in rotation direction with l demonstrates that this effect is due to the angular momentum carried by the ultrasound beam.

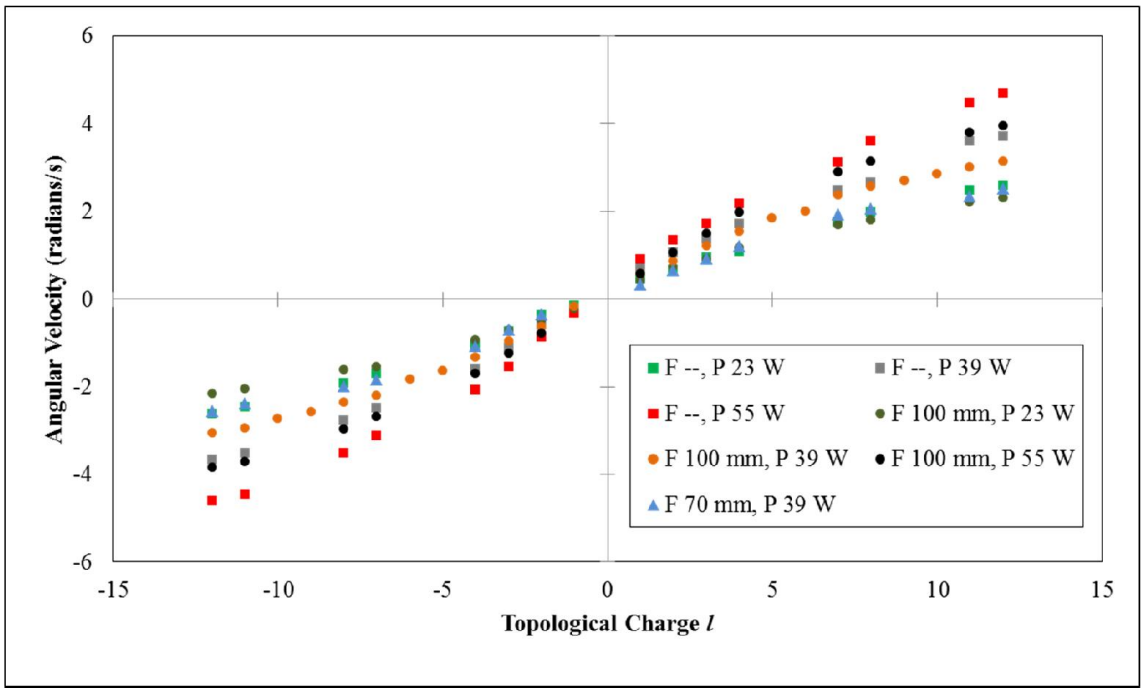

Figure 5-11 Terminal angular velocity ω_A v.s. topological charge l with transmitted acoustic power of 23 W, 39 W and 55 W, and focal distance 70 mm, 100 mm and unfocused. It is clearly shown that angular velocity increases generally linearly with l at low order of topological charge.

With the same phase profile, i.e. the same focus and the same topological charge, the angular velocity is larger with higher acoustic power. This fits to the prediction that higher acoustic power would introduce more orbital angular

momentum in the beam, thus more angular momentum is transferred to the absorber. Moreover, under the same topological charge and acoustic power, the unfocused beam carries the most orbital angular momentum, whilst the beam which focuses at 100 mm above the transducer is the next most effective, and the beams focuses at 70 mm above transducer the least. This effect can be explained by the inclination of the wavefronts in the beam. While an unfocused beam has axial and tangential components of momentum, a focused beam has a radial component towards the focal point. While the spherical focusing used these experiments and using a target larger than the beam, the radial components cancel out, but reduce the net remaining momentum to transfer to the absorber.

5.3.5 Ratio of Orbital Angular Momentum to Energy in Vortex Beams

1) Drag coefficient from angular acceleration.

The terminal angular velocity of the absorber, ω_A, was obtained in the last subchapter (Figure 5-11), from which angular momentum can be calculated. The angular momentum, L_A transferred to the acoustic absorber, which is proportional to the angular velocity of the acoustic absorber, is calculated from

$$L_A = I\omega_A \qquad \text{Eq. (5-4)}$$

Using the moment of inertia I of the absorber about its axis of rotation, $10.9\text{x}10^{-6}$ kg·m^2.

The top view camera allowed us to observe the rotational motion from the acceleration phase through to terminal angular velocity. When the acoustic absorber is levitated and starting to rotate, the torque applied on the disk is constant since the acoustic power is constant. A portion of this torque has to overcome the drag from water, and the rest accelerates the spin of the acoustic absorber until a stable angular velocity was reached.

The drag coefficient of the fluid depends on the shape of the object and on the Reynolds number (Re), which depends on specific conditions of the system.

Consider the flow over a flat disk which rotates about the centre with a uniform angular velocity, ω_A, in an stationary incompressible fluid (water), as discussed in [165], the flow over the disk is laminar for Reynolds number

$$Re = \frac{\omega_A r^2}{\nu} \qquad \text{Eq. (5-5)}$$

Where r is the radius of the disk, ν is the kinematic viscosity of water, which is $1.002 \times 10^{-6}\ m^2/s$.

The system is laminar for Re less than about 4.5×10^4, and fully turbulent for Re greater than about 3.9×10^5 [165], [166].

Putting the maximum angular velocity of our result which is 4.7 radians/s and radius of the disk 0.05 m into equation, we get to a Re number of 11700. This is much smaller than the criterion above. We can safely assume the rotation of the absorber is under laminar flow without turbulence, i.e. we have a Stoke's drag on the absorber.

According to Stoke's law, for a linear motion, the frictional force is proportional to the velocity and can be expressed in the form

$$F_{drag} = -bv \qquad \text{Eq. (5-6)}$$

Where

b is the drag coefficient constant under Stoke's drag

v is the linear velocity

Under the rotation scenario, it has a the similar form

$$\Gamma_{drag} = -C\omega = -C\dot{\theta} \qquad \text{Eq. (5-7)}$$

Where

Γ_{drag} is the drag torque on the absorber

C is the drag coefficient constant under rotation

ω is the angular velocity

θ is the angular displacement

Since the torque applied on the acoustic absorber is constant, Γ_B, the differential equation for this rotational motion is given by

$$\Gamma_B - C\dot{\theta} = I\ddot{\theta} \qquad \text{Eq. (5-8)}$$

Where

Γ_B is the torque applied by the beam, equal to the angular momentum current from the beam into the absorber, $< L >$.

In this system, the acoustic absorber is driven only by the acoustic beam, and all the momentum exerted by the acoustic beam is absorbed by the absorbing disk, hence the torque applied on the acoustic absorber is equal to the torque applied by the beam

$$\Gamma_B = \Gamma_A \qquad \text{Eq. (5-9)}$$

When the absorber reaches its terminal velocity, the drag on the absorber Γ_A is also proportional to the terminal angular frequency of the absorber ω_A through the constant drag coefficient C.

$$\Gamma_A = C\omega_A \qquad \text{Eq. (5-10)}$$

We get

$$C\omega_A = I\frac{d^2\theta}{dt^2} + C\frac{d\theta}{dt} \qquad \text{Eq. (5-11)}$$

With the initial state of the acoustic absorber

$$\begin{matrix} t(0) = t_0 \\ \theta(0) = \theta_0 \end{matrix} \qquad \text{Eq. (5-12)}$$

And terminal equilibrium state

$$\lim_{t\to\infty}\frac{d\theta}{dt} = \omega_A \qquad \text{Eq. (5-13)}$$

There is a linear analogy model for this. Consider a ball falling in laminar flow, experiencing only gravity, buoyancy and Stoke's drag, as shown in Figure 5-12. The net force of gravity and buoyancy overcome Stoke's drag and provides

power for acceleration. At terminal states, velocity reaches to a constant value and net force equals to Stoke's drag. The equation of motion is:

$$F_{gravity} - F_{buoyancy} = F_{net} = ma + bv \qquad \text{Eq. (5-14)}$$

Where m is the mass of the ball, a is the acceleration of the ball, b is the Stoke's drag on the ball, v is the linear speed of the ball.

This motion has a solution as follows:

$$y(t) = v_t t + (1 - e^{-t/\tau}) + v_t(e^{-t/\tau} - 1) \qquad \text{Eq. (5-15)}$$

Where the characteristic time τ is the ratio m/b, and v_t is the terminal velocity of the ball.

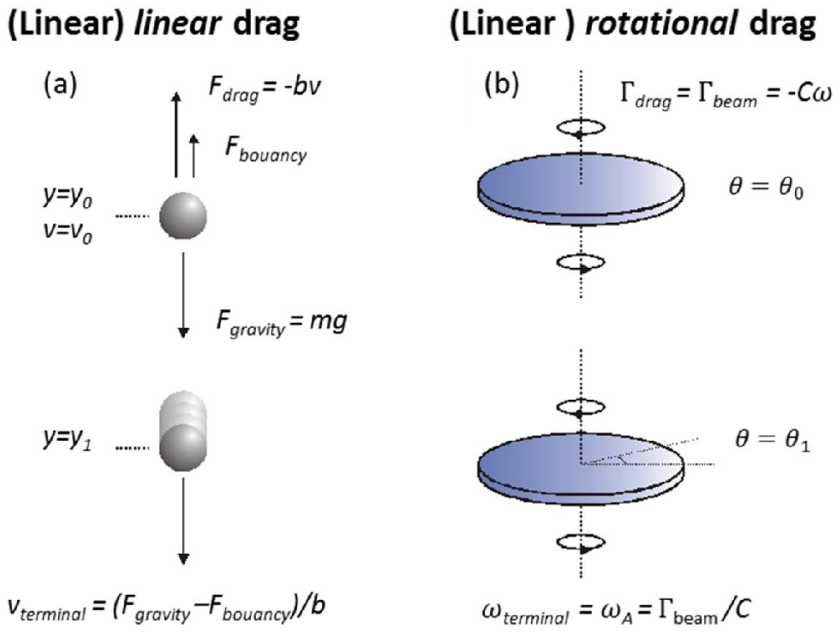

Figure 5-12 Linear drag and rotational drag in laminar flow. Rotation model is the analogue from the linear case on the left

By analogy to the linear case the solution for this is as follows:

$$\theta(t) = \omega_A t + (1 - e^{-t/\tau}) + \omega_A(e^{-t/\tau} - 1) \qquad \text{Eq. (5-16)}$$

Where $\tau = I/C$ is the characteristic time of the acceleration phase. When the terminal velocity is reached, t >> τ , the applied torque is balanced by the drag torque and Eq. (5-16) reduces to a linear function with slope ω_A.

The drag coefficient C is calculated by fitting the complete from of Eq. (5-16) to full data sets in the acceleration process. One sample of the fit is shown in Figure 5-10, which confirms that the assumption of the linear drag is valid. This yields an average value for C of $(2.9 \pm 0.2) \times 10^{-5}$ kg m^{2}s^{-1}.

2) Drag coefficient from 'Golden Ratio'

We can consider the rotation motion from another aspect, assuming the 'Golden Ratio' of orbital angular momentum to energy is valid, and the drag coefficient can be calculated.

$$< L >= \frac{l}{\omega_B} < E > \qquad \text{Eq. (5-1)}$$

When observing the transfer of angular momentum, the key characteristic of the beam is in fact the time average of the angular momentum current, $< L_Z >$, because the transfer of the extremely small amount of momentum carried by a single photon, or phonon in this case, is difficult to observe. When a vortex beam impinges upon an object, part or all of $< L_Z >$ is absorbed, leading to a rate of change of angular momentum dLz/dt. dLz/dt is also the definition for the torque, Γ, exerted upon an object. The predicted Equation Eq. (5-1) [78], [146], [148], [162] can be modified so that

$$\frac{< L_Z >}{P} = \frac{l}{\omega_B} \qquad \text{Eq. (5-17)}$$

Where

1. ω_B is the angular frequency of the beam and can be obtained from

$$\omega_B = 2\pi f \qquad \text{Eq. (5-18)}$$

Where f is the frequency of the beam.

2. P is the total power in the beam, and can be measured from the levitation force exerted upon the object, F_z, multiplied by the speed of sound in fluid, c (1482 m / s for water at room temperature).

$$P = cF_z \qquad \text{Eq. (5-19)}$$

This is the standard method to accurately measure the power in a beam [170], [171].

From the result above, Eq. (5-17) can be transformed to

$$\frac{\Gamma_B}{cF_z} = \frac{l}{2\pi f} \qquad \text{Eq. (5-20)}$$

Hence, by measuring the ratio of the torque exerted by a beam on the acoustic absorber to its levitation force, we can directly measure the ratio of orbital angular momentum to energy of a helical beam.

Since

$$\Gamma_B = \Gamma_A = C\omega_A \qquad \text{Eq. (5-21)}$$

From above we can get to the equations as below, the ratio of topological charge and drag coefficient

$$\frac{l}{C} = \frac{\omega_A}{cF_Z} * 2\pi f \qquad \text{Eq. (5-22)}$$

With all the result in the last subchapter (Figure 5-9, Figure 5-11), we get to ratio of angular velocity to incident power multiplied by wave frequency (s/kg.m^2), all data sets lie on a straight line. The slope of the linear fit [which according to Eq. (5-22) should be $1/C$] to all the data in Figure 5-13 is 3.35 ± 0.36 × 10^4 s/kg m^2, which lead to a the value of drag coefficient C = 3.02 ± 0.3 × 10^{-5} kg m^2/s.

5.4 Conclusion

With acoustic transducer array in ExAblate 2100 system, we created various ultrasonic beams with vortex wave front to levitate and rotate a macro acoustic absorber.

We have demonstrated that with this 1000-element transducer array, high order acoustic vortex beam can be generated without aliasing. This has been

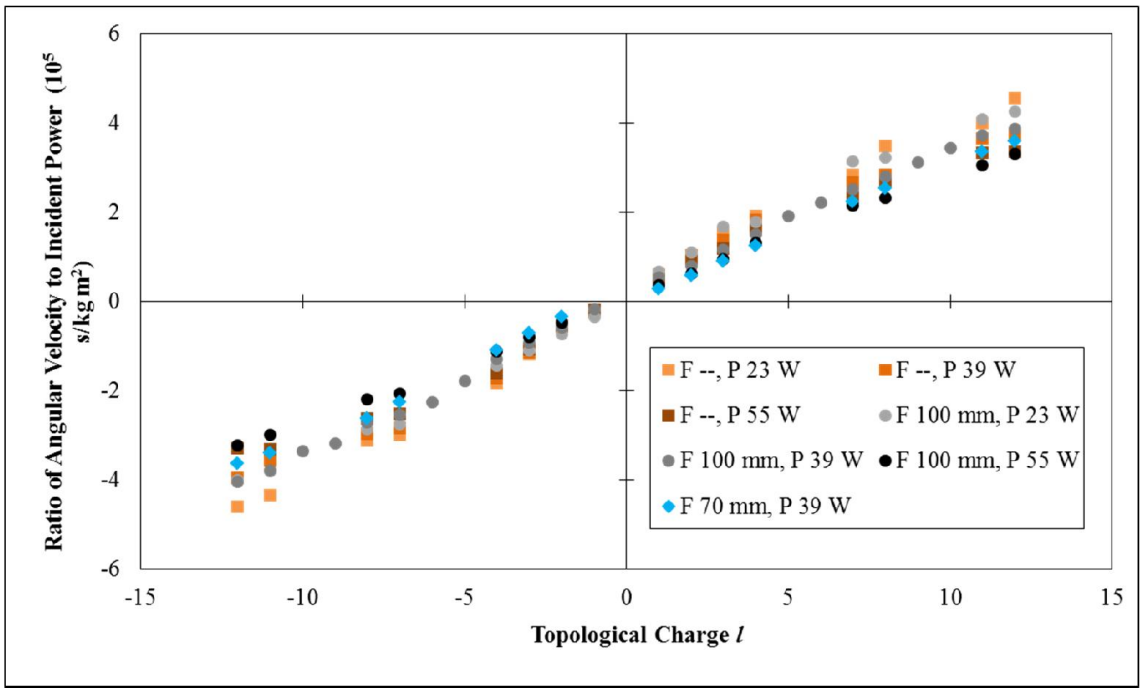

Figure 5-13 Ratio of measured torque to power incident on acoustic absorber times the angular velocity of acoustic beam, i.e. $\boldsymbol{\omega_A/(cF_z)} * \boldsymbol{2\pi f}$, from a range of helical ultrasonic beams focused at 70 mm, 100 mm or unfocused (indicated as F 70mm, F 100 mm and F --, respectively), with transmitted acoustic power of 23 W, 39 W and 55 W (indicated as P 23 W, P 39 W and P 55 W, respectively.

confirmed with both acoustic field simulation and hydrophone tests of the ultrasonic beam generated from the transducer array. Angular momentum transfer from the acoustic beam to the absorber was observed.

An increase in the levitation distance of the acoustic absorber with power was clearly detected, as expected, due to the increased axial acoustic radiation pressure. The trend of reduced levitation force, with increasing of l, was also observed, due to increased angular momentum component in the beam.

From the extracted angular velocity change of the acoustic absorber, we observed that

1. The terminal angular velocity at balanced state is linear to l at low order of topological charge.
2. Sign change of the topological charge in the beam phase profile would lead to the change in rotation direction, which proved that this rotation

effect is due to the angular momentum carried by the ultrasound beam, not asymmetry of the beam or system.

3. The terminal angular velocity is larger with higher acoustic power, as predicted.
4. Under the same condition, unfocused beams carry the most orbital angular momentum, beams which focus at 100 mm above transducer follow, then beams focus at 70 mm above transducer least.

Mathematics model of angular motion of the acoustic absorber was built and analysed. Reynolds number of the system was worked out to prove that this is a rotation with Stoke's drag with constant drag coefficient. By fitting all the data set to the acceleration process, the drag coefficient C was obtained. This coefficient was also confirmed by the Eq. (5-1), which is the 'golden ratio' of orbital angular momentum to energy in vortex beam and has been theoretically proven. This is the first time to confirm this ratio does stand.

The fine agreement of the results from those two models not just demonstrated the correctness of the predicted theory, but also proved the ability of the acoustic array as precise beam shaping instrument. Further acoustic demonstrations can be established with this apparatus.

Chapter 6
Negative Radiation Force in a Tractor Beam

Most object manipulation in optics and acoustics makes use of conservative forces, such as the potential wells formed by optical tweezers and acoustic standing waves. However there are also many interesting and useful forms of manipulation based upon non-conservative forces, dating back to the original optical trap formed using radiation pressure [172][173]. More recently, there has been wide interest in creating negative non-conservative force to, somewhat counter intuitively, pull a target towards the source, an arrangement that has come to be known as a tractor beam.

In this chapter, we used an ultrasonic phased array to create a 'negative' radiation force on prism target pulling them toward the array. This is the first demonstration of 1) negative radiation force with non-conservative force directed towards the energy source and 2) acoustic negative radiation pressure. Also because it is done with ultrasound, as discussed in last chapter, this is the first demonstration of negative radiation force with 3) a macroscopic target.

6.1 Background

Non-contact manipulation of objects is used for many practical uses. This includes optical [174] and ultrasonic trapping [81], [175]. Recently, there has been wide interest in using radiation force, in contrast to gradient force, to produce a 'negative' force, directed towards the energy source.

There have been many theoretical descriptions of whether or how a tractor beam could be realised, i.e. a beam with attractive force coming from radiation pressure instead of gradient force [176]–[180]. The first demonstration of a tractor beam was reported very recently last year in Nature Photonics [181], and it only worked with a mirror and without a net flow of momentum.

In this chapter, we use the same 1000-element ultrasound transducer array, the same on as in last chapter, to produce ultrasound beams which induce negative radiation force (NRF) in opposition to the net flow of momentum i.e. the propagation direction of the beam. Unlike utilizing absorption of acoustic wave by the absorber to transfer the momentum in last chapter, the energy is transferred to the target when reflected on metal surfaces.

6.1.1 Radiation Force vs. Gradient Force

As introduced in chapter 2, light carries linear momentum. If the photons are exerted onto an object and are reflected or absorbed, linear momentum will be transferred onto the object and give it momentum with the same direction as the original direction of the light beam. The force caused by this momentum transfer is called *radiation force*.

When the photons are refracted at the surface of the target due to a refractive index mismatch, the propagation direction of the light beam changes, momentum is also given to the target. However, if the light intensity is not even and, i.e. there is a gradient, then the light beam component with higher intensity will give a larger force whilst the lower intensity beam will contribute a smaller

force. This leads to a resultant force directed towards to the light intensity maxima in the light beam. Since this force is caused by the light intensity gradient in the beam, it is called the *gradient force*. Gradient forces exerted by a highly focused laser beam are employed in optical trapping systems (optical tweezers) to trap and move microscopic particles [55], [182].

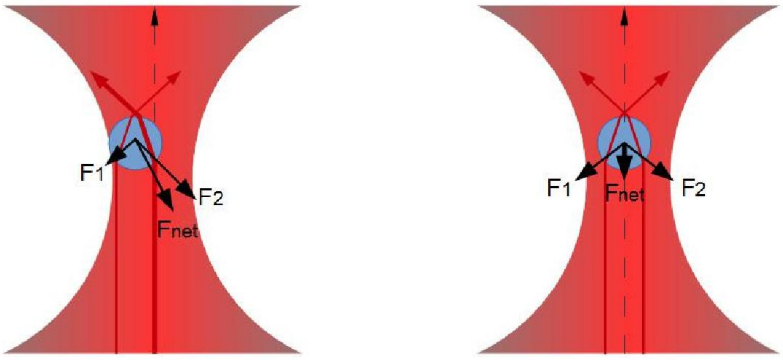

Figure 6-1 Gradient force in optical trapping

Distinguishing between a radiation force and a gradient force can be hard since they can both be caused by a changing in the beam propagation direction. However, the intensity gradient in the field is essential for gradient pressure whilst the radiation pressure is usually considered independent from intensity gradient. The other big distinction between them, as introduced in Chapter 2.9, is that the gradient force is a kind of conservative force, i.e. it is associated with the formation of a potential energy well, whilst radiation pressure is a non-conservative force.

Traditionally, methods for moving particles towards a light source use conservative forces, however using only non-conservative forces can have several benefits. Firstly, it eliminate the need for highly non-uniform fields with high intensity in a focused region. Secondly, the manipulation range can be extended significantly, potentially beyond the focal length in optical tweezing. This also means the possibility of manipulation large objects with optical forces.

6.1.2 Demonstration of Negative Radiation Pressure in Optics

At present, a number of proposals for attracting objects towards light sources have been raised and among them some have been demonstrated.

Optical tweezers systems is capable of applying force on microscopic targets towards the light source. Potential wells in trapping centre are moved to move the trapped particle accordingly.

Similar to Gaussian beam optical tweezing, there have been a number of other methods which employ non-diffracting beams for creating standing waves to move particles in the negative direction. Optical conveyor belts [183] provide trapping and delivery of submicron particles over hundreds of microns. They are based on a standing wave created from two counter-propagating non-diffracting Bessel beams, in which phase of one of the beams can be changed. The translation of the standing wave nodes and antinodes delivers micro-particles both along and opposite to the direction of light propagation to specific place. This two side orientation requires complete overlap of counter-propagating beams and is hard to realise. A one-sided variant of the optical conveyor belt created from coaxial Bessel beams has been demonstrated, but relies on auxiliary forces to achieve retrograde motion [184]. A one-side optical conveyors that does not require outside assistance was demonstrated [84]. Coherently superposing coaxial Bessel beams create a class of tractor beams. Those optical conveyors have periodic intensity maxima along the axes that act as optical traps. Trapped micro-objects are moved along the conveyor by selectively changing the Bessel beam's relative phase. Hence conveyor belt traps do not qualify as tractor beams under the definition whereby a non-conservative force is needed.

Another impressive demonstration of 'pulling' particle was achieved by interfering a set of Bessel beams, resulting in what was called a solenoid beam [185]. A single spiral intensity maximum was created to trap a particle. If the direction of the overall angular momentum of the beam is opposite to the spiral,

a part of the gradient force appears that acts in a direction opposite to the beam propagation. This setup was described as the optical analogue of the Archimedes' screw [186].

Those methods all make use of the potential wells within the optical fields. Either by moving the potential minima points or through interfering, forces employed are all in the catalogue of conservative forces.

There has been proposed that the material surrounding a particle serves not just to assist but in fact an essential element, for achieving negative motion. Some studies suggested that a light beam propagating in metamaterials, which refers to an artificial structure which has special optical properties and even negative refractive index over some frequency range, and incident on a reflecting body imparts onto it momentum directed towards the source of the radiation [187]–[189]. Metamaterials are also called left-hand materials. Unfortunately, at present, all the metamaterials presented are solid, hence a demonstration of particles moving in metamaterial is precluded.

There is another collection of demonstrations which employs negative thermophoresis to manipulate macroscopic objects. A particle with an unequal heat generation across its surface due to, for instance, lensing effects under laser illumination, can migrate towards the radiation source if its back side is warmer than its front. The first observation of negative photophoresis in liquid media was achieved with absorbing microdroplets in water [190]. Then clusters of highly absorbing carbon nanoparticles were trapped and manipulated in open air with a dual-vortex optical trap [191], [192]. Later on, the manipulation was expanded to provide transport of ~ 100 μm objects over a distance of the order of a meter with $\pm$ 10 μm accuracy [193]. In those cases, the presence of a surrounding gas or liquid media is critical for the generation of thermophoretic force while radiation distribution is not crucial.

The properties of the small particles such as shape and material composition can be tailored to modify scattering properties. For instance, anti-

reflection coated microspheres have a small radiation pressure cross-section and therefore experience a small positive radiation pressure. AR coated microspheres with high refractive index can be optically trapped with force up to nanonewton [194]. Because of momentum conservation, radiation pressure can also be dramatically reduced when particles scatter light strongly in the forwards direction [195], [196]. At more extreme cases, an active media can even increase the 'forward' momentum results from scattering and creates a negative force on the particles due to gain-induced momentum [197], [198]. However the using 'exotic' media strongly confines the possible applications of the negative force.

Stable optical lift [199] is able to give semi-cylindrical rods transverse force within uniform light stream. The rod in the uniform non-intensity-gradient light beam is able to self-rotate to a stable angle and exhibit uniform motion due to its differently shaped top and bottom surfaces. In this system, the transverse force is solely due to the geometry of the micro-rods and thus an intensity gradient is not required. However, since this system is only capable of generating a transverse force, the targets are impossible to move in the direction opposite to that of the incident beam.

Alternatively, and the most successfully to date, one can put less axial momentum in the beam. A simple, conceptual macroscopic example is the ordinary optical components such as lenses, as shown in Figure 6-2. For the un-collimated beam, the projection of the total photon momentum along the propagation direction is small. When it encounters a lens, a beam is refracted to the propagation direction and hence an attractive optical force is possible. This refraction-based concept can be extended to appropriately designed subwavelength spherical particles. A Bessel beam is used to pull varieties of spheres, such as polystyrene [179], a magnetodielectric [180] or a high-refractive-index dielectric [200], towards the optical source.

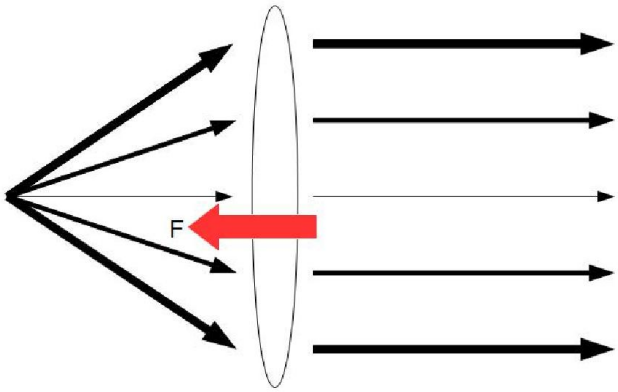

Figure 6-2 Reflection of the beam with less axial photon momentum by lens. Forward momentum on axis is enhanced so that the axial momentum of the emergent beam is larger than that of the incident beam.

Based on this principle of linear momentum conservation, Sukhov and Dogariu [178], [201] demonstrated that this negative radiation force can be generated on any scattering object with arbitrary shape by proper design of a non-axial light beam according to the target so that the beam is deflected parallel to the propagating axis.

In a very recent approach [181], a tailored optical beam incident on particles in the presence of a reflecting surface produced both gradient and radiation forces. The targeted particles reach an equilibrium position where significant gradient forces balance a radiation pressure that is towards the virtual source. Another demonstration has claimed the generation of forces acting against the flow of light with arbitrary objects and 'without resorting to non-paraxial illumination, interference of multiple beams, gain or other exotic materials' [202]. However the target has to be at the interface of two dielectric media to enable amplification of the photon momentum when the light is scattered from one medium into another with higher refractive index.

6.1.3 Demonstration of Negative Radiation Pressure with Sound

In part due to the similarities between light and sound waves, acoustic tweezers can perform many of the same function as optical tweezers for the purpose of trapping biological cells or other small objects. In fact an acoustic analogue to the optical schemes has also proposed for generating negative radiation pressure.

Acoustic standing waves, similar to optical standing waves, have been commonly applied in manipulation since more than 20 years ago. Two collimated focused ultrasonic beams (3.5 MHz) propagating along opposite directions were used to generate a stable force potential well to trap latex particles (270 μm diameter) and frog eggs. This potential well can move the trapped objects axially or laterally by moving one of the focusing transducers that generate the ultrasonic beams. These two collimated beams formed a standing wave at the paraxial region thus the axial movement can also be achieved by changing the frequency of the electrical voltage applied on the transducers [203].

Apart from acoustic standing waves, the counterpart of optical tweezers – the acoustic tweezing using a highly focused high frequency ultrasonic beam (100 MHz) with a Gaussian intensity distribution was investigated. It was demonstrated that, if the particle material and beam meet certain specifications, acoustic tweezing is possible, in both axial [204] and lateral [205] directions.

Martson [176], [206] predicted that, with an appropriate choice of frequency and Bessel beam parameters, a sphere which lies on the axis of an ideal acoustic Bessel beam can experience a radiation force directed towards the source. Rather than being based on counter-propagating sound beams in [203], his application only involve a single acoustic beam. His research became the foundation of acoustic pulling force investigation. Later, negative radiation forces on spheres with helicoidal Bessel beams were investigated [207]. The term ‘helicoidal’ refers

to acoustic vortex and having an axial amplitude null. The presence of axial amplitude null gives less axial pressure on spheres and thus it is more likely to produce radiation force directing opposite to the propagation direction of the beam, and negative forces only occurs when the scattering momentum backwards is suppressed relative to the scattering forward [177].

All the research on acoustic negative radiation pressure has, previous to this work, been done theoretically. Practical demonstrations are hard to realise due to the device limitation of creating the desired acoustic beam. In this chapter, a 1000-element ultrasound transducer array was used to produce ultrasound beams which induce negative radiation force in opposition to the propagation direction of the beam. Two macroscopic prism-shape targets were manufactured, and pulling forces on them were investigated. The production of pulling force without the presence of acoustic intensity gradient is confirmed.

6.2 Materials and Methods

6.2.1 Phase Configuration on Transducer Array

The ultrasound system and matrix transducer array used for this experiment is the same as in the last chapter. The array operates at 550 kHz (wavelength 2.7 mm in water) and the programmable system has independent control of the approximately 1000 elements in the 76-mm square aperture. The array control system drives the array elements, or a specified subset, with phases discretized to $\phi = n*\pi/4$, $0 \leq n \leq 7$, and eight discrete phases are required during operation.

The idea behind this demonstration is to create a set of acoustic beams with the 'Bessel beam' profile on one dimension, and constant phase and pressure distribution on another dimension. Hence it is what could be called a '2D Bessel beam profile', or what we call colloquially a 'Cross-Sabre beam'. Similar to a Bessel beam, the Cross-Sabre beam focuses at a rectangular–prism area, as shown

in Figure 6-3. The beam is reflected by the upper surface of a designed hollow prism, which is not shown in the figure, giving the prism a 'negative' force pointing to the energy source. To reduce the 'positive' pushing generated at the bottom surface of the prism, transducer elements in the centre were turned off.

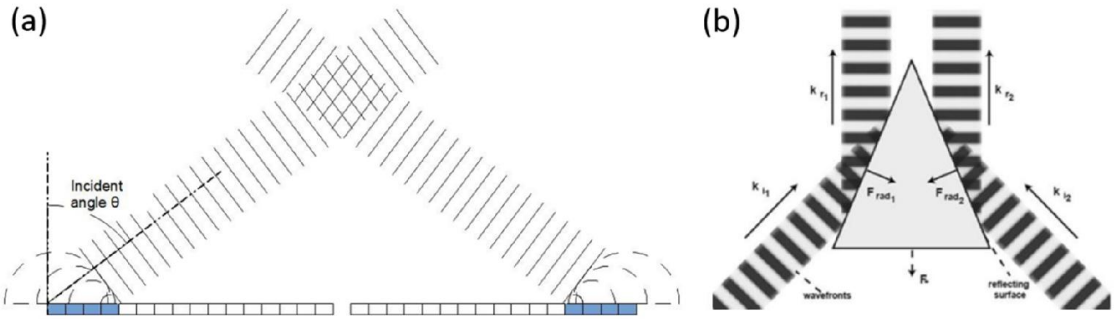

Figure 6-3 Cross-Sabre beam generation. (a) Generation of the acoustic beam without target above. (b) The acoustic wave is redirected by the prism-shape target and results in a negative radiation force.

To create such a beam, a four-element-wide (8.8 mm) rectangular active aperture on each side of the array was used, corresponding to eight rows of active elements, with all elements in a row having the same phase. Since the elements have only eight possible phase states, this dictates the possible steering angles, θ, to limit possibilities.

Using a phase offset between active apertures on either side of the array, each element has a phase for delays between n = 1 ~ 8 times π/4. The corresponding theoretical incident angle, referring to the angle between beam propagation direction and the normal to the transducer, to phase shift is shown in Figure 6-4. When n is small, the shallow incident angles will only graze the side of the target, and the force due to a change in direction of the beam will be minimal. When n is large, the focal zone will be close to the transducer array, thus limiting the useable distance above the array. For the present study, n = 5 for θ = 50.6° was chosen, which gives a high degree of directivity to the beam momentum. Hence a linear phase gradient of 5π/4 per element was applied to the active apertures.

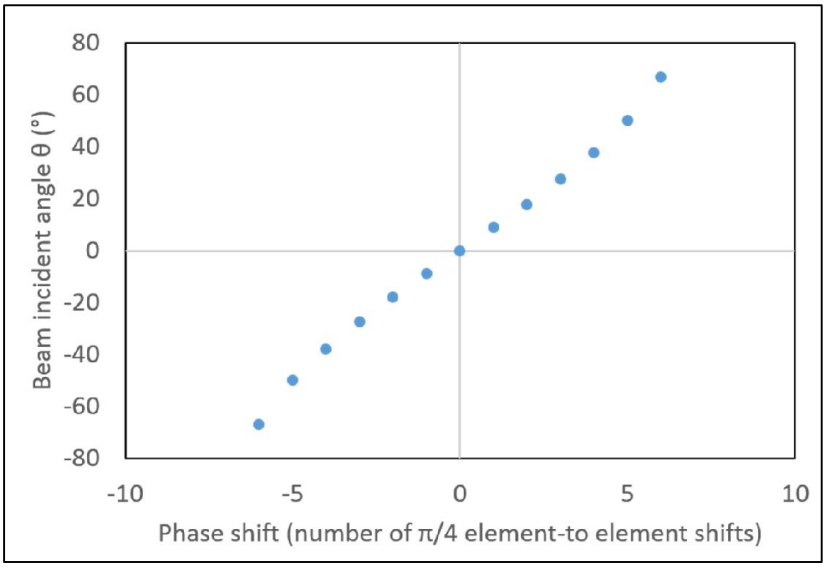

Figure 6-4 Beam incident angle corresponding to phase shift, calculated based on the possible phase shift between adjacent active elements.

Phase profiles with four lines of elements active are prepared and applied on ExAblate 2100 system, as shown in Figure 6-5. Phase gradient between neighbouring element-lines was $5\pi/4$ to create beam with incident angle of 50.6° towards the centreline. Due to the safety limits of the ExAblate system to avoid damaging the transducer array, phase profile with identical phase on both sides of the array cannot be performed. Hence a π radians offset between sides of the array was applied. This offset does not affect the measurements, which is confirmed by simulation (6.3.2), hydrophone test (6.3.3) and the Schlieren images (6.3.1).

The pair of active apertures were stepped towards the centreline, with interval of an element between each step. The steering angle and relative phase remain the same. The stepping in of the active region results in the wavefront intersection region moving closer to the source. This will be shown later in the simulation result Figure 6-10 in Simulation and Schlieren images in Figure 6-9 in Schlieren Imaging Result. As a consequence of the finite width of all sources, in this case, a finite numbers of elements, a Bessel-like beam will only retain its form over a finite propagation distance.

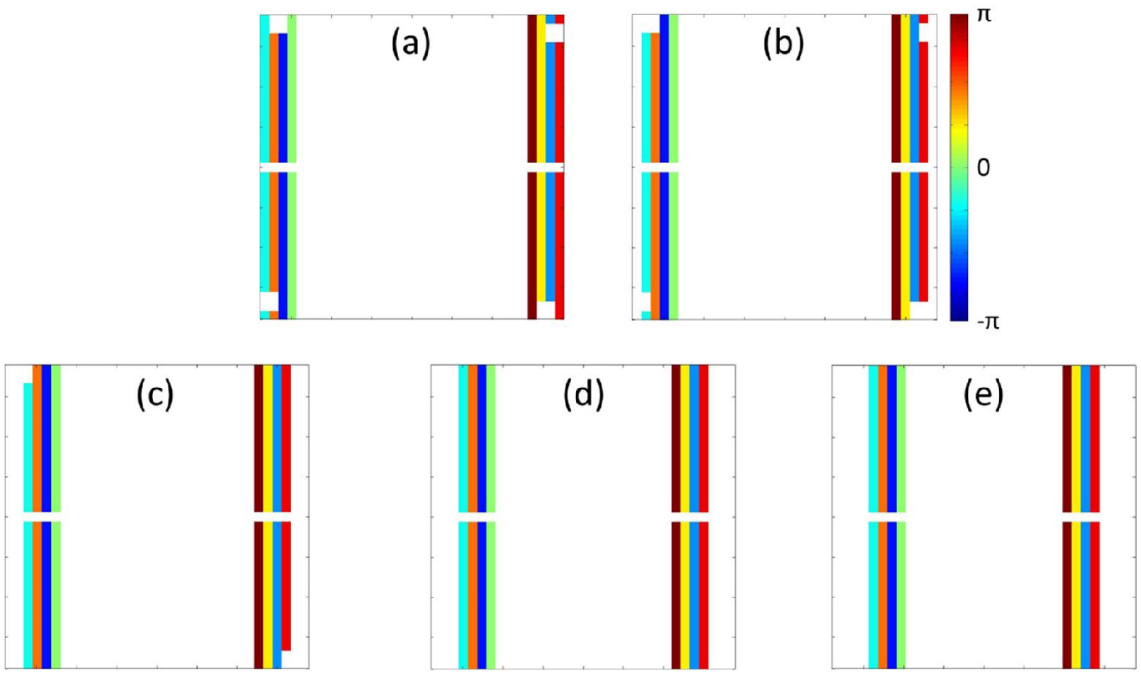

Figure 6-5 Applied phase files for generating Cross-Sabre beams (a ~ f) are corresponding to the aperture 1~5 respectively.

6.2.2 Target Geometry

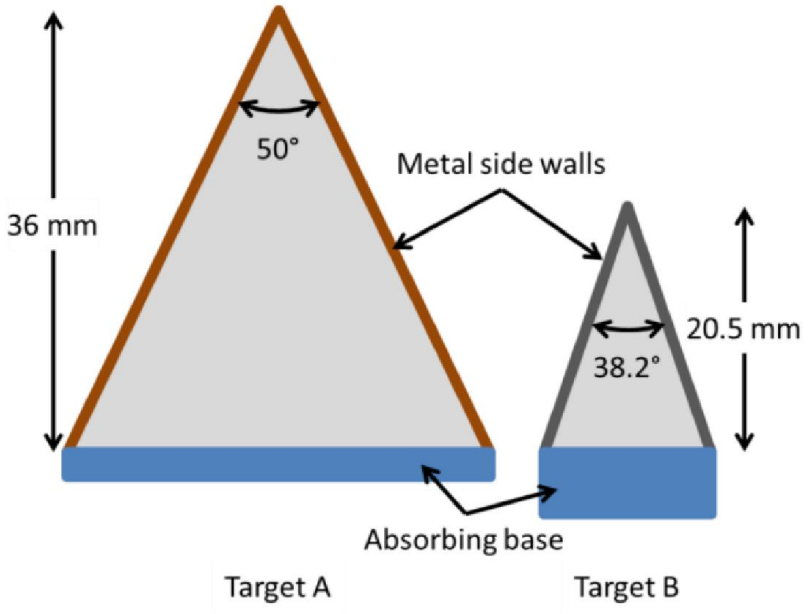

Figure 6-6 Dimensions of the targets used in the measurements. Sidewall of Target A and B is brass and stainless steel, respectively.

Two targets with different dimensions were designed for the negative radiation force measurements. The targets used in the experimental

measurements are hollow, sealed prisms with a layer of acoustically absorbing material (Aptflex F48, Precision Acoustics Ltd., Dorchester, UK) at the bottom.

The absorber is required to protect the source from large amplitude reflections. In addition, it can eliminate reflection at the base to further reduce pushing pressure on the base. The targets are filled with weight to make them close to negatively buoyant.

The targets used in the measurements are illustrated in Figure 6-6 and the geometry detailed in Table 6-1. The apex angle of target A was designed to fit the incident angle of the acoustic beam, so that at incident angle = 50° the acoustic beam was reflected straight up to maximum the negative radiation force. Both of the targets extend beyond the edge of the array aperture so that the target intersects the full extent of the transmitted ultrasound field along the y axis. For both targets, the metal sidewall thickness is much less than the wavelength at the system frequency.

Table 6-1 Geometry of targets used in negative radiation force measurements

	Target A	*Target B*
Apex angle	50°	38.2°
Prism height	36 mm	20.5 mm
Prism base	34 mm	14 mm
Target length	100 mm	76 mm
Sidewall material	Brass	Stainless Steel
Sidewall thickness	100 μm	150 μm
Absorbing Base Thickness	2 mm	5 mm

6.2.3 Experimental Setup

For the force experiment, the matrix array was placed at the base of a tank (1 × 1 × 1 m) filled with degassed water. The walls of the tank, including sides, bottom and top surface, were lined with acoustic absorber (Aptflex F28, Precision Acoustics LTD., Dorchester, UK) to minimum sound reflections. The triangle prism target was suspended by threads from a bar on a mass balance, and place

above the transducer. The target was filled with weights to make the target nearly negatively buoyant, so that the threads were always in tension and providing lifting force to the target.

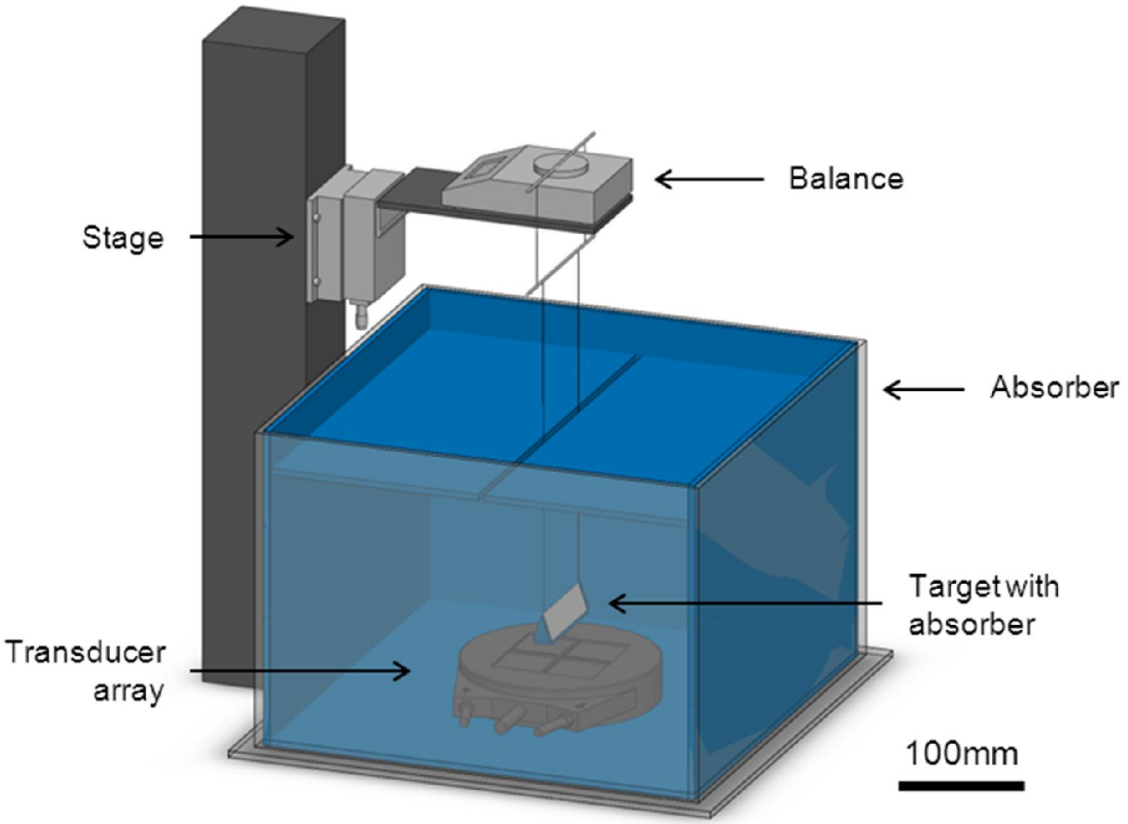

Figure 6-7 Experimental setup for measuring acoustic radiation force on the triangle prism target. Measurement of the force was achieved by suspending the triangle prism target with threads and a bar onto a mass balance on a platform which was attached to a translation stage and the stage was attached to a vertical optical rail on a mounting platform.

Measurement of the force was achieved by a mass balance with precision of 0.001 g. The mass balance was on a platform which was attached to a manual, micrometre actuator driven translation stage with 14 mm travel range (M-562-XYZ, Newport, US), and the stage was attached to a vertical optical rail (XT95-1000, Thorlabs, UK) via a mounting platform (XT95P11, Thorlabs, UK). This optical rail was fixed on an optical breadboard on which the water tank was placed. The initial position of the prism was with its bottom contacting the surface of the transducer array at a height Z = 0, then raised to each targeting

height Z_t, by raising the translation stage. When the range limit of the stage was reached, the stage, and connected balance and target, was repositioned on the optical rail with an increment of 14 mm. A video camera was placed above the balance to record the reading from the display panel.

The transducer array elements were driven with a continuous wave signal with pre-set phase profiles to generate the desired acoustic beam. The sonication lasts for 15 seconds so that the reading from the balance is stable before the sonication stops. Although the ExAblate 2100 system is capable of delivering up to 200 W acoustic power, the acoustic power we used for testing was limited to 23 W in order to protect the transducer array by limiting the reflection from the targeting base. In addition, the lowered power can also reduce the heat delivered to the target. Heat on the target would lead to a volume increase due to thermal expansion. The change of target volume would cause a change of buoyancy force on the target, thus affecting the accuracy of the force measurement. Between each sonication a sufficient length of time was left for the target to cool down. This could be monitored via the reading from the balance. The temperature rise of degassed water in the tank was negligible because of the large volume. Since the balance is very sensitive, slight perturbation in air can cause a large error of the result. A paper-board box was made and covered on the balance to eliminate the error due to air disturbance, which is not shown in Figure 6-7.

Each experiment was repeated three times and the force was averaged over three measurements.

6.2.4 Schlieren Setup

To visually observe the acoustic pressure created by the transducer, a Schlieren imaging setup was assembled.

Schlieren photography uses a collimated light beam to visualize the pressure variation in fluid. When a parallel beam goes through transparent media, it can be seen as a group of parallel ‘sub-rays’. If the media has uniform

refractive index, after passing the media, these rays would still be parallel and could be focused with a converging lens to a single point. However, if the media has pressure variation in it, some of the rays would change propagation direction and cannot be focused to the former point while some still can. Hence by putting a knife-edge at the focal point, some of the interacted rays would be blocked and causes darker pattern at the camera behind the focal point, while some rays would cause brighter pattern. Thus Schlieren imaging allows the visualization of refractive index variations (caused by intensity or pressure) within transparent media [208]. The most important point of Schlieren is using a sharp edge at focal point to block part of the rays, as shown in Figure 6-8.

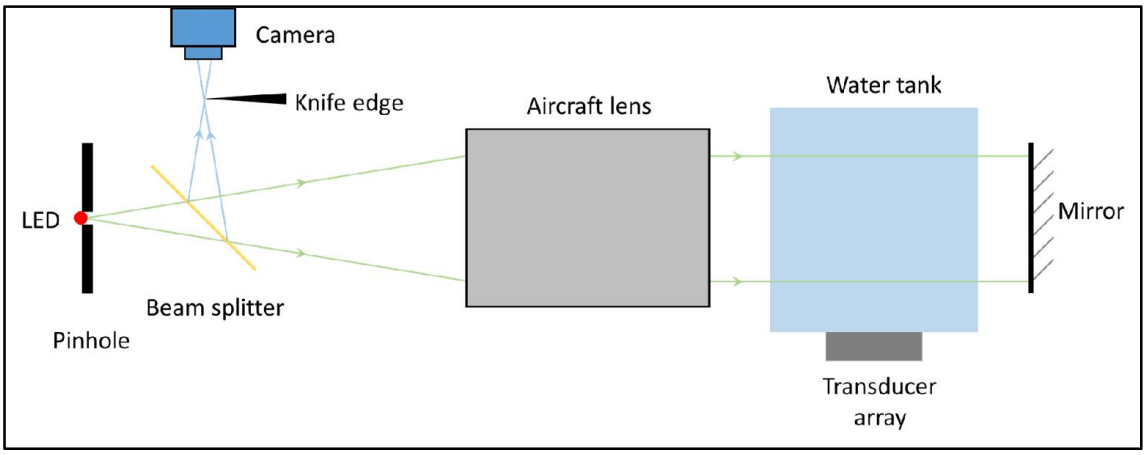

Figure 6-8 Schlieren imaging setup for visualization of the acoustic pressure distribution. A point light source is created with an ultra-bright LED and a pinhole. Diverging light is collimated with an aircraft lens onto the water tank. The beam is then reflected back with a 4 inch mirror hence beam goes through the tank twice, leading to the increment of contrast. A beam splitter reflects the beam to focus onto a knife-edge and then onto a camera

There are several ways to accomplish Schlieren imaging. The simplest setup is using a long-focal-length concave mirror and put both the point light source and the knife-edge at $2f$ away from the mirror with very small lateral interval, and the imaging target very close to the mirror, where f is the focal length of the concave mirror. The extra benefit of this setup is that the beam will be reflected by the mirror, thus it goes through the imaged target twice, enhancing the

imaging contrast. However since the illumination beam is not collimated when encounter imaging area, it is not suitable for imaging target with large volume.

The acoustic field needs to be imaged is 80 ×80 × 80 mm. Since this is a fairly large area, an old lens set (Diameter 150 mm, borrowed from Miles Padgett, University of Glasgow) originally from an aircraft camera was used to provide enough field of view. The setup is shown in Figure 6-8.

A red LED was used as a continuous light source in front of a pinhole aperture (around 200 microns, measured under bright-field microscope), to create a point light source. The size of the pinhole determines the quality of the light source, usually the smaller the better but not too small to cause diffraction, and should also still be able to provide enough light intensity. A diverging light beam is collimated by the aircraft lens and provides parallel illumination onto an optical transparent plastic box (300 × 300 × 300 mm) with a thin layer of acoustic transparent Mylar for its base. The ExAblate 2100 transducer array is under the transparent box to generate the acoustic beam. A four-inch flat mirror (100MC00, Comar optics, UK) is behind the plastic box to reflect the beam the same way back. Before the beam is focused back to the point light source, a beam splitter (BS016, 50:50, Thorlabs, USA) reflects the beam to focus onto a knife-edge and then onto a camera [EC1280, (1280 × 1024) pixel resolution, 6.7 μm per pixel, PROSILICA, Canada]. Similar to the common concave mirror imaging system, this setup benefits from enhanced contrast.

6.3 Results and Discussion

6.3.1 Schlieren Imaging Results

Cross-Sabre beam profiles with active elements moving towards centre of the array were applied to the acoustic array and Schlieren images were taken at each step. Figure 6-9 shows the pressure distribution within the acoustic field without the target object.

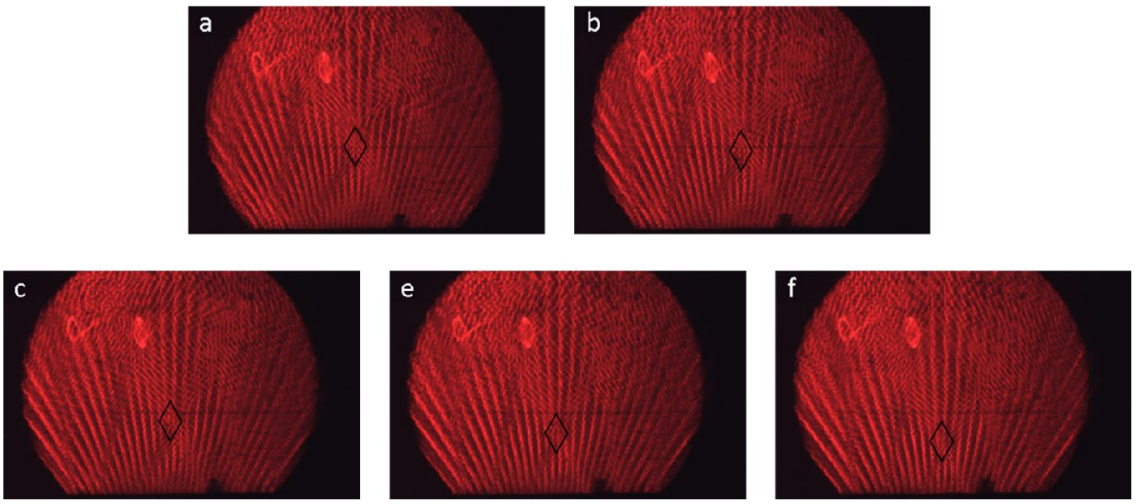

Figure 6-9 Schlieren images of the acoustic field with different phase profiles applied. (a-f) indicated step 1-5 respectively, i.e. with active elements moving from outside to inside. The black diamonds in the images indicate the focused regions of the acoustic beams.

Black diamonds on the graphs illustrate the location of the focused region of the Cross-Sabre beam. The results are coincident with hydrophone-measured acoustic fields and simulation. Figure 6-9.a is with elements at the rim active; in Figure 6-9.b active elements moved one step, i.e. one element, into the centre, , and so on. From the Schlieren images, we can clearly see that with the moving in of the active elements, the focused diamond area moves downwards. This can further validate the results we got.

6.3.2 Simulation

(Simulation of acoustic field in Matlab was done by Christine E. M. Démoré. Simulation of force in COMSOL was done by Peter Glynne-Jones).

The acoustic field distribution was simulated in Matlab based on a Fourier acoustics approach [163], with the geometry of the transducer array and applied phase profile. The transducer array was assumed to be working in an open free space filled with water.

Figure 6-10 shows the simulated acoustic pressure distribution with applied phase. From the results (Figure 6-10.b and Figure 6-10.d) we can see that the phase offset on either side of the array is not affecting the pressure of the acoustic

field. In addition, the diamond part we are interested in is moving towards the transducer array while the active elements step towards the centre of the array, as we expected.

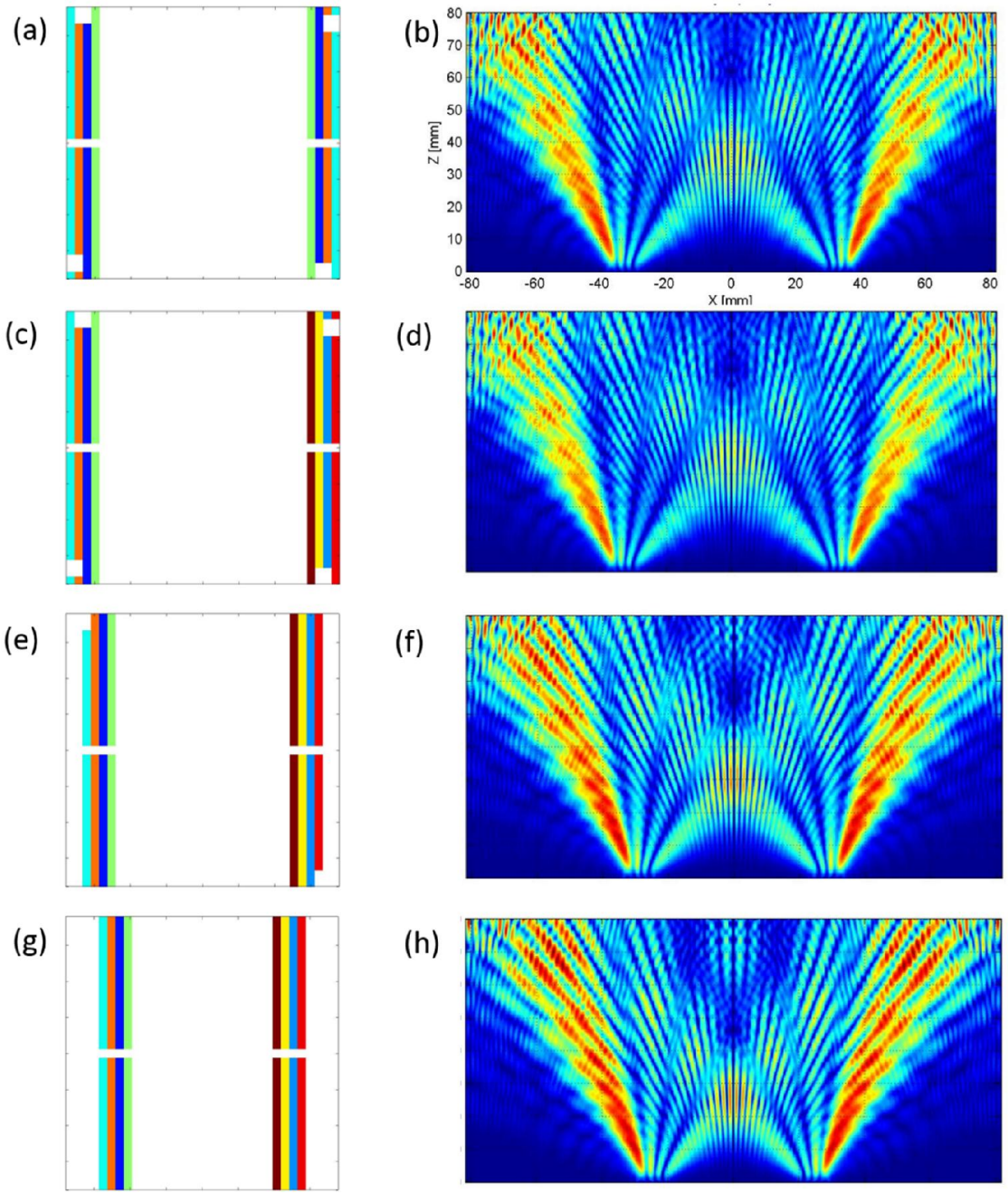

Figure 6-10 Simulated pressure distribution of Cross-Sabre beam. (a, b) Applied phase and simulated pressure of aperture 1. Phases applied on both side of the array are the same. (c, d) Applied phase and simulated pressure of aperture 1 but with phase offset of π. (e, f) Aperture 3 with phase offset. (g, h) Aperture 5 with phase offset.

Finite element analysis was used to predict the radiation force on the target, which includes the positive radiation force on the target base, F_+, the negative radiation force on the target sides, F_-, and the resultant force, F_{net}. The predicted radiation forces on the surfaces of the prism targets were calculated using a 2D harmonic, linear acoustic finite element model of the source and target (COMSOL 4.3a, Cambridge, UK) [209]. Given the shell construction of the targets, they were approximated as simple isosceles triangles, with reflecting boundary conditions for the sides and a radiation boundary condition for the absorbing base. The array elements were modelled as point sources, valid since the array elements are much less than 1λ wide and confirmed with directivity test (shown in Chapter 6.3.3), and the modelled domain surrounded by a perfectly matched layer (PML) to absorb energy incident on the boundaries. Since acoustic velocity is not zero at all faces of the target, it is necessary to take this movement into account when calculating the mean force on the boundary. Yosioka and Kawasima [210] showed that the net force is given (to second order) by the integral of the acoustic radiation stress tensor [211] over the mean position of the surface of the target, that is, the excess pressure on each of the target faces. Thus the time-averaged radiation force $\langle F_s \rangle$ on a section dA of the moving target can be written as:

$$\frac{\langle F_s \rangle}{dA} = \boldsymbol{n}(\langle V \rangle - \langle K \rangle) + \rho_0 \langle (\boldsymbol{n} \cdot \boldsymbol{u}_1)\boldsymbol{u}_1 \rangle, \qquad \text{Eq. (6-1)}$$

where $\langle V \rangle$ and $\langle K \rangle$ are the first order (i.e. linear) time averaged potential and kinetic acoustic energy densities respectively, ρ_0 the fluid density, $\boldsymbol{n}$ the surface normal and $\boldsymbol{u}_1$ the first order acoustic velocity vector. The vertical component, $\langle F_s \rangle \cdot \hat{z}$, was calculated for the target base, $\langle F_{side} \rangle$, and the symmetric sides of the triangle, $\langle F_{side} \rangle$ giving a net force, $\langle F_{net} \rangle$, on the target:

$$\langle F_{net} \rangle = \langle F_{base} \rangle \cdot \hat{z} + 2\langle F_{side} \rangle \cdot \hat{z} \qquad \text{Eq. (6-2)}$$

Predicted force profiles are shown in Figure 6-11.

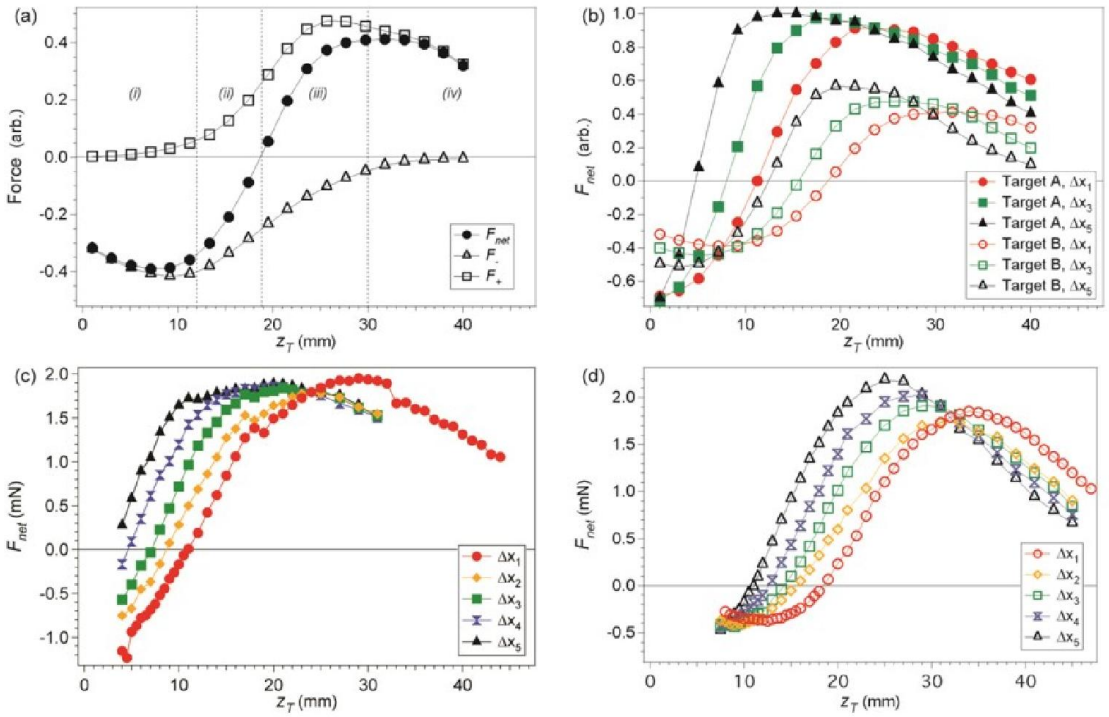

Figure 6-11 Axial map of radiation forces on prism-shaped targets in tractor beams, along with the experimental data for comparison. (a) Predicted normalized net force profile, F_{net}, on Target B by field transmitted from active sub-apertures with separation Δx_1. F_{net} is the sum of component vertical forces: positive radiation force, F_+, due to absorption on the base, and negative radiation force, F_-, from forward scattering at the target sides. Regions of interaction: (i) only the top of the target intersects the wavefronts and F_{net} is minimized when wavefronts are maximally incident on target sides; (ii) wavefronts intersect more of the base and less of the sides until F_+ balances F_-; (iii) wavefronts are primarily incident on the absorbing base, increasing then maximizing F_+; (iv) the target moves beyond the intersecting wavefronts and F_{net} decreases. (b) Predicted normalized net forces on Target A and Target B, with varying separation between active array sub-apertures, Δx_n. Measured net force on (c) target A and (d) target B showing the same trend as the predicted force. More information will be given in Chapter 6.3.4.

6.3.3 Hydrophone Test

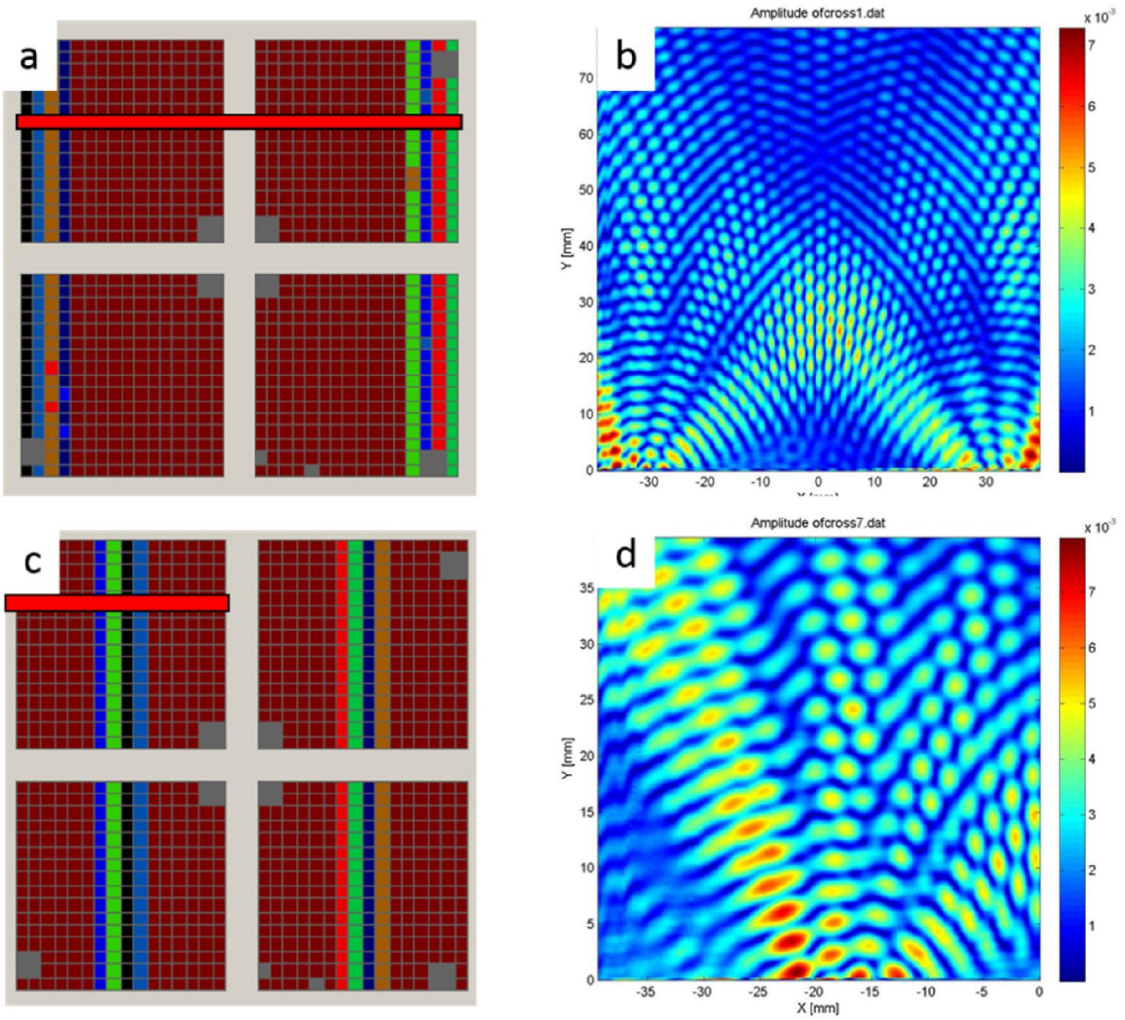

Figure 6-12 Hydrophone test of the acoustic field. (a, b) Full acoustic field measurement with elements at the rim on, area 80 * 80 mm. (c, d) half of the field in a smaller testing window, area 40 *40 mm. Red bars indicate scanned area.

The real ultrasound field was measured in a three-dimensional ($1 \times 1 \times 1$ m^3) scanning tank, with a calibrated needle hydrophone (200 μm Probe, Precision Acoustics, UK). The array was placed in the tank, facing a sidewall. Free-field profiles were generated, and subsequently used to validate the fields for the transducer located within the chamber. Different from last chapter which measured acoustic information in XY plane, the acoustic field in XZ plane was characterized. Because of the arrangement of the phase files applied, information

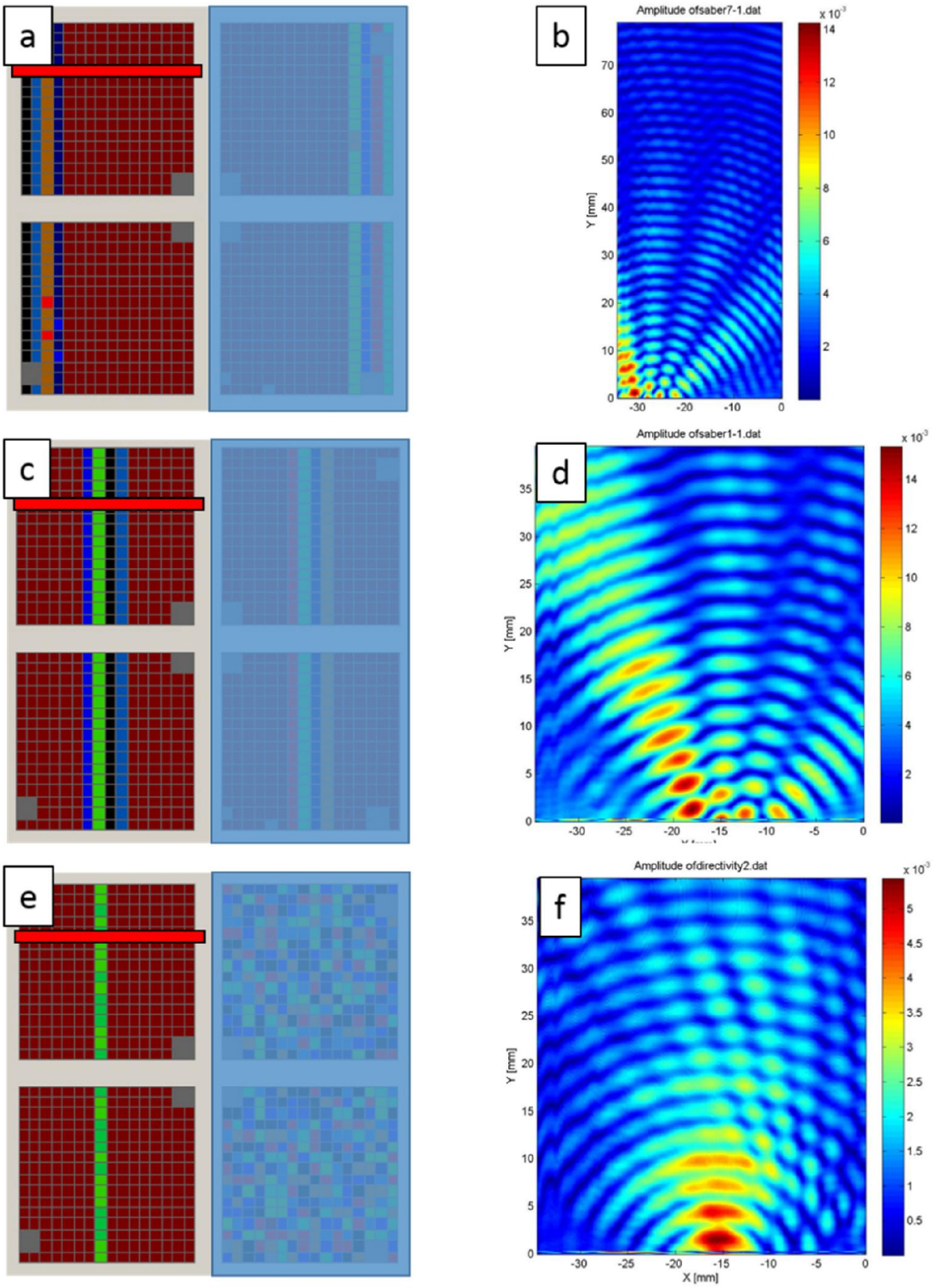

Figure 6-13 Hydrophone test of the acoustic field with half of the transducer array covered with acoustic absorber (effect as turned off). (a,b) Acoustic field when the rim of the array was active. Scanned area 40 * 80 mm. (c, d) Acoustic field when the elements at the centre were active. Scanned area 40 * 40 mm. (e, f) Acoustic field with only a line of the elements were turned on to show the directivity of the elements. Scanned area 40 * 40 mm. Red bars indicate scanned area.

along the Y axis is constant and field information along Z direction is more important.

Two phase profiles were applied to the ExAblate 2100 transducer array and the acoustic field was scanned at the XZ plane. As shown in Figure 6-12, when elements at the rim were active, interference of wave fronts constructed a diamond-shape focus at the centre. Moving activated elements into centre of the transducer produced similar field pattern with the focus area closer to the transducer array. The scanning result of (d) in Figure 6-12 showed the inference acoustic field.

In order to map the pressure distribution before interference of both sides of the array, another three test were carried out with half of the transducer array covered with acoustic absorber. The right half of the transducer array was not totally turned off because the safety restriction of the ExAblate system limits inactivated elements numbers.

Figure 6-13 shows the pressure distribution without interference with the other half of the array. Those results demonstrated good directivity of the elements and well-constructed beam profile.

6.3.4 Negative Radiation Force

1) Force variation during a single sonication

When the sonication starts, the acoustic energy generates not only a radiation force on the prism, but also causes it to heat up. Acoustic energy was absorbed by the target, especially at the bottom where it was coated with the acoustic absorber. The heating effect can be observed in the Schlieren imaging. The temperature rise on the prism leads to material expansion and causes further volume increase. Hence during a single sonication, the buoyancy on the prism increases with time.

Figure 6-14 shows the variation of the force from one sample, measured by the balance. Sonication started at t =2 s. An obvious negative force, with slight fluctuation which caused by the movement of the target, can be observed during the whole sonication. Negative force decreases with time as described before. When the sonication is finished at t = 17 s, the target got to its normal position and a positive force, which is increased buoyancy, can be observed. After sonication is finished, the target cooled down gradually by the water in tank, and the reading on balance went back to zero again.

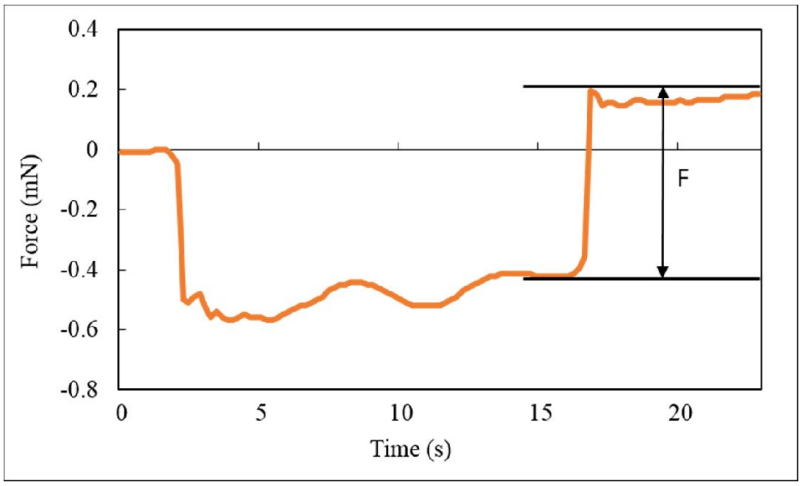

Figure 6-14 Balance reading variation with time during a single sonication. Force at the ending of sonication was used because it is smoother and would cause less error.

The negative radiation force can be extracted from the beginning or the end of the sonication. The force at the end of the sonication was used because it is smoother and would cause less error. Each data point was repeated three times and averaged to minimize error.

2) Radiation force on the target B

The radiation force on the target B with aperture 1 (Δx_1) is shown in Figure 6-15. The position of the target was defined as the distance between the base of the target (excluding the acoustic absorber) and the acoustic elements surface. Hence the minimum height of the target B can reach is 7 mm, which includes the height 5 mm of the absorber and the pitch on the transducer array which is 2 mm.

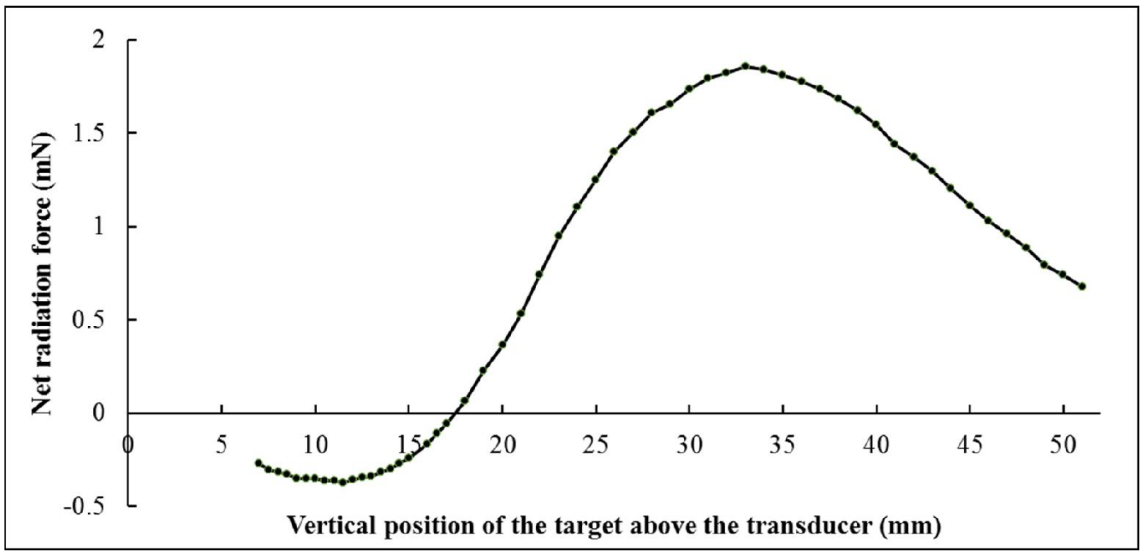

Figure 6-15 Radiation force on the target B along the vertical position. When the target is close to the array (small Z), the force is indeed negative. With the increment of Z, the ultrasound beam interacts more with the base of the targets, results in the pushing force.

When the target is close to the array (small Z), F_{net} is indeed negative, pulling the target towards the array because the steered wavefronts primarily interact with the side surface of the target. As Z increases, the wavefronts begin to interact more with the base of the target and less with the sides. Increased energy absorption at the base and reduced scattering force on the sides leads to the decrease in F_{net}, until F_+ and F_- are balanced. When Z is big enough, the wavefronts are incident primarily on the absorbing base, so F_{net} becomes positive, reaching a maximum upwards push when then base is at the highest intensity region of the field, before moving beyond the region of interference between the two crossing wavefronts.

Radiation force on the target B, with different apertures at various heights, is shown in Figure 6-16. As expected, reducing Δx has a similar effect to increasing Z_T, such that the region, measured from the source, over which F_{net} is negative, is shorter. With larger Δx, the maximum of $|F_{net}|$ reduces because of diverging and lower intensity fields farther from the source, and the position of the maximum in the negative radiation force is farther from the source. For both measured and predicted forces (Figure 6-11), the axial position, z_{T0}, at which

$F_{net} = 0$ increases linearly with Δx, corresponding to an axial shift in the interference field of the tractor beam. Differences between simulation and experiment can again be attributed to imperfect reflection and absorption by the targets. Above this position, the target is pushed away from the source, while below z_{T0}, it is continuously pulled towards the source.

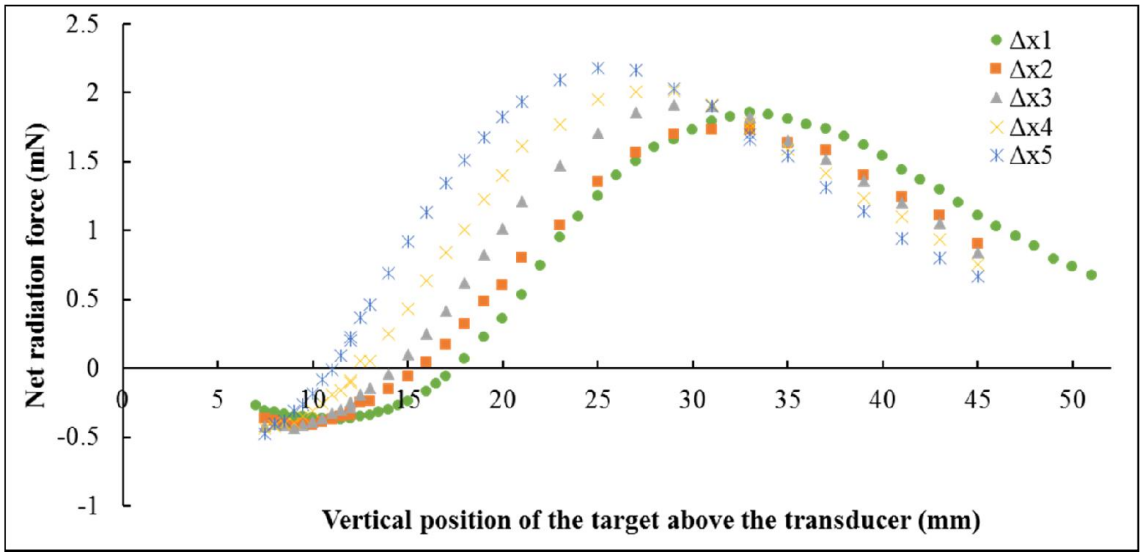

Figure 6-16 Radiation force on target B with different apertures at various heights. $\Delta x1$ has the largest distance between active elements while $\Delta x5$ refers to the smallest distance between active elements. Decreasing of the distance between active elements has a similar effect to moving the target away from the transducer, just as expected.

3) Radiation force on target A

The measurement of radiation force on the target A is shown on Figure 6-17. Unlike the result for target B, the force measurement for target A starts from 4mm due to the thinner absorber on the base. The results demonstrated that precise target geometry is not critical to the realization of the negative force, although a smaller target (target B) would allow more localized force measurement and profile mapping.

The wavefronts intersect the broader base of target A at a lower Z than target B, increasing the F_+ component, and consequently F_{net} is negative over a shorter distance from the source. However, the pulling force on the target A is

bigger, up to 1 mN, because of the larger surface area and optimized apex angle compared to the target B.

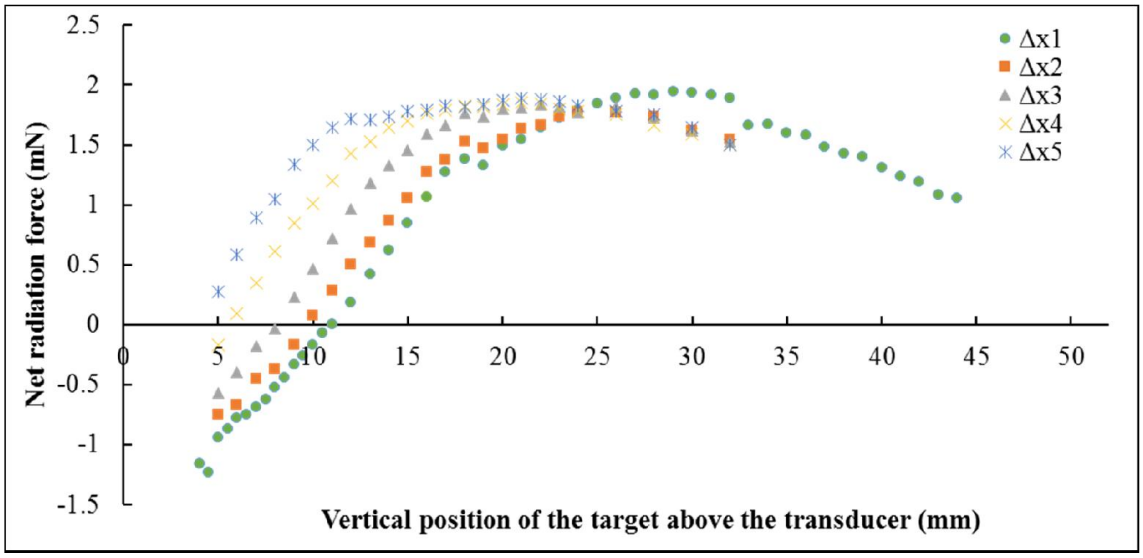

Figure 6-17 Radiation force on the target A along the vertical positions of the target. $\Delta x1$ has the largest distance between active elements while $\Delta x5$ refers to the smallest distance between active elements. A similar trend for the force to that with target B is observed. However, due to the bigger size of target A the negative radiation force region is smaller.

6.4 Conclusion

Negative radiation forces on objects, which arise from the reflection or scattering of locally off-axis wavefronts towards the beam axis, have been proposed for a range of particle trapping and manipulation applications using both optical and acoustic beams. We have provided clear visualization of the essential effects of these non-conservative attractive forces, and have used a very simple geometry to experimentally demonstrate negative acoustic radiation forces upon macroscopic objects.

In this experiment, the same ultrasound array source as last chapter was used to apply a controllable negative radiation pressure onto prism-shaped targets. The measured force profile confirms that the object is pulled towards the source even when the apex of the target intersects high intensity regions of the

beam, demonstrating that the force is due to non-conservative radiation pressure, not a conservative force due to gradients in the field. These results also indicate that these methods, in addition to other techniques, extend the dexterity of an ultrasonic matrix array to the point of having the ability to acoustically manipulate the position of matter in all directions, given the proper phasing and drive. Using the present wide ultrasonic array, negative radiation force has been observed for objects centred up to 18 mm away. This suggests that a source with a large aperture is required to manipulate distant objects but it will be possible to increase the net F– with more tightly collimated beams, or more complex propagating beam types.

Chapter 7
Discussion

With both propagating as waves, light and sound share many physical properties, such as reflection, refraction, scattering, diffraction, etc. The similarities between them enable us to translate our knowledge from one to the other, which is the key point of this thesis. Being different types of waves, the interaction of light and sound with different materials differs. Instead of a disadvantage, this actually brings us more opportunities to find the right tool for a certain application.

Modern optical imaging technologies employ fluorescent dyes [86] to enhance the contrast and the resolution of the images. However, to achieve this, the sample has to be prepared in advance. For living samples, introduction of the dye may have non-negligible effect on the behaviour of the sample [118]. These all make plain scattered light from the sample a good source of forming images, particularly when optical scattering and absorption of the sample is low.

In this thesis, a low-cost Light-Sheet Tomography imaging system was built for monitoring the growth of plant root. Because of the naturally low-density of scatterers in plant roots, optical scattering is very suitable for high resolution imaging the structure inside the roots. Shaping the illumination to form a light sheet with a simple cylindrical lens provides a number of benefits, including a simple optical setup, good axial resolution, very low light dose to the sample, fast

imaging speed and suitability for imaging relatively large 3D samples [47]. Since light sheet imaging technique gained its influence in the last ten years, it is playing an increasingly important role, especially for long-term monitoring development of large 3D samples [34], [102], [119]. Also, despite the resolution provided by scattered light from the plant root being not as high as in fluorescent imaging techniques, it is good enough for visualising the internal development of the roots, and simple enough to form a highly robust system. Potentially, it can be widely used for monitoring root development of other plant types when combined with model transparent soils.

Results have shown that LST is a promising tool for investigating root-soil interaction, even only with scattered light. Some improvement on performance of the imaging system would include integrating fluorescence imaging, further improving the resolution with structured illumination [139] and de-convolution [212], and extending the field of view with novel light sheet, such as Scanned Bessel and Airy light sheet [213]. Solely relaying on scattered light, this technique is therefore widely applicable to most other plant species. The simplicity and low cost of LST is also essential. In the future, portable instruments or stackable imaging system arrays could be developed using the same concept and applied in glasshouse screens.

Similarly, a light-sheet-illumination based photoacoustic imaging system is demonstrated. Employing light sheet illumination, similar to the good axial resolution in pure optical light sheet illumination imaging, provides good resolution in the Z axis because of optical sectioning feature. Hybrid imaging systems have shown that employing both optical and acoustic waves can be united; they do not have to serve independently as the form of an optical imaging system plus an ultrasound scanning system. Instead, the integration of them leads to high contrast due to optical absorption and deep penetration due to less acoustic scattering in photoacoustic imaging [3]. This also proves that it helps not

to take ultrasound and optics in isolation, but to have both in mind for addressing any solution.

Spatial light modulators allow the modulation of phase and/or amplitude of the light beam based on diffraction. SLMs can update the mask on the chip dynamically, hence have been used for aberration correction [22], adaptive optics [214], dynamic particle trapping [59], [215] etc. In short, SLMs can basically create arbitrary wavefront needed. We used a commercial 1000-element transducer array, essentially an analogue of SLM, as producer and modulator of the acoustic beam to create desired complex ultrasound beams.

There are several benefits to utilize ultrasound instead of light. The long wavelength of ultrasound makes it more suitable to interact with larger objects, and, the relatively high power of ultrasound array is able to provide more power in the beam, resulting in a larger force exerted on the objects.

With this transducer array, complex acoustic beams were generated, including acoustic helical beams with high topological charge up to $l = \pm 12$, comparing to the low-order ultrasonic vortex in [77] and [78]. Measurement of the sound field confirmed the accuracy of the beams. Those acoustic vortex beams were applied to a macro acoustic absorber to lift and rotate it through linear and angular momentum transfer. Based on the study of orbital angular momentum research in optics, the understanding in wave-matter interaction has been extended: for the first time, the ratio of angular momentum and linear momentum [148] in vortex is validated in a single experiment .

Apart from showing an experiment which are analogues of those in optics, novel ideas in ultrasound have been tested as well. With 1D Bessel-profile acoustic beams generated with the same transducer, negative radiation force toward the source of the beam was demonstrated. This is not just the first demonstration tractor beam with ultrasound, but the first time proper tractor beam (attraction towards source produced by a non-conservative force) is demonstrated in both optics and acoustics, and with macro objects.

The quantitative results achieved has clearly shown the accuracy of created beams, and this accuracy and control could enable us achieve more in ultrasound applications in the future.

Our use of a clinically approved ultrasound system opens up a range of potential medical and biosciences applications that may exploit tailored and complex ultrasound beams. By implementing the advanced control of ultrasound fields developed in experiments, there is significant potential for improving the control of energy deposition in focused ultrasound surgery and targeted drug delivery, in which high intensity beams are used to treat tumours noninvasively. Pushing, rotating and negative radiation forces might be used for *in vivo* manipulation and stimulation of objects, fluids or biological tissue, yielding novel diagnostic techniques and treatment options (e.g. drug delivery and activation). These potential applications will benefit from the larger forces possible with ultrasound, due to the longer wavelength, and are not constrained to the simple target geometry used here. Greater depth penetration is also provided relative to optical methods, up to several centimetres with the current ultrasound system. These results provide additional momentum for developing tailored ultrasound fields for both microscopic and macroscopic manipulation.

Bibliography

[1] K. Scholle, S. Lamrini, P. Koopmann, and P. Fuhrberg, "2 μm Laser Sources and Their Possible Applications," in *Frontiers in Guided Wave Optics and Optoelectronics*, 2010.

[2] F. A. Jenkins and F. E. White, *Fundamentals of optics*, Fourth. McGraw-Hill Book Co, 1957, p. 467.

[3] M. Xu and L. V Wang, "Photoacoustic imaging in biomedicine," *Rev. Sci. Instrum.*, vol. 77, no. 4, p. 41101, 2006.

[4] P. N. T. Wells, "Ultrasonic imaging of the human body," *Reports Prog. Phys.*, vol. 62, no. 5, pp. 671–722, May 1999.

[5] F. A. Duck, *Physical Properties of Tissues*. Elsevier, 1990.

[6] L. E. Kinsler, A. R. Frey, A. B. Coppens, and J. V Sanders, "Fundamentals of acoustics," *Fundam. Acoust. 4th Ed. by Lawrence E. Kinsler, Austin R. Frey, Alan B. Coppens, James V. Sanders, pp. 560. ISBN 0-471-84789-5. Wiley-VCH, December 1999.*, vol. 1, 1999.

[7] R. P. Feynman, R. B. Leighton, and M. L. Sands, *The Feynman Lectures on Physics: Mainly Mechanism, Radiation and Heat*. Addison Wesley, 1963.

[8] S.-C. Chu, Y.-T. Chen, K.-F. Tsai, and K. Otsuka, "Generation of high-order Hermite-Gaussian modes in end-pumped solid-state lasers for square vortex array laser beam generation.," *Opt. Express*, vol. 20, no. 7, pp. 7128–41, Mar. 2012.

[9] N. B. Simpson, K. Dholakia, L. Allen, and M. J. Padgett, "Mechanical equivalence of spin and orbital angular momentum of light: an optical spanner," *Opt. Lett.*, vol. 22, no. 1, pp. 52–54, 1997.

[10] J. M. Enoch, "History of mirrors dating back 8000 years.," *Optom. Vis. Sci.*, vol. 83, no. 10, pp. 775–81, Oct. 2006.

[11] F. Quercioli, "Fundamentals of optical microscopy," in *Optical Fluorescence Microscopy*, Springer, 2011, pp. 1–36.

[12] K. B. Wolf and G. Krotzsch, "Geometry and dynamics in refracting systems," *Eur. J. Phys.*, vol. 16, no. 1, p. 14, 1995.

[13] D. A. Goss, "Renaissance Vision from Spectacles to Telescopes," *Optom. Vis. Sci.*, vol. 85, no. 7, pp. 505–506, Jul. 2008.

[14] M. W. Beijersbergen, R. P. C. Coerwinkel, M. Kristensen, and J. P. Woerdman, "Helical-wavefront laser beams produced with a spiral phaseplate," *Opt. Commun.*, vol. 112, no. 5, pp. 321–327, 1994.

[15] J. Courtial, K. Dholakia, D. A. Robertson, L. Allen, and M. J. Padgett, "Measurement of the rotational frequency shift imparted to a rotating light beam possessing orbital angular momentum," *Phys. Rev. Lett.*, vol. 80, no. 15, p. 3217, 1998.

[16] V. Garcés-Chávez, D. McGloin, H. Melville, W. Sibbett, and K. Dholakia, "Simultaneous micromanipulation in multiple planes using a self-reconstructing light beam.," *Nature*, vol. 419, no. 6903, pp. 145–7, Sep. 2002.

[17] D. G. Grier, "A revolution in optical manipulation," *Nature*, vol. 424, no. 6950, pp. 810–816, 2003.

[18] T. A. Planchon, L. Gao, D. E. Milkie, M. W. Davidson, J. A. Galbraith, C. G. Galbraith, and E. Betzig, "Rapid three-dimensional isotropic imaging of living cells using Bessel beam plane illumination.," *Nat. Methods*, vol. 8, no. 5, pp. 417–23, May 2011.

[19] D. Faklis and G. M. Morris, "Spectral properties of multiorder diffractive lenses," *Appl. Opt.*, vol. 34, no. 14, pp. 2462–2468, 1995.

[20] P. Hariharan, *Basics of holography*. Cambridge University Press, 2002.

[21] K. D. Wulff, D. G. Cole, R. L. Clark, R. Dileonardo, J. Leach, J. Cooper, G. Gibson, and M. J. Padgett, "Aberration correction in holographic optical tweezers.," *Opt. Express*, vol. 14, no. 9, pp. 4170–5, May 2006.

[22] H. I. C. Dalgarno, T. Čižmár, T. Vettenburg, J. Nylk, F. J. Gunn-Moore, and K. Dholakia, "Wavefront corrected light sheet microscopy in turbid media," *Appl. Phys. Lett.*, vol. 100, no. 19, p. 191108, 2012.

[23] G. Sinclair, P. Jordan, J. Leach, M. J. Padgett, and J. Cooper, "Defining the trapping limits of holographical optical tweezers," *J. Mod. Opt.*, vol. 51, no. 3, pp. 409–414, Feb. 2004.

[24] T. Čižmár, M. Mazilu, and K. Dholakia, "In situ wavefront correction and its application to micromanipulation," *Nat. Photonics*, vol. 4, no. 6, pp. 388–394, May 2010.

[25] D. McGloin, G. Spalding, H. Melville, W. Sibbett, and K. Dholakia, "Applications of spatial light modulators in atom optics," *Opt. Express*, vol. 11, no. 2, p. 158, Jan. 2003.

[26] M. O. Ko¨hler, C. Mougenot, B. Quesson, J. Enholm, B. Le Bail, C. Laurent, C. T. W. Moonen, and G. J. Ehnholm, "Volumetric HIFU ablation under 3D guidance of rapid MRI thermometry," *Med. Phys.*, vol. 36, no. 8, p. 3521, 2009.

[27] S. L. Ehrlich, "Spherical acoustic transducer." Google Patents, 1973.

[28] E. Belcher and D. Lynn, "Beamforming and imaging with acoustic lenses in small, high-frequency sonars," *Ocean. MTS/IEEE. …*, pp. 1495–1499, 1999.

[29] D. J. Coleman, R. H. Silverman, A. Chabi, M. J. Rondeau, K. K. Shung, J. Cannata, and H. Lincoff, "High-resolution ultrasonic imaging of the posterior segment.," *Ophthalmology*, vol. 111, no. 7, pp. 1344–51, Jul. 2004.

[30] K. Thomenius, "Evolution of ultrasound beamformers," *Ultrason. Symp. 1996. Proceedings., …*, pp. 1615–1622, 1996.

[31] V. S. Dogra, B. K. Chinni, K. S. Valluru, J. V Joseph, A. Ghazi, J. L. Yao, K. Evans, E. M. Messing, and N. A. Rao, "Multispectral Photoacoustic Imaging of Prostate Cancer: Preliminary Ex-vivo Results.," *J. Clin. Imaging Sci.*, vol. 3, p. 41, Jan. 2013.

[32] S. te L. H. Frans J.M. Harren, Gina Cotti, Jos Oomens, "Photoacoustic Spectroscopy in Trace Gas Monitoring," in *Encyclopedia of Analytical Chemistry*, 2000, pp. 2203–2226.

[33] C. B. Scruby and L. E. Drain, *Laser ultrasonics: Techniques and applications*. 1990, p. 447.

[34] P. J. Keller, A. D. Schmidt, J. Wittbrodt, and E. H. K. Stelzer, "Reconstruction of Zebrafish Early Embryonic Development by Scanned Light Sheet Microscopy," *Science (80-.).*, vol. 322, no. November, pp. 1065–1069, 2008.

[35] F. W. Sears, M. W. Zemansky, and H. D. Young, *University physics*. Addison-Wesley Reading, UK, 1982.

[36] F. N. Egerton, "A history of the ecological sciences, part 19: Leeuwenhoek's microscopic natural history," *Bull. Ecol. Soc. Am.*, vol. 87, no. 1, pp. 47–58, 2006.

[37] A. Walther, "Irreducible aberrations of a lens used for a range of magnifications," *JOSA A*, vol. 6, no. 3, pp. 415–422, 1989.

[38] E. Abbe, "Beiträge zur Theorie des Mikroskops und der mikroskopischen Wahrnehmung," *Arch. für Mikroskopische Anat.*, vol. 9, no. 1, pp. 413–418, Dec. 1873.

[39] T. Mappes, N. Jahr, A. Csaki, N. Vogler, J. Popp, and W. Fritzsche, "The invention of immersion ultramicroscopy in 1912-the birth of nanotechnology?," *Angew. Chem. Int. Ed. Engl.*, vol. 51, no. 45, pp. 11208–12, Nov. 2012.

[40] G. Shtengel, J. A. Galbraith, C. G. Galbraith, J. Lippincott-Schwartz, J. M. Gillette, S. Manley, R. Sougrat, C. M. Waterman, P. Kanchanawong, M. W. Davidson, and others, "Interferometric fluorescent super-resolution microscopy resolves 3D cellular ultrastructure," *Proc. Natl. Acad. Sci.*, vol. 106, no. 9, pp. 3125–3130, 2009.

[41] K. I. Mortensen, L. S. Churchman, J. A. Spudich, and H. Flyvbjerg, "Optimized localization analysis for single-molecule tracking and super-resolution microscopy," *Nat. Methods*, vol. 7, no. 5, pp. 377–381, 2010.

[42] V. Westphal, S. O. Rizzoli, M. A. Lauterbach, D. Kamin, R. Jahn, and S. W. Hell, "Video-rate far-field optical nanoscopy dissects synaptic vesicle movement," *Science (80-.).*, vol. 320, no. 5873, pp. 246–249, 2008.

[43] M. Minsky, "Microscopy Apparatus: US 3,013,467." .

[44] A. Nakano, "Spinning-disk Confocal Microscopy — A Cutting-Edge Tool for Imaging of Membrane Traffic," *Cell Struct. Funct.*, vol. 27, no. 5, pp. 349–355, 2002.

[45] W. Denk, J. H. Strickler, and W. W. Webb, "Two-photon laser scanning fluorescence microscopy," *Science (80-.).*, vol. 248, no. 4951, pp. 73–76, 1990.

[46] C. Holzner, M. Feser, S. Vogt, B. Hornberger, S. B. Baines, and C. Jacobsen, "Zernike phase contrast in scanning microscopy with X-rays," *Nat. Phys.*, vol. 6, no. 11, pp. 883–887, Sep. 2010.

[47] J. Huisken, J. Swoger, F. Del Bene, J. Wittbrodt, and E. H. K. Stelzer, "Optical sectioning deep inside live embryos by selective plane illumination microscopy.," *Science*, vol. 305, no. 5686, pp. 1007–9, Aug. 2004.

[48] D. Wildanger, B. R. Patton, H. Schill, L. Marseglia, J. P. Hadden, S. Knauer, A. Schönle, J. G. Rarity, J. L. O'Brien, S. W. Hell, and J. M. Smith, "Solid immersion facilitates fluorescence microscopy with nanometer resolution and sub-ångström emitter localization.," *Adv. Mater.*, vol. 24, no. 44, pp. OP309–13, Nov. 2012.

[49] T. A. Klar, S. Jakobs, M. Dyba, A. Egner, and S. W. Hell, "Fluorescence microscopy with diffraction resolution barrier broken by stimulated emission," *Proc. Natl. Acad. Sci.*, vol. 97, no. 15, pp. 8206–8210, 2000.

[50] P. J. Keller, A. D. Schmidt, A. Santella, K. Khairy, Z. Bao, J. Wittbrodt, and E. H. K. Stelzer, "Fast, high-contrast imaging of animal development with scanned light sheet-based structured-illumination microscopy.," *Nat. Methods*, vol. 7, no. 8, pp. 637–642, Jul. 2010.

[51] C. Pavlin, K. Harasiewicz, M. D. Sherar, and F. S. Foster, "Clinical use of ultrasound biomicroscopy.," *Ophthalmology*, vol. 98, no. 3, pp. 287–295, 1991.

[52] K. H. Song, G. Stoica, and L. V Wang, "In vivo three-dimensional photoacoustic tomography of a whole mouse head," *Opt. Lett.*, vol. 31, no. 16, pp. 2453–2455, 2006.

[53] D. McGloin, "Optical tweezers: 20 years on.," *Philos. Trans. A. Math. Phys. Eng. Sci.*, vol. 364, no. 1849, pp. 3521–37, Dec. 2006.

[54] P. Lebedev, "The experimental study of the pressure of the light," *Ann. Phys*, vol. 6, p. 433, 1901.

[55] A. Ashkin, J. M. Dziedzic, J. E. Bjorkholm, and S. Chu, "Observation of a single-beam gradient force optical trap for dielectric particles," *Opt. Lett.*, vol. 11, no. 5, pp. 288–290, 1986.

[56] V. Y. Bazhenov, M. V Vasnetsov, and M. S. Soskin, "Laser beams with screw dislocations in their wavefronts," *Jetp Lett*, vol. 52, no. 8, pp. 429–431, 1990.

[57] M. S. Soskin, V. N. Gorshkov, M. V Vasnetsov, J. T. Malos, and N. R. Heckenberg, "Topological charge and angular momentum of light beams carrying optical vortices," *Phys. Rev. A*, vol. 56, no. 5, p. 4064, 1997.

[58] H. He, M. E. J. Friese, N. R. Heckenberg, and H. Rubinsztein-Dunlop, "Direct observation of transfer of angular momentum to absorptive particles from a laser beam with a phase singularity," *Phys. Rev. Lett.*, vol. 75, no. 5, p. 826, 1995.

[59] E. R. Dufresne, G. C. Spalding, M. T. Dearing, S. A. Sheets, and D. G. Grier, "Computer-generated holographic optical tweezer arrays," *Rev. Sci. Instrum.*, vol. 72, no. 3, pp. 1810–1816, 2001.

[60] J. E. Curtis, B. A. Koss, and D. G. Grier, "Dynamic holographic optical tweezers," *Opt. Commun.*, vol. 207, no. 1, pp. 169–175, 2002.

[61] E. Benes, M. Groschl, H. Nowotny, F. Trampler, T. Keijzer, H. Bohm, S. Radel, L. Gherardini, J. J. Hawkes, R. Konig, and others, "Ultrasonic separation of suspended particles," in *Ultrasonics Symposium, 2001 IEEE*, 2001, vol. 1, pp. 649–659.

[62] T. G. Wang and C. P. Lee, "Radiation pressure and acoustic levitation," *Nonlinear Acoust.*, pp. 177–205, 1998.

[63] A. Kundt and O. Lehmann, "Longitudinal vibrations and acoustic figures in cylindrical columns of liquids," *Ann. der Phys. und Chemie (Poggendorff's Ann.*, vol. 153, no. 1874, pp. 1–12, 1874.

[64] Lord Rayleigh, "XXXIV. On the pressure of vibrations," *London, Edinburgh, Dublin Philos. Mag. J. Sci.*, vol. 3, no. 15, pp. 338–346, 1902.

[65] H. Hatano, Y. Kanai, Y. Ikegami, T. Fujii, and K. Saito, "Fundamental study on ultrasonic levitation and its application to material processing in space," *J. Acoust. Soc. Jpn.(J)*, vol. 47, pp. 40–47, 1991.

[66] M. Takeuchi and K. Yamanouchi, "Ultrasonic micromanipulation of small particles in liquid," *Jpn. J. Appl. Phys.*, vol. 33, no. part 1, pp. 3045–3047, 1994.

[67] T. Kozuka, T. Tuziuti, H. Mitome, and T. Fukuda, "Acoustic manipulation of micro objects using an ultrasonic standing wave," in *Micro Machine and Human Science, 1994. Proceedings., 1994 5th International Symposium on*, 1994, p. 83.

[68] W. J. Xie and B. Wei, "Parametric study of single-axis acoustic levitation," *Appl. Phys. Lett.*, vol. 79, no. 6, pp. 881–883, 2001.

[69] E. H. Brandt, "Acoustic physics: Suspended by sound," *Nature*, vol. 413, no. 6855, pp. 474–475, 2001.

[70] M. S. Limaye, J. J. Hawkes, and W. T. Coakley, "Ultrasonic standing wave removal of microorganisms from suspension in small batch systems," *J. Microbiol. Methods*, vol. 27, no. 2, pp. 211–220, 1996.

[71] T. Laurell, F. Petersson, and A. Nilsson, "Chip integrated strategies for acoustic separation and manipulation of cells and particles," *Chem. Soc. Rev.*, vol. 36, no. 3, pp. 492–506, 2007.

[72] A. Nilsson, F. Petersson, H. Jönsson, and T. Laurell, "Acoustic control of suspended particles in micro fluidic chips.," *Lab Chip*, vol. 4, no. 2, pp. 131–5, Apr. 2004.

[73] L. V King, "On the acoustic radiation pressure on spheres," *Proc. R. Soc. London. Ser. A-Mathematical Phys. Sci.*, vol. 147, no. 861, pp. 212–240, 1934.

[74] J. J. Hawkes, W. T. Coakley, M. Gröschl, E. Benes, S. Armstrong, P. J. Tasker, and H. Nowotny, "Single half-wavelength ultrasonic particle filter: Predictions of the transfer matrix multilayer resonator model and experimental filtration results," *J. Acoust. Soc. Am.*, vol. 111, p. 1259, 2002.

[75] J. Hu, C. Tay, Y. Cai, and J. Du, "Controlled rotation of sound-trapped small particles by an acoustic needle," *Appl. Phys. Lett.*, vol. 87, no. 9, p. 094104, 2005.

[76] T. Wang, H. Kanber, and I. Rudnick, "First-order torques and solid-body spinning velocities in intense sound fields," *Phys. Rev. Lett.*, vol. 38, no. 3, pp. 38–40, 1977.

[77] K. Volke-Sepúlveda, A. O. Santillán, and R. R. Boullosa, "Transfer of Angular Momentum to Matter from Acoustical Vortices in Free Space," *Phys. Rev. Lett.*, vol. 100, no. 2, pp. 2–5, Jan. 2008.

[78] K. D. Skeldon, C. Wilson, M. Edgar, and M. J. Padgett, "An acoustic spanner and its associated rotational Doppler shift," *New J. Phys.*, vol. 10, no. 1, p. 013018, Jan. 2008.

[79] A. Ashkin and J. M. Dziedzic, "Optical levitation by radiation pressure," *Appl. Phys. Lett.*, vol. 19, no. 8, pp. 283–285, 1971.

[80] E. F. Nichols and G. F. Hull, "The pressure due to radiation," in *Proceedings of the American Academy of Arts and Sciences*, 1903, vol. 38, no. 20, pp. 559–599.

[81] M. Evander and J. Nilsson, "Acoustofluidics 20: Applications in acoustic trapping," *Lab Chip*, vol. 12, no. 22, pp. 4667–4676, 2012.

[82] L. Paterson, M. P. MacDonald, J. Arlt, W. Sibbett, P. E. Bryant, and K. Dholakia, "Controlled rotation of optically trapped microscopic particles," *Science (80-.).*, vol. 292, no. 5518, pp. 912–914, 2001.

[83] T. Čižmár, V. Garcéz-Chávez, K. Dholakia, and P. Zemánek, "Optical conveyor belt for delivery of sub-micron objects," in *Photonics, Devices, and Systems III*, 2006, p. 618027.

[84] D. B. Ruffner and D. G. Grier, "Optical conveyors: A class of active tractor beams," *Phys. Rev. Lett.*, vol. 109, no. 16, p. 163903, 2012.

[85] T. H. Maiman, "Stimulated optical radiation in ruby," 1960.

[86] M. Chalfie, Y. Tu, G. Euskirchen, W. W. Ward, and D. C. Prasher, "Green fluorescent protein as a marker for gene expression," *Science (80-.).*, vol. 263, no. 5148, pp. 802–805, 1994.

[87] A. H. Voie, D. H. Burns, and F. A. Spelman, "Orthogonal-plane fluorescence optical sectioning: Three-dimensional imaging of macroscopic biological specimens," *J. Microsc.*, vol. 170, no. 3, pp. 229–236, 1993.

[88] A. H. Voie and F. A. Spelman, "Three-dimensional reconstruction of the cochlea from two-dimensional images of optical sections," *Comput. Med. imaging Graph.*, vol. 19, no. 5, pp. 377–384, 1995.

[89] A. H. Voie, "Imaging the intact guinea pig tympanic bulla by orthogonal-plane fluorescence optical sectioning microscopy," *Hear. Res.*, vol. 171, no. 1, pp. 119–128, 2002.

[90] S. Lindek, R. Pick, and E. H. K. Stelzer, "Confocal theta microscope with three objective lenses," *Rev. Sci.*, vol. 65, no. 11, p. 3367, 1994.

[91] E. H. K. Stelzer, S. Lindek, S. Albrecht, R. Pick, G. Ritter, N. J. Salmon, and R. Stricker, "A new tool for the observation of embryos and other large specimens: confocal theta fluorescence microscopy," *J. Microsc.*, vol. 179, no. 1, pp. 1–10, 1995.

[92] E. Fuchs, J. S. Jaffe, R. A. Long, and F. Azam, "Thin laser light sheet microscope for microbial oceanography," *Opt. Express*, vol. 10, no. 2, p. 145, 2002.

[93] H.-U. Dodt, U. Leischner, A. Schierloh, N. Jährling, C. P. Mauch, K. Deininger, J. M. Deussing, M. Eder, W. Zieglgänsberger, and K. Becker, "Ultramicroscopy: three-dimensional visualization of neuronal networks in the whole mouse brain," *Nat. Methods*, vol. 4, no. 4, pp. 331–336, 2007.

[94] J. Huisken and D. Y. R. Stainier, "Even fluorescence excitation by multidirectional selective plane illumination microscopy (mSPIM).," *Opt. Lett.*, vol. 32, no. 17, pp. 2608–10, Sep. 2007.

[95] K. Greger, J. Swoger, and E. H. K. Stelzer, "Basic building units and properties of a fluorescence single plane illumination microscope," *Rev. Sci. Instrum.*, vol. 78, no. 2, p. 023705, 2007.

[96] J. A. N. Buytaert and J. J. J. Dirckx, "Design and quantitative resolution measurements of an optical virtual sectioning three-dimensional imaging technique for biomedical specimens, featuring two-micrometer slicing resolution," *J. Biomed. Opt.*, vol. 12, no. 1, p. 14039, 2007.

[97] E. Fuchs, J. Jaffe, R. Long, and F. Azam, "Thin laser light sheet microscope for microbial oceanography.," *Opt. Express*, vol. 10, no. 2, pp. 145–54, Jan. 2002.

[98] C. Dunsby, "Optically sectioned imaging by oblique plane microscopy," in *European Conference on Biomedical Optics*, 2009.

[99] P. J. Keller and E. H. K. Stelzer, "Quantitative in vivo imaging of entire embryos with Digital Scanned Laser Light Sheet Fluorescence Microscopy.," *Curr. Opin. Neurobiol.*, vol. 18, no. 6, pp. 624–32, Dec. 2008.

[100] J. Mertz and J. Kim, "Scanning light-sheet microscopy in the whole mouse brain with HiLo background rejection.," *J. Biomed. Opt.*, vol. 15, no. 1, p. 016027, 2010.

[101] T. V Truong, W. Supatto, D. S. Koos, J. M. Choi, and S. E. Fraser, "Deep and fast live imaging with two-photon scanned light-sheet microscopy.," *Nat. Methods*, vol. 8, no. 9, pp. 757–60, Sep. 2011.

[102] R. Tomer, K. Khairy, F. Amat, P. J. Keller, and E. H. K. Stelzer, "Quantitative high-speed imaging of entire developing embryos with simultaneous multiview light-sheet microscopy.," *Nat. Methods*, vol. 9, no. 7, pp. 755–63, Jul. 2012.

[103] U. Krzic, S. Gunther, T. E. Saunders, S. J. Streichan, and L. Hufnagel, "Multiview light-sheet microscope for rapid in toto imaging.," *Nat. Methods*, vol. 9, no. 7, pp. 730–3, Jul. 2012.

[104] Zeiss, "Lightsheet Z.1 Fast, Gentle Imaging for Living Samples." .

[105] T. F. Holekamp, D. Turaga, and T. E. Holy, "Fast three-dimensional fluorescence imaging of activity in neural populations by objective-coupled planar illumination microscopy," *Neuron*, vol. 57, no. 5, pp. 661–672, 2008.

[106] D. Turaga and T. E. Holy, "Miniaturization and defocus correction for objective-coupled planar illumination microscopy," *Opt. Lett.*, vol. 33, no. 20, pp. 2302–2304, 2008.

[107] P. J. Keller and E. H. K. Stelzer, "Digital scanned laser light sheet fluorescence microscopy," *Cold Spring Harb. Protoc.*, vol. 2010, no. 5, p. pdb–top78, 2010.

[108] T. Breuninger, K. Greger, and E. H. K. Stelzer, "Lateral modulation boosts image quality in single plane illumination fluorescence microscopy.," *Opt. Lett.*, vol. 32, no. 13, pp. 1938–40, Jul. 2007.

[109] J. Palero, S. I. Santos, D. Artigas, and P. Loza-Alvarez, "A simple scanless two-photon fluorescence microscope using selective plane illumination," *Opt. Express*, vol. 18, no. 8, pp. 8491–8498, 2010.

[110] M. B. Ahrens, M. B. Orger, D. N. Robson, J. M. Li, and P. J. Keller, "Whole-brain functional imaging at cellular resolution using light-sheet microscopy.," *Nat. Methods*, vol. 10, no. 5, pp. 413–20, May 2013.

[111] P. Tomancak, "OpenSPIM Wiki." 2013.

[112] J. D. Rouse, C. A. Bishop, and J. Struger, "Nitrogen pollution: an assessment of its threat to amphibian survival.," *Environ. Health Perspect.*, vol. 107, no. 10, p. 799, 1999.

[113] A. Eshel and T. Beeckman, *Plant roots: the hidden half*. CRC Press, 2013.

[114] J. P. Lynch, "Turner review no. 14. Roots of the second green revolution," *Aust. J. Bot.*, vol. 55, no. 5, pp. 493–512, 2007.

[115] I. De Smet, P. J. White, a G. Bengough, L. Dupuy, B. Parizot, I. Casimiro, R. Heidstra, M. Laskowski, M. Lepetit, F. Hochholdinger, others, X. Draye, H. Zhang, M. R. Broadley, B. Péret, J. P. Hammond, H. Fukaki, S. Mooney, J. P. Lynch, P. Nacry, U. Schurr, L. Laplaze, P. Benfey, T. Beeckman, and M. Bennett, "Analyzing lateral root development: how to move forward," *Plant Cell Online*, vol. 24, no. 1, pp. 15–20, Jan. 2012.

[116] H. Downie, N. Holden, W. Otten, A. J. Spiers, T. A. Valentine, and L. X. Dupuy, "Transparent soil for imaging the rhizosphere," *PLoS One*, vol. 7, no. 9, p. e44276, Jan. 2012.

[117] R. Tomer, K. Khairy, and P. J. Keller, "Light Sheet Microscopy in Cell Biology," in *Cell Imaging Techniques*, Springer, 2013, pp. 123–137.

[118] E. G. Reynaud, U. Kržič, K. Greger, E. H. K. Stelzer, and U. Krzic, "Light sheet-based fluorescence microscopy: more dimensions, more photons, and less photodamage.," *HFSP J.*, vol. 2, no. 5, pp. 266–75, Oct. 2008.

[119] J. Huisken and D. Y. R. Stainier, "Selective plane illumination microscopy techniques in developmental biology.," *Development*, vol. 136, no. 12, pp. 1963–75, Jun. 2009.

[120] M. Shotton, others, and D. Shotton, "Confocal scanning optical microscopy and its applications for biological specimens," *J. Cell Sci.*, vol. 94, no. 2, p. 175, 1989.

[121] W. J. J. Alford, R. D. R. D. VanderNeut, and V. J. V. J. Zaleckas, "Laser scanning microscopy," *Proc. IEEE*, vol. 70, no. 6, pp. 641–651, 1982.

[122] T. Van Nguyen, M. V. Nguyen, K. J. Nordheden, and W. He, "Effect of bulk and surface treatments on the surface ionic activity of nafion membranes," *J. Electrochem. Soc.*, vol. 154, no. 11, pp. A1073–A1076, 2007.

[123] D.-G. Strullu and C. Romand, "Méthode d'obtention d'endomycorhizes à vésicules et arbuscules en conditions axéniques," *Comptes rendus l'Academie des Sci. Ser. III. Sci. la Vie*, vol. 303, no. 6, pp. 245–250, 1986.

[124] S. Declerck, D. G. Strullu, and C. Plenchette, "Monoxenic Culture of the Intraradical Forms of Glomus sp. Isolated from a Tropical Ecosystem: A Proposed Methodology for Germplasm Collection," *Mycologia*, vol. 90, no. 4, p. 579, Jul. 1998.

[125] L. Dolan, K. Janmaat, V. Willemsen, P. Linstead, S. Poethig, K. Roberts, and B. Scheres, "Cellular organisation of the Arabidopsis thaliana root," *Development*, vol. 119, no. 1, pp. 71–84, 1993.

[126] A. G. Bell, "On the Production and Reproduction of Speech by Light," *Am. J. Sci.*, vol. 20, no. 118, pp. 305–324, 1880.

[127] L. V Wang and S. Hu, "Photoacoustic tomography: in vivo imaging from organelles to organs.," *Science*, vol. 335, no. 6075, pp. 1458–62, Mar. 2012.

[128] L. V Wang, "Multiscale photoacoustic microscopy and computed tomography.," *Nat. Photonics*, vol. 3, no. 9, pp. 503–509, Aug. 2009.

[129] N. Weidner, J. P. Semple, W. R. Welch, and J. Folkman, "Tumor angiogenesis and metastasis--correlation in invasive breast carcinoma.," *N. Engl. J. Med.*, vol. 324, no. 1, pp. 1–8, Jan. 1991.

[130] S. Hu, K. Maslov, and L. Wang, "Second-generation optical-resolution photoacoustic microscopy with improved sensitivity and speed," *Opt. Lett.*, vol. 36, no. 7, pp. 1134–1136, 2011.

[131] K. Maslov, H. F. Zhang, S. Hu, and L. V Wang, "Optical-resolution photoacoustic microscopy for in vivo imaging of single capillaries.," *Opt. Lett.*, vol. 33, no. 9, pp. 929–31, May 2008.

[132] H. F. Zhang, K. Maslov, G. Stoica, and L. V Wang, "Functional photoacoustic microscopy for high-resolution and noninvasive in vivo imaging.," *Nat. Biotechnol.*, vol. 24, no. 7, pp. 848–51, Jul. 2006.

[133] M. Xu and L. V Wang, "Time-domain reconstruction for thermoacoustic tomography in a spherical geometry.," *IEEE Trans. Med. Imaging*, vol. 21, no. 7, pp. 814–22, Jul. 2002.

[134] M. Xu and L. Wang, "Universal back-projection algorithm for photoacoustic computed tomography," *Phys. Rev. E*, vol. 71, no. 1, p. 016706, Jan. 2005.

[135] G. Ku, X. Wang, G. Stoica, and L. V Wang, "Multiple-bandwidth photoacoustic tomography," *Phys. Med. Biol.*, vol. 49, no. 7, pp. 1329–1338, Apr. 2004.

[136] M. Xu and L. Wang, "Analytic explanation of spatial resolution related to bandwidth and detector aperture size in thermoacoustic or photoacoustic reconstruction," *Phys. Rev. E*, vol. 67, no. 5, p. 056605, May 2003.

[137] M. Haltmeier, O. Scherzer, P. Burgholzer, and G. Paltauf, "Thermoacoustic computed tomography with large planar receivers," *Inverse Probl.*, vol. 20, no. 5, pp. 1663–1673, Oct. 2004.

[138] P. Burgholzer, C. Hofer, G. Paltauf, M. Haltmeier, and O. Scherzer, "Thermoacoustic tomography with integrating area and line detectors," *IEEE Trans. Ultrason. Ferroelectr. Freq. Control*, vol. 52, no. 9, pp. 1577–1583, Sep. 2005.

[139] J. Mertz, "Optical sectioning microscopy with planar or structured illumination.," *Nat. Methods*, vol. 8, no. 10, pp. 811–9, Jan. 2011.

[140] M. A. Fiddy, "The Radon Transform and Some of Its Applications," *Opt. Acta Int. J. Opt.*, vol. 32, no. 1, pp. 3–4, Jan. 1985.

[141] Z. Yang, H. Downie, and E. Rozbicki, "Light Sheet Tomography (LST) for in situ imaging of plant roots," *Opt. Express*, vol. 21, no. 14, pp. 16239–16247, 2013.

[142] L. Allen, M. W. Beijersbergen, R. J. C. Spreeuw, J. P. Woerdman, and others, "Orbital angular momentum of light and the transformation of Laguerre-Gaussian laser modes," *Phys. Rev. A*, vol. 45, no. 11, pp. 8185–8189, 1992.

[143] T. Wu, T. A. Nieminen, S. Mohanty, J. Miotke, R. L. Meyer, H. Rubinsztein-Dunlop, and M. W. Berns, "A photon-driven micromotor can direct nerve fibre growth," *Nat. Photonics*, vol. 6, no. 1, pp. 62–67, 2011.

[144] M. R. Dennis, R. P. King, B. Jack, K. O'Holleran, and M. J. Padgett, "Isolated optical vortex knots," *Nat. Phys.*, vol. 6, no. 2, pp. 118–121, Jan. 2010.

[145] B. Hefner and P. Marston, "Acoustical helicoidal waves and Laguerre-Gaussian beams: Applications to scattering and to angular momentum transport," *J. Acoust. Soc. Am*, pp. 1921–1922, 1998.

[146] B. T. Hefner and P. L. Marston, "An acoustical helicoidal wave transducer with applications for the alignment of ultrasonic and underwater systems," *J. Acoust. Soc. Am.*, vol. 106, no. 6, p. 3313, 1999.

[147] R. Marchiano and J.-L. Thomas, "Synthesis and analysis of linear and nonlinear acoustical vortices," *Phys. Rev. E*, vol. 71, no. 6, Jun. 2005.

[148] J. Lekner, "Acoustic beams with angular momentum," *J. Acoust. Soc. Am.*, vol. 120, no. 6, p. 3475, 2006.

[149] L. Allen, M. J. Padgett, and M. Babiker, "IV The orbital angular momentum of light," *Prog. Opt.*, vol. 39, pp. 291–372, 1999.

[150] R. A. Beth, "Mechanical detection and measurement of the angular momentum of light," *Phys. Rev.*, vol. 50, no. 2, p. 115, 1936.

[151] L. Allen, M. Beijersbergen, R. Spreeuw, and J. Woerdman, "Orbital angular momentum of light and the transformation of Laguerre-Gaussian laser modes," *Phys. Rev. A*, vol. 45, no. 11, pp. 8185–8189, Jun. 1992.

[152] A. Ambrosio, L. Marrucci, F. Borbone, A. Roviello, and P. Maddalena, "Light-induced spiral mass transport in azo-polymer films under vortex-beam illumination.," *Nat. Commun.*, vol. 3, p. 989, Jan. 2012.

[153] L. Paterson, M. P. MacDonald, J. Arlt, W. Dultz, H. Schmitzer, W. Sibbett, and K. Dholakia, "Controlled simultaneous rotation of multiple optically trapped particles," *J. Mod. Opt.*, vol. 50, no. 10, pp. 1591–1599, 2003.

[154] K. T. Gahagan, G. A. Swartzlander Jr, and others, "Optical vortex trapping of particles," *Opt. Lett.*, vol. 21, no. 11, pp. 827–829, 1996.

[155] S. Kuppens, M. Rauner, M. Schiffer, K. Sengstock, W. Ertmer, F. E. Van Dorsselaer, and G. Nienhuis, "Polarization-gradient cooling in a strong doughnut-mode dipole potential," *Phys. Rev. A*, vol. 58, no. 4, p. 3068, 1998.

[156] M. Schiffer, M. Rauner, S. Kuppens, M. Zinner, K. Sengstock, and W. Ertmer, "Guiding, focusing, and cooling of atoms in a strong dipole potential," *Appl. Phys. B Lasers Opt.*, vol. 67, no. 6, pp. 705–708, 1998.

[157] S. Gspan, A. Meyer, S. Bernet, and M. Ritsch-Marte, "Optoacoustic generation of a helicoidal ultrasonic beam," *J. Acoust. Soc. Am.*, vol. 115, no. 3, p. 1142, 2004.

[158] J.-L. Thomas and R. Marchiano, "Pseudo angular momentum and topological charge conservation for nonlinear acoustical vortices," *Phys. Rev. Lett.*, vol. 91, no. 24, p. 244302, 2003.

[159] A. O. Santillán and K. Volke-Sepúlveda, "A demonstration of rotating sound waves in free space and the transfer of their angular momentum to matter," *Am. J. Phys.*, vol. 77, no. 3, p. 209, 2009.

[160] A. Biswas, E. W. Leung, and E. H. Trinh, "Rotation of ultrasonically levitated glycerol drops," *J. Acoust. Soc. Am.*, vol. 90, no. 3, p. 1502, 1991.

[161] M. R. Schroeder, "Circularly polarized acoustic fields: the number theory connection," *Acta Acust. united with Acust.*, vol. 75, no. 2, pp. 94–98, 1991.

[162] L. Zhang and P. L. Marston, "Angular momentum flux of nonparaxial acoustic vortex beams and torques on axisymmetric objects," *Phys. Rev. E*, vol. 84, no. 6, Dec. 2011.

[163] E. G. Williams and J. A. Mann, "Fourier Acoustics: Sound Radiation and Nearfield Acoustical Holography," *J. Acoust. Soc. Am.*, vol. 108, no. 4, pp. 1373–1373, Oct. 2000.

[164] G. C. Spalding, "User-Friendly, Freeware Image Segmentation and Particle Tracking." .

[165] R. Kobayashi, "Review: Laminar-to-Turbulent Transition of Three-Dimensional Boundary Layers on Rotating Bodies," *J. Fluids Eng.*, vol. 116, no. 2, p. 200, 1994.

[166] I. T. Simulations, "Prediction and investigation of the turbulent flow over a rotating disk," vol. 418, pp. 231–264, 2000.

[167] S. Hashimoto, H. Ito, and Y. Inoue, "Experimental study on geometric structure of isolated mixing region in impeller agitated vessel," *Chem. Eng. Sci.*, vol. 64, no. 24, pp. 5173–5181, 2009.

[168] N. Ohmura, T. Makino, T. Kaise, and K. Kataoka, "Transition of organized flow structure in a stirred vessel at low Reynolds numbers," *J. Chem. Eng. Japan*, vol. 36, no. 12, pp. 1458–1463, 2003.

[169] R. K. Sinnott and G. Towler, *Chemical Engineering Design: SI Edition*. Access Online via Elsevier, 2009.

[170] T. Hasegawa and K. Yosioka, "Acoustic radiation force on fused silica spheres, and intensity determination," *J. Acoust. Soc. Am.*, vol. 58, p. 581, 1975.

[171] R. T. Beyer, "Radiation pressure—the history of mislabeled tensor," *J. Acoust. Soc. Am.*, vol. 60, no. S1, p. S21, 1976.

[172] A. Ashkin, "Applications of laser radiation pressure.," *Science*, vol. 210, no. 4474, pp. 1081–8, Dec. 1980.

[173] A. Ashkin and J. P. Gordon, "Stability of radiation-pressure particle traps: an optical Earnshaw theorem," *Opt. Lett.*, vol. 8, no. 10, p. 511, Oct. 1983.

[174] M. P. MacDonald, G. C. Spalding, and K. Dholakia, "Microfluidic sorting in an optical lattice.," *Nature*, vol. 426, no. 6965, pp. 421–4, Nov. 2003.

[175] M. Wiklund, S. Radel, and J. J. Hawkes, "Acoustofluidics 21: ultrasound-enhanced immunoassays and particle sensors.," *Lab Chip*, vol. 13, no. 1, pp. 25–39, Jan. 2013.

[176] P. L. Marston, "Axial radiation force of a Bessel beam on a sphere and direction reversal of the force," *J. Acoust. Soc. Am.*, vol. 120, no. 6, p. 3518, 2006.

[177] L. Zhang and P. L. Marston, "Geometrical interpretation of negative radiation forces of acoustical Bessel beams on spheres," *Phys. Rev. E*, vol. 84, no. 3, p. 035601, Sep. 2011.

[178] S. Sukhov and a Dogariu, "On the concept of 'tractor beams'.," *Opt. Lett.*, vol. 35, no. 22, pp. 3847–9, Nov. 2010.

[179] J. Chen, J. Ng, Z. Lin, and C. T. Chan, "Optical pulling force," *Nat. Photonics*, vol. 5, no. 9, pp. 531–534, Jul. 2011.

[180] A. Novitsky, C.-W. Qiu, and H. Wang, "Single Gradientless Light Beam Drags Particles as Tractor Beams," *Phys. Rev. Lett.*, vol. 107, no. 20, p. 203601, Nov. 2011.

[181] O. Brzobohatý, V. Karásek, M. Šiler, L. Chvátal, T. Čižmár, and P. Zemánek, "Experimental demonstration of optical transport, sorting and self-

arrangement using a ‘tractor beam,’” *Nat. Photonics*, vol. 7, no. 2, pp. 123–127, Jan. 2013.

[182] A. Ashkin, J. Dziedzic, and T. Yamane, “Optical trapping and manipulation of single cells using infrared laser beams,” *Nature*, 1987.

[183] T. Čižmár, V. Garcéz-Chávez, K. Dholakia, P. Zemánek, T. C̆iz̆már, V. Garcés-Chávez, and P. Zemánek, “Optical conveyor belt for delivery of submicron objects,” *Appl. Phys. Lett.*, vol. 86, no. 17, p. 174101, 2005.

[184] T. Čižmár, V. Kollárová, Z. Bouchal, and P. Zemánek, “Sub-micron particle organization by self-imaging of non-diffracting beams,” *New J. Phys.*, vol. 8, no. 3, pp. 43–43, Mar. 2006.

[185] S.-H. Lee, Y. Roichman, and D. G. Grier, “Optical solenoid beams.,” *Opt. Express*, vol. 18, no. 7, pp. 6988–93, Mar. 2010.

[186] A. Dogariu, S. Sukhov, and J. Sáenz, “Optically induced ‘negative forces,’” *Nat. Photonics*, vol. 7, no. 1, pp. 24–27, Dec. 2012.

[187] V. G. Veselago, “Energy, linear momentum and mass transfer by an electromagnetic wave in a negative-refraction medium,” *Physics-Uspekhi*, vol. 52, no. 6, pp. 649–654, Jun. 2009.

[188] V. Yannopapas and P. Galiatsatos, “Electromagnetic forces in negative-refractive-index metamaterials: A first-principles study,” *Phys. Rev. A*, vol. 77, no. 4, p. 043819, Apr. 2008.

[189] B. Kemp, J. Kong, and T. Grzegorczyk, “Reversal of wave momentum in isotropic left-handed media,” *Phys. Rev. A*, vol. 75, no. 5, p. 053810, May 2007.

[190] H. Monjushiro, K. Takeuchi, and H. Watarai, “Anomalous Laser Photophoretic Behavior of Photo-Absorbing Organic Droplets in Water,” *Chem. Lett.*, no. 8, pp. 788–788, 2002.

[191] V. G. Shvedov, A. S. Desyatnikov, A. V. Rode, W. Krolikowski, and Y. S. Kivshar, “Optical guiding of absorbing nanoclusters in air,” *Opt. Express*, vol. 17, no. 7, p. 5743, Mar. 2009.

[192] A. S. Desyatnikov, V. G. Shvedov, A. V. Rode, W. Krolikowski, and Y. S. Kivshar, “Photophoretic manipulation of absorbing aerosol particles with vortex beams: theory versus experiment,” *Opt. Express*, vol. 17, no. 10, p. 8201, Apr. 2009.

[193] V. G. Shvedov, A. V. Rode, Y. V. Izdebskaya, A. S. Desyatnikov, W. Krolikowski, and Y. S. Kivshar, "Giant Optical Manipulation," *Phys. Rev. Lett.*, vol. 105, no. 11, p. 118103, Sep. 2010.

[194] A. Jannasch, A. F. Demirörs, P. D. J. van Oostrum, A. van Blaaderen, and E. Schäffer, "Nanonewton optical force trap employing anti-reflection coated, high-refractive-index titania microspheres," *Nat. Photonics*, vol. 6, no. 7, pp. 469–473, Jun. 2012.

[195] A. Novitsky, C.-W. Qiu, and A. Lavrinenko, "Material-Independent and Size-Independent Tractor Beams for Dipole Objects," *Phys. Rev. Lett.*, vol. 109, no. 2, p. 023902, Jul. 2012.

[196] J. M. Geffrin, B. García-Cámara, R. Gómez-Medina, P. Albella, L. S. Froufe-Pérez, C. Eyraud, A. Litman, R. Vaillon, F. González, M. Nieto-Vesperinas, J. J. Sáenz, and F. Moreno, "Magnetic and electric coherence in forward- and back-scattered electromagnetic waves by a single dielectric subwavelength sphere.," *Nat. Commun.*, vol. 3, p. 1171, Jan. 2012.

[197] A. Mizrahi and Y. Fainman, "Negative radiation pressure on gain medium structures.," *Opt. Lett.*, vol. 35, no. 20, pp. 3405–7, Oct. 2010.

[198] K. J. Webb, "Negative electromagnetic plane-wave force in gain media," *Phys. Rev. E*, vol. 84, no. 5, p. 057602, Nov. 2011.

[199] G. A. Swartzlander, T. J. Peterson, A. B. Artusio-Glimpse, and A. D. Raisanen, "Stable optical lift," *Nat. Photonics*, vol. 5, no. 1, pp. 48–51, Dec. 2010.

[200] J. J. Sáenz, "Optical forces: Laser tractor beams," *Nat. Photonics*, vol. 5, no. 9, pp. 514–515, Aug. 2011.

[201] S. Sukhov and a. Dogariu, "Negative Nonconservative Forces: Optical 'Tractor Beams' for Arbitrary Objects," *Phys. Rev. Lett.*, vol. 107, no. 20, p. 203602, Nov. 2011.

[202] V. Kajorndejnukul, W. Ding, S. Sukhov, C.-W. Qiu, and A. Dogariu, "Linear momentum increase and negative optical forces at dielectric interface," *Nat. Photonics*, vol. 7, no. 10, pp. 787–790, Aug. 2013.

[203] J. Wu, "Acoustical tweezers," *J. Acoust. Soc. Am.*, vol. 89, no. 5, p. 2140, 1991.

[204] J. Lee, K. Ha, and K. K. Shung, "A theoretical study of the feasibility of acoustical tweezers: Ray acoustics approach," *J. Acoust. Soc. Am.*, vol. 117, no. 5, p. 3273, 2005.

[205] J. Lee and K. K. Shung, "Radiation forces exerted on arbitrarily located sphere by acoustic tweezer," *J. Acoust. Soc. Am.*, vol. 120, no. 2, p. 1084, 2006.

[206] P. L. Marston, "Negative axial radiation forces on solid spheres and shells in a Bessel beam.," *J. Acoust. Soc. Am.*, vol. 122, no. 6, pp. 3162–5, Dec. 2007.

[207] P. L. Marston, "Radiation force of a helicoidal Bessel beam on a sphere.," *J. Acoust. Soc. Am.*, vol. 125, no. 6, pp. 3539–47, Jun. 2009.

[208] T. Neumann and H. Ermert, "Schlieren visualization of ultrasonic wave fields with high spatial resolution.," *Ultrasonics*, vol. 44 Suppl 1, pp. e1561–6, Dec. 2006.

[209] P. Glynne-Jones, P. P. Mishra, R. J. Boltryk, and M. Hill, "Efficient finite element modeling of radiation forces on elastic particles of arbitrary size and geometry.," *J. Acoust. Soc. Am.*, vol. 133, no. 4, pp. 1885–93, Apr. 2013.

[210] K. Yosioka, "Acoustic radiation pressure on a compressible sphere," *Acustica*, vol. 5, pp. 167–173, 1955.

[211] C. P. Lee and T. G. Wang, "Acoustic radiation pressure," *J. Acoust. Soc. Am.*, vol. 94, p. 1099, 1993.

[212] P. J. Verveer, J. Swoger, F. Pampaloni, K. Greger, M. Marcello, and E. H. K. Stelzer, "High-resolution three-dimensional imaging of large specimens with light sheet-based microscopy.," *Nat. Methods*, vol. 4, no. 4, pp. 311–3, Apr. 2007.

[213] T. Vettenburg, H. I. C. Dalgarno, J. Nylk, C. Coll-Lladó, D. E. K. Ferrier, T. Cižmár, F. J. Gunn-Moore, and K. Dholakia, "Light-sheet microscopy using an Airy beam.," *Nat. Methods*, vol. 11, no. 5, pp. 541–4, May 2014.

[214] M. J. Booth, "Adaptive optics in microscopy.," *Philos. Trans. A. Math. Phys. Eng. Sci.*, vol. 365, no. 1861, pp. 2829–43, Dec. 2007.

[215] M. Padgett and R. Di Leonardo, "Holographic optical tweezers and their relevance to lab on chip devices.," *Lab Chip*, vol. 11, no. 7, pp. 1196–205, Apr. 2011.